University College Cork, Cork

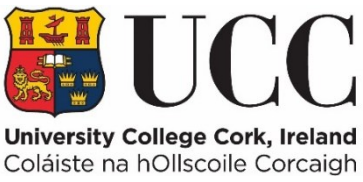

Sustainable Laser-Induced Graphene (LIG) for Electrochemical Sensing, Energy Storage and Harvesting

Thesis presented by

Md Jahidul Islam

for the degree of

Doctor of Philosophy

Tyndall National Institute

University College Cork

Supervisors: Dr Daniela Iacopino and Dr Aidan Quinn

Head of Department: Dr Fatima Gunning

2025

Table of Contents

Abbreviations

AA – Ascorbic Acid

ABT – 4-Aminobenzenethiol

AC – Alternating Current

Ag NPs – Silver Nanoparticles

ATR-FTIR – Attenuated Total Reflection-Fourier Transform Infrared

BPPG – Basal Plane Pyrolytic Graphite

BET – Brunauer-Emmett-Teller

CA – Specific Areal Capacitance

CE – Counter Electrode

CO_2 – Carbon Dioxide

CVD – Chemical Vapor Deposition

CVD-Gr – Chemical Vapor Deposition-Graphene

CS-LIGN-BA – Chitosan-Lignin-Boric Acid

CP – Chronopotentiometry

CV – Cyclic Voltammetry

CNF – Cellulose Nanofiber

DA – Dopamine

DIF – Difloxacin hydrochloride

DI – Deionized Water

DLW – Direct Laser Writing

DOE – Design of Experiments

DOS – Density of Electronic States

D_O – Diffusion Coefficients of Oxidized Analyte Form

D_R – Diffusion Coefficients of Reduced Analyte Form

DPV – Differential Pulse Voltammetry

DMAB – Di-mercaptoazobenzene

D-TGA – Derivative of Thermogravimetric Analysis

EC-SERS – Electrochemical Surface Enhanced Raman Spectroscopy

EIS – Electrochemical Impedance Spectroscopy

EPE – Education and Public Engagement

EPPG – Edge Plane Pyrolytic Graphite

EDLC – Electric Double-Layer Capacitance

ED – Energy Density

EDS – Energy Dispersive Spectroscopy

EP – Peak Potential

FWHM – Full Width at Half Maximum

GO – Graphene Oxide

GCD – Galvanostatic Charge Discharge

HR-TEM – High Resolution

HET – Heterogeneous Electron Transfer

I_D – Intensity of D Peak

I_{SC} – Short Circuit Current

I_G – Intensity of G Peak

I_{2D} – Intensity of 2D Peak

IoT – Internet of Things

g-LIG – Green Laser-Induced Graphene

IP – Peak Current

LED – Light Emitting Diode

LIGN – Lignin

CS – Chitosan

BA – Boric Acid

LP – Laser Power

DA – Depth Adjustment

LD – Laser Depth

LOD – Limit of Detection

LIG – Laser-Induced Graphene

MRL – Maximum Residual Limit

NPs – Nanoparticles

Nd:YAG – Neodymium-Doped Yttrium Aluminum Garnet

NLDFT – Nonlocal Density Functional Theory

OCP – Open Circuit Potential

PBS – Phosphate Buffered Saline

PET – Polyethylene Terephthalate

PBM – Polybenzimidazole

PC – Polycarbonate

PC – Pseudo-Capacitance

PD – Power Density

PDCT – Photon Driven Charge Transfer

PDMS – Polydimethylsiloxane

PEEK – Polyether Ether Ketone

PEI – Polyetherimide

PEDOT – Poly(3,4-Ethylenedioxythiophene)

PMMA – Poly(methyl methacrylate)

CMCS – Carboxymethyl Cellulose

PI – Polyimide

PLD – Pulsed Laser Deposition

PVA – Polyvinyl Alcohol

RE – Reference Electrode

R_{SH} – Sheet Resistance

RSF – Relative Sensitivity Factors

TEMPO – 2,2,6,6-Tetramethylpiperidin-1-Oxyl Radical

SC – Supercapacitor

SPC – Self Charging Supercapacitor Power Cell

DoE-RS – Response Surface Design of Experiment

SE-TENG – Single-Electrode Triboelectric Nanogenerator

SEM – Scanning Electron Microscopy

SPCE – Screen-Printed Carbon Electrode

SERS – Surface-Enhanced Raman Spectroscopy

SWV – Square Wave Voltammetry

SSA – Specific Surface Area

TENG – Triboelectric Nanogenerator

TGA – Thermogravimetric Analysis

TEM – Transmission Electron Microscopy

HR-TEM – High Resolution Transmission Electron Microscopy

TLM – Transmission Line Measurement

TPa – Tera Pascal

UA – Uric Acid

V_{OC} – Open Circuit Potential

XPS – X-ray Photoelectron Spectroscopy

Declaration

This is to certify that the work I am submitting is my own and has not been submitted for another degree, either at University College Cork or elsewhere. All external references and sources are clearly acknowledged and identified within the contents. I have read and understood the regulations of University College Cork concerning plagiarism and intellectual property.

Md Jahidul Islam

Acknowledgements

I would like to begin by expressing my sincere gratitude to my supervisors, Daniela and Aidan, for their unwavering support throughout my PhD journey. Their insightful guidance, continuous encouragement, and trust have been essential to my growth and success. I am particularly grateful to Daniela for her exceptional mentorship, which has deeply influenced both my academic and personal development. I am equally thankful to Aidan for his practical advice and direction, which have kept me on the right track. I would also like to extend my thanks to my thesis examiners, Raymond Duffy and Johan Hjelm, for their careful review and constructive feedback, which have undoubtedly contributed to the strength of my work.

Throughout this journey, I have been fortunate to meet many remarkable individuals who have enriched my experience. Eoghan, a true inspiration, was one of the first to introduce me to the fascinating worlds of laser processing and electrochemistry. His teachings have left a lasting impact, and I will always be grateful for that. Alessandra, thank you for sparking my passion for supercapacitors and for sharing your expertise. Richard, your exceptional professional training and practical insights have been invaluable, while Cathal, your thoughtful advice and creative demonstrations have always left me in awe. I am also indebted to Alida, whose friendship and wisdom have made a profound difference in my life. Your support, like that of an elder sibling, has been a constant source of comfort. Veronica, I will never forget the joy and camaraderie of those covid-era seafood dinners that you so thoughtfully organized.

Special thanks also go to Mintesinot, Martina, and Rasel for their stimulating discussions, which ranged from research topics to broader intellectual debates. I cannot leave out Hassan Hamidi, whose motivational words about pursuing a career as a renowned electrochemist will continue to guide me in the future.

Finally, I am grateful to Rafael, Yunyun, Tarun, and everyone else at Tyndall who has made this journey so memorable. If your name hasn't appeared here, it's likely because this section is more read by my thesis than by people! But rest assured, I am equally appreciative of all those who have played a part in this adventure.

Thanks to everyone who has contributed to this experience—your support, camaraderie, and shared knowledge have made it all possible.

Thesis Abstract

The fabrication of laser-induced graphene (LIG) via direct laser writing has emerged as a rapid, cost-effective, and versatile method for producing 3D graphitic materials. This technique enables precise control over porous structures, making it highly suitable for applications in electrochemical sensing, energy storage, and energy harvesting. Since its discovery in 2014, LIG fabrication has evolved into a significant research area. This thesis explores the development of LIG, investigating the materials used, their essential properties, and standard characterization techniques. The exceptional properties of LIG, such as its large surface area, high conductivity and tuneable porosity, make it an ideal candidate for electrochemical sensors, supercapacitors, and triboelectric nanogenerators (TENG). Particular emphasis is placed on optimizing fabrication parameters to enhance these properties and identifying sustainable precursor materials for LIG production. Among various carbon precursors, cork and chitosan-biopolymer derived from shrimp shells-emerge as a promising alternative to petroleum-based synthetic polymers due to their biodegradability, renewability, and reduced environmental impact. This thesis presents a detailed study on LIG synthesis strategies using traditional polyimide, cork and chitosan substrates to determine their efficiency as precursors for graphitization and patterning. Initially, efforts are focused on optimizing LIG synthesis and laser processing techniques on polyimide for electrochemical sensor applications. Next, strategies for fabricating flexible, “green” LIG architectures are explored. These architectures are further demonstrated in energy storage devices and triboelectric nanogenerators for sustainable energy harvesting. Overall, the laser processing strategies developed in this work highlight cork and chitosan as efficient and sustainable precursors for green-LIG synthesis. The presented approaches emphasize the potential of LIG as a versatile material for electrochemical and energy applications, paving the way for environmentally friendly and cost-effective graphene-based technologies.

Chapter 1: Introduction

1.1 2D and 3D Graphene

Graphene is a 2D carbon material, first discovered by Geim and Novoselov et al.[1] in 2004 and is characterised by a honeycomb lattice structure formed by a single-layer of sp^2-hybridised carbon atoms (**figure 1.1**). This hybridisation is responsible for graphene's exceptional properties such as electrical conductivity related to overlapping π bonds in the z-axis,[2] high surface area (2630 m^2/g),[3] mechanical strength (42 N/m), and Young's modulus (~1 TPa), related to in plane σ bonds,[4] and thermal conductivity (5 kW/mK at room temperature compared to copper (0.4 kW/mK) and carbon nanotubes (3 kW/mK).[5] Such exceptional properties make graphene an invaluable material for catalysis,[6] sensors,[7], [8] biotechnology,[9] environmental remediation[10] and energy storage applications.[11], [12]

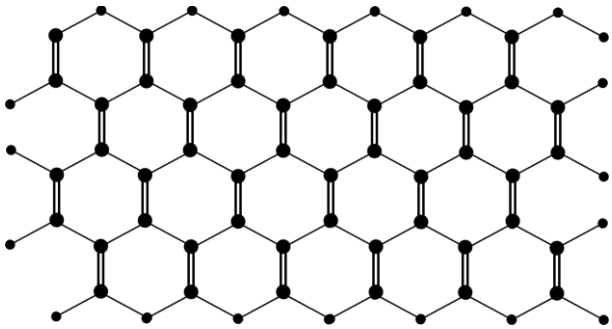

Figure 1.1 Schematic representation of 2D graphene

Graphene was first isolated via mechanical exfoliation of graphite,[1] but over time the extensive study of this material has resulted in a plethora of different methods being used for its fabrication, such as liquid-phase exfoliation,[13] pulsed laser deposition (PLD)[14] and chemical vapour deposition (CVD).[15] However, these methods often present some important limitations. For example, CVD allows the growth of large areas of graphene, but it has little control on defects and poses challenges on the removal of the graphene sheet from the substrate;[16] on the other hand, mechanical exfoliation is effective in isolating graphene sheet

of high quality, but it is very time consuming and allows the production of only small amounts of graphene.[17] Moreover, the scalability of these techniques at an industrial level still poses challenges in terms of cost-effectiveness, quality control, and environmental impact due to the high temperature and harsh chemicals used.[18] In addition, when incorporated in real world devices, 2D graphene layers tend to lose their unique properties.

Recently, the possibility to fabricate 3D graphene structures from connected 2D layers has emerged as a valid alternative to overcome the limitations of 2D graphene while maintaining its flexibility and mechanical stability.[12], [19] 3D graphene architectures have been widely produced since 2009 from hydrothermal/chemical reduction of graphene oxide (GO),[20]–[24] laser casting[25], [26] and 3D printing,[27] as well as through CVD.[28], [29] The large variety of created architectures has considerably broadened the applications of graphene in energy storage (batteries and supercapacitors), environmental protection, biomedical applications, among others.[30]

1.2 Emergence of Direct Laser Writing (DLW) for production of Laser-Induced Graphene (LIG)

In the quest to find scalable and cost-effective fabrication solutions, the research community is investigating alternative techniques featuring low embodied energy fabrication processes and high throughput. In 2014, the group of Tour *et al*. has developed a direct laser writing (DLW) technique for fabrication of graphene-like carbon materials on flexible polyimide films.[31] DLW converts polyimide into highly conductive and porous graphitic carbon patterns called laser induced graphene (LIG) by laser scribing under ambient and mild conditions (low laser power <5 W).[31], [32] The method is inherently environmentally friendly as the DLW transforms only the required areas of the substrate, avoiding the unnecessary conversion of material or wasteful production.[33]

In the first study reporting this technique, a commercial polyimide (PI) tape (also known as Kapton tape) was irradiated using an infrared CO_2 laser with 10.6 µm wavelength and pulse duration of ~14 µs.[31] During laser exposure, the irradiated area is subjected to localised high pressure (>3 GPa) and high temperature (>2500°C) that causes the breaking of C-O, C=O and C-N bonds in the polyimide and conversion from their original hybridisation to sp^2-rich chemical structures, through aromatisation and condensation processes, essentially causing the formation of graphene-like structures.[34]

Pulse duration **Laser Power**

Pulse energy **Scan speed**

Pulse number **Number of scans**

Pulse frequency

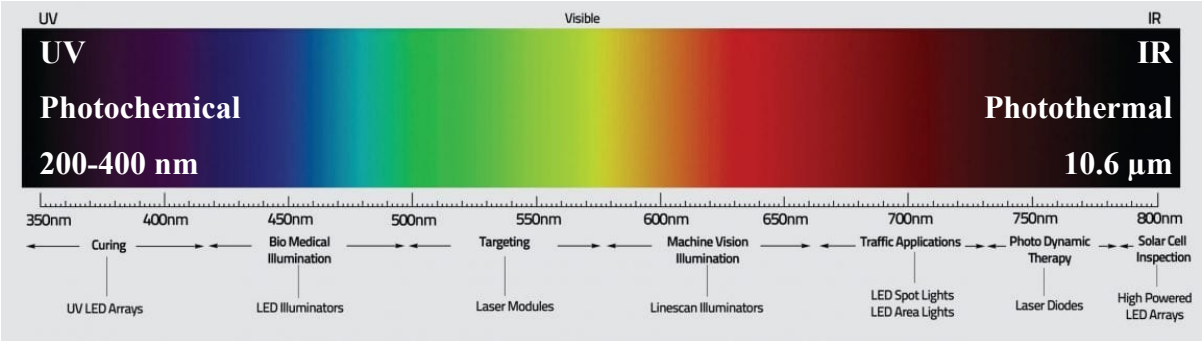

Figure 1.2 Laser parameters and LIG formation mechanism

Depending on the laser wavelength, the formation mechanism of LIG can be either (i) photothermal-dominated polymer pyrolysis (when the laser wavelength is >390nm) or (ii) combined photothermal and photochemical polymer pyrolysis (figure 1.2).[34] Photochemical effects depend on the wavelength of laser radiation and the mechanism of their interaction with the bonds of the specific material and excitation of electronic states by incident photons with adequate energy to cause bond cleavage and isomerisation. Photothermal effects are associated to the set of laser operational parameters (power, dwell time/depth etc.) and occur as result to laser exposure and are subject to bond breaking and rearrangements or in some cases, complete ablation.[35]

During this process, the extreme local conditions of pressure and temperature cause the recombination of oxygen and nitrogen, with formation of gas pockets that result in formation of a 3D structured materials with highly porous.[36] By tuning the laser setting, it is possible to regulate the pore size and to tune surface morphology of the LIG making this material appealing for a range of applications from catalysis to energy storage applications.[36], [37] Since the discovery of this technique, different laser sources have been investigated for LIG fabrication on different substrate materials, each with their specific advantages and disadvantages:

- CO_2 lasers are the most widely used engraving machine for production of LIG on PI and other polymeric materials, particularly due to the laser wavelength ranging from 9 to 11 μm that interacts strongly with the C-C bond. However, the main disadvantage is the relatively low spatial resolution, with the smallest spot size around 60-120 μm.[37]
- Nd:YAG lasers (operating wavelength of 1.06 μm) have been used to fabricate LIG with sheet resistance of ~40 Ω/sq.[32] However, their wavelength is poorly absorbed by carbon structures, and the laser has also poorer beam quality compared to other laser sources, and low energy efficiency.[37]
- Semiconductor diode lasers, with wavelengths of 405 and 450 nm have been also widely investigated for LIG fabrication. Compared to the other types of lasers, their main advantages are their higher spatial resolution of about 6-12 μm, high absorption on carbon structures, and very low cost.[37], [38]
- Fiber laser, a family of pulsed laser with ultra-short pulses (picoseconds, femtoseconds) and high quantum efficiency of about 94%. Among them, the femtosecond laser with wavelengths ranging between 1020-1070 nm have attracted interest for the conversion of carbon materials into LIG.[34] Their main advantages are a minimal photothermal ablation and high spatial resolution, however their use for LIG production is still very limited due to their high cost.[37]

- The possibility to form LIG from different substrates, initially fossil fuel derived polymers, and later from natural materials will be discussed more in detail later in this chapter and will be the object of the experimental work presented in Chapters 2, 3 and 4.

Among the polymers, those with high content of imide groups or aromatic units like the aforementioned PI, but also polyetherimide (PEI) can be converted to LIG, whereas polymers such as non-aromatic hydrocarbon simply degrade at high temperatures without converting into LIG.[31], [37] Moreover, a theoretical work from Green's group found out that polyether ether ketone (PEEK), similarly to PEI, converts in LIG with high surface area.[39] Their simulation also revealed that polycarbonate (PC) generates LIG with molecular structure characterised by many five- and seven-membered rings. Polybenzimidazole (PBM), however, was found to be the best LIG candidate thanks to the absence of oxygen in the polymer chain.[37], [39]

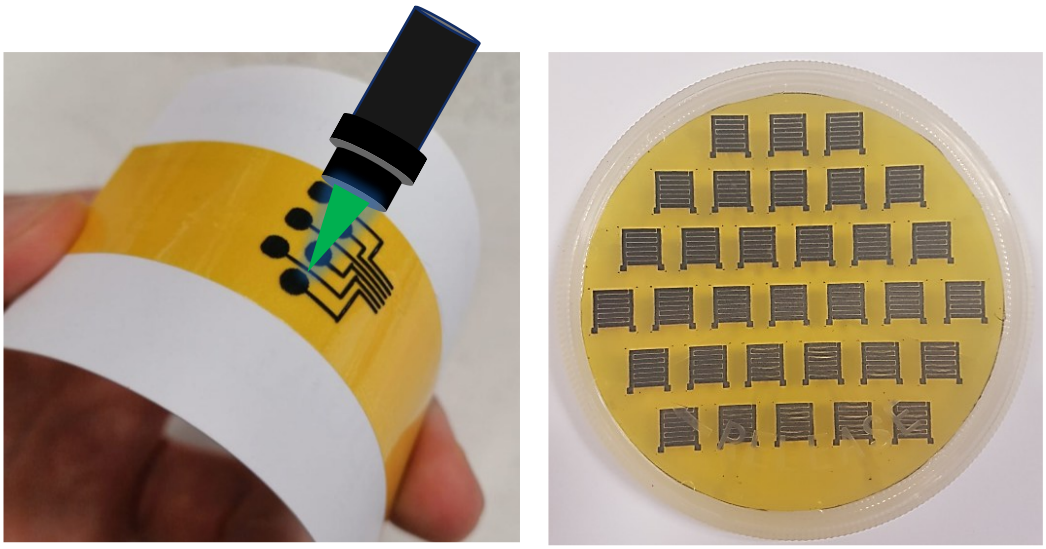

Figure 1.3 Examples of patterns obtained with DLW technique on Polyimide (PI)

In summary, the DLW technique has the great advantage of versatility of design, since virtually any pattern shape can be created (figure 1.3). The direct patterning of the substrate allows to convert a minimal amount of material, avoiding waste surplus, and does not require chemical precursors nor masks. The fabrication conditions are mild, with laser patterning being performed at room temperature and ambient conditions. The laser equipment is low cost, since

inexpensive hobbyist lasers can be used to perform DLW, and the technique is suitable for roll-to-roll scale up to wafer scale and above. Moreover, the LIG obtained from this technique has relatively low sheet resistance (< 50 Ω/sq) and high porosity that makes them suitable for electrochemical applications.

1.3 LIG Physical property characterisation

Many factors determine the quality of the LIG and its suitability for electrochemical applications: the bonding structure, chemical structure and crystallinity, the hydrophobicity, the morphology with presence of defects and pores, the electrical properties. To assess them, several morphological, physical and chemical techniques are used.

1.3.1 LIG surface morphology

The morphology of LIG is usually assessed via Scanning Electron Microscopy (SEM) technique. Examples of the typical LIG SEM micrograph are represented in figure 1.4. The thickness of the LIG film formed can be accessed via cross-section imaging (figure 1.4a). The surface is characterised by a highly porous structure and 3D that formed from the explosion of trapped gas pockets during the DLW process (figure 1.4b). Qualitative information on the pore size can be obtained by high magnification SEM images, while a quantitative and more accurate information can be obtained via Brunauer-Emmett-Teller (BET) analysis. Another interesting feature visible in the SEM micrographs is the presence of depressions and elevations like valleys and peaks, which are formed during the DLW of the substrate by the raster movements of the laser. As mentioned previously, it is possible to tune the surface morphology of the LIG by changing the laser irradiation condition.

The transmission electron microscope (TEM) image shows LIG structures with nanoscale wrinkles and rippled surface (figure 1.4c). The high-resolution TEM (HRTEM) image also shows the LIG layers contain plenty of graphene edges providing higher active surface area accessible for improved electrochemical performances (Inset of figure 1.4c). An example of

LIG fibers, consisting of bundles of conical fiber structures with an average diameter of approximately 50–70 nm and a typical length of around 100–200 µm, is shown in figure 1.4d. This LIG morphology is notably different from that shown in figure 1.4b, exhibiting a more fibrous and elongated structure.

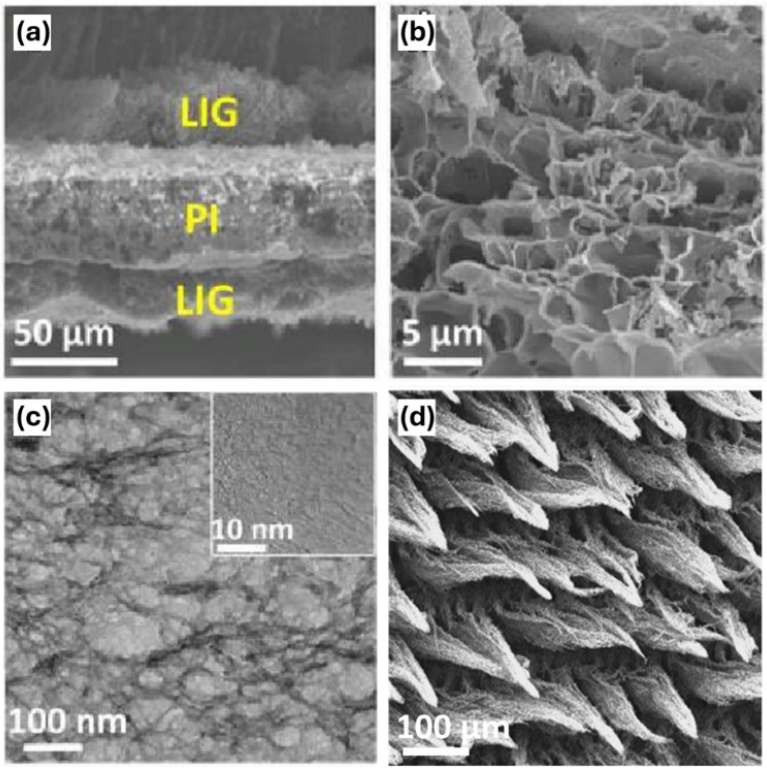

Figure 1.4 SEM micrographs of (a) Cross-sectional LIG on PI substrate with both sides scribed with laser to form graphene, (b) LIG films showing a porous 3D network, (c) TEM image of a LIG thin film showing nanosized wrinkles and ripples (Inset is a HRTEM image of a LIG nanosheet showing numerous graphene), c) fibrous LIG surface. Panels a) b) and c) adapted from [40]. Copyright 2015, ACS Publishing Group; panel 31 d) adapted from [41] Copyright 2020, ACS Publishing Group.

1.3.2 LIG sheet resistance

The Transmission Line Measurement (TML) technique can be used to determine the sheet resistance ($R_{SH,}$ measured in Ω/sq.) of LIG materials. TLM structures characterized by a specific aspect ratio are examined for resistance measurements across different lengths, L_i. The track resistance for a segment of material situated between two probes is connected to L_i through the following equation: $R_i = R_{CT} + (R_{SH} \times L_i)/W$

where R_i is the track resistance, R_{CT} is contact resistance, R_{SH} is sample's sheet resistance, and W is the track width. By taking multiple measurements it's possible to create a plot of R_i versus L_i that can be used to determine R_{SH} and R_{CT} via linear regression.

For LIG materials, the sheet resistance R_{SH} varies in a wide range, from less than 15 Ω/sq. to above than 100 Ω/sq.[31], [42] This is due to the different laser conditions and substrate material used for the LIG fabrication. For the majority of LIG applications, a low value of R_{SH} is required.

1.3.3 LIG chemical characterisation

The surface chemical characteristic can be investigated via X-Ray photoelectron spectroscopy (XPS), a particularly powerful tool for surface analysis thanks to its surface sensitivity (ca. 10 nm), its ability to differentiate the chemical environment, and the possibility to perform quantitative analysis of the surface chemical composition.[43] The kinetic energy of the photo-excited electrons that escape the sample surface as consequence of the X-ray bombardment provides information on the binding energy and allows the identification of the element and of its bonding state. For the characterisation of LIG, the regions of interest are the C1s and O1s. In the case of doped LIG, regions relative to the dopant elements may be of interest too, such as N1s and B1s in the case of doping with Nitrogen and Boron respectively, two common dopants used in LIG.

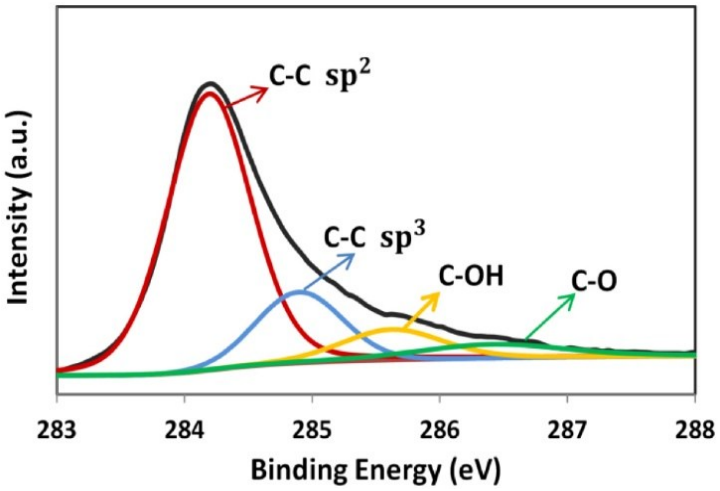

Figure 1.5 Example of typical C1s deconvoluted spectra. Reproduced from [38].

An example of the typical C1s peak spectrum is shown in figure 1.5.[44] As shown in the figure, the C1s peak can be deconvoluted into several contributions, obtaining information regarding the orbital hybridization of C atoms and their bond: C=C sp^2, C-C sp^3, C-OH, and C=O. It is also possible to assign additional peaks, such as an extra pi-pi transition peak and a COOH peak.[45]

The binding energy of the C-C sp^2 peak is 284.5 eV, while the C-C sp^3 peak is at around 285 eV.[46], [47] Functional groups like C-OH, C=O and COOH show positive shifts of about 1.5, 2.5 and 4 eV respectively in the binding energy.[48] In the case of LIG materials, the successful conversion of the substrate into a graphitic material is represented by a high content of sp^2 C-C, and its ratio compared to other C contributions gives information about the quality of the DLW. The Auger spectra can be also used to discriminate the nature of the sp^2 bonding and thus determine if the material presents more similarity to graphite or graphene. The D parameter obtained from the KLL Auger spectrum represents the difference between the maximum and minimum of the first derivative of the C KLL spectrum.[49] More specifically, the typical D values for graphene are 13.5 – 15 eV, while graphite shows a typical value of about 21 eV.[50] The O1s peak gives information on the oxygen content of the LIG sample, an important

parameter when investigating the chemical reactivity, electrochemical activity and hydrophilicity.

Another important tool for the chemical characterisation, specifically for determine the overall quality of the graphene, the number of layers, disorder and defects is the Raman spectroscopy.[51], [52] **Figure 1.6** shows a comparison between the pristine single layer graphene spectrum and the multilayer disordered graphene.[51]

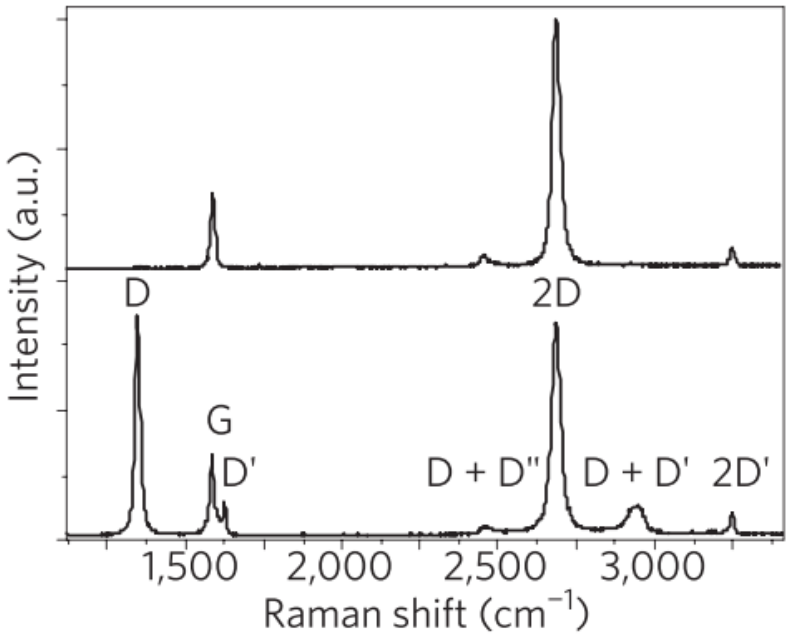

Figure 1.6 Comparison of Raman spectra of pristine single layer (top) and disordered multilayer (bottom) graphene. Reproduced from [51]. Copyright 2013, Nature Publishing Group.

Single layer bare graphene Raman spectra (figure 1.6 top) present two characteristic peaks: the G band, generated by the high frequency E_{2g} phonon, is always located in the range of 1500 – 1630 cm^{-1}.[53] The 2D band, due to breathing modes of the graphene ring, is still present despite the absence of D peak. This has been associated to the conservation of momentum by two phonons with opposite wave vectors.[51] By comparison, the Raman spectrum of disordered multilayer graphene (figure 1.6 bottom) shows an intense D peak usually located at about 1355 cm^{-1} that is associated with the presence of defects in the graphene structure. When comparing graphene-like materials, the degree of disorder can be determined by calculating the intensity

ratio of D to G peak (I_D/I_G), where I_G, is related to modes of sp^2 atoms while I_D is related to six-membered rings.[53] The I_D/I_G ratio correlated to the G band position can be used to discriminate between crystalline and amorphous carbon species (figure 1.7).

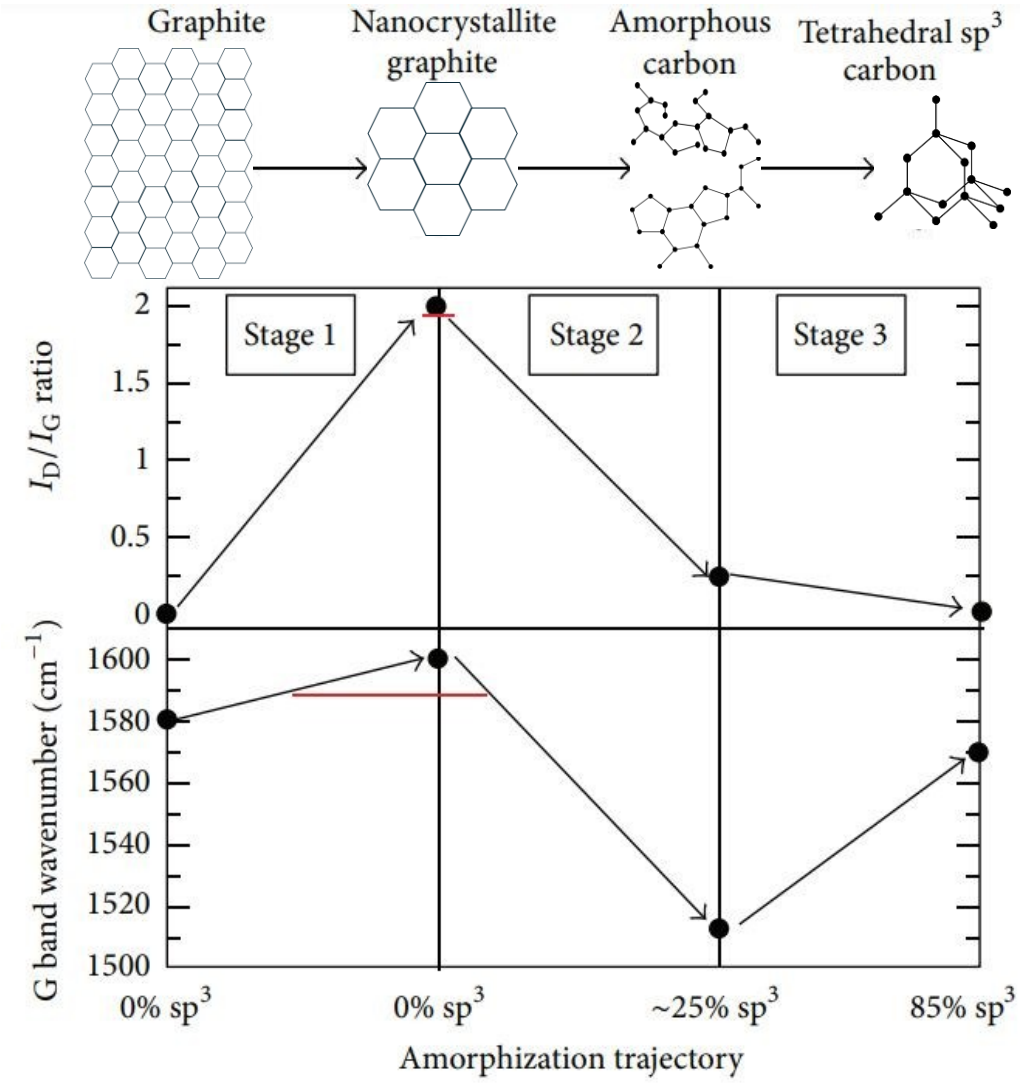

Figure 1.7 Correlation between I_D/I_G ratio and G band position. Reproduced from [42]. Copyright 2013, John Wiley and Sons.

In particular, $I_D/I_G = 0$ is associated to pristine crystalline graphite. As disorder increases, the I_D/I_G ratio will initially increase too. However, further increases of disorder will cause the nano-crystallite graphite to become more distorted and smaller, and its aromatic ring might open eventually turning into amorphous carbon, causing I_D to decrease compared to I_G, and the I_D/I_G ratio to decrease as well.[53] In graphene materials, the 2D peak gives additional information

useful to clarify the crystallinity content of the material. The I_{2D}/I_G ratio is used to give a measure on the layered nature of produced graphitic structures and usually increases with the increase in laser operation coordinates.

1.3.4 Electrochemical characterisation

The LIG's exploded highly porous surface also rich in defects is particularly suitable for electrochemical applications. In fact, the presence of five- and seven-membered carbon rings and oxygen functional groups enhances the catalytic activity of the material by exposing edge defects. These sites, characterized by sp^3 hybridization and functional groups such as carboxyl and ether groups, are more reactive than the basal plane of graphene. The high density of edge defects correlates with fast electrochemical reaction kinetics, making LIG a promising material for sensing and energy applications. For what concerns the electrochemical sensing, LIG is usually used in a three-electrode configuration, whereby LIG is used as working and counter electrode, in combination with Ag/AgCl reference electrode. For energy storage applications, LIG is used as electrode material in combination with an electrolyte solution. Both applications will be discussed more in detail later in this thesis.

The techniques used for electrochemical characterisation are the following:

- **Cyclic voltammetry (CV)** is a potential sweep technique where the working electrode potential is varied linearly in a potential range between two values (switching potentials).
- **Differential Pulse Voltammetry (DPV)** is an electrochemical technique in which small potential pulses are superimposed onto a linear potential ramp. The method measures the difference in current before and after each pulse, producing a peak-shaped waveform. This enhances sensitivity and enables better discrimination of analytes with similar oxidation potentials.[54]

- **Square Wave Voltammetry (SWV)** is a staircase voltammetric technique that applies a symmetric square-wave pulse over a staircase potential waveform. This method minimizes non-faradaic contributions and offers higher sensitivity compared to DPV.[55]
- **Chronopotentiometry (CP)** is a galvanostatic technique where a constant continuous current is applied to the working electrode and the subsequent potential change between working and counter electrode is recorded over time. It is widely used for electrodeposition, material characterization, and reaction kinetics analysis. In CP measurements, a constant current is switched on at time t_o and off at t_1, while the time-dependent potential response is recorded. The response curve typically exhibits key features such as transition time and discharge time, which provide insights into ion transport and concentration dynamics in the electrode/membrane interface. The limiting current density is identified where the apparent resistance reaches a maximum due to co-ion depletion. [56]
- **Electrochemical Impedance Spectroscopy (EIS)** involves perturbing an electrochemical system that is already at a steady state or at equilibrium by applying a sinusoidal AC voltage or current across a broad frequency range. The system's response, in the form of a corresponding sinusoidal current or voltage, is then recorded. Since the electrochemical system is assumed to be linear and time-invariant meaning its output remains proportionally related to the input without changing over time- EIS functions as a transfer function technique. It characterizes the relationship between the applied AC signal and the resulting system response across various frequencies.[57]

To perform a qualitative analysis of the behaviour of an electrode CV is the most suited technique, while other voltametric or amperometric methods are more suited for quantitative analysis. This is due to the inherent limitations in the precision of peak current measurements obtained from CV, superimposed to a background charging current, resulting in uncertainties

during correction. Electrochemical techniques such as chronoamperometry, EIS, DPV, SWV etc. are frequently employed, with the latter two methods offering the advantage of being unaffected by charging phenomena.[58]

The electrode-solution interface is where the heterogeneous electrochemical reaction take place. The reaction rate is an important parameter in electrochemistry and depends on both the kinetics of electron transfer at the surface and the mass transfer of analyte towards the electrode. When convection is absent, the only contributions to mass transfer come from migration (molecule's movement as consequence of a potential gradient) and diffusion (molecule's movement as consequence of a concentration gradient). To simplify the electrochemical reaction, it is possible to use a supporting electrolyte composed of an excess concentration of non-electroactive ions. This will eliminate the potential gradient, so that the mass-transfer mechanism is dominated by diffusion.[58]

The kinetics associated with electron transfer at electrode surfaces are represented by the universal heterogeneous electron transfer (HET) rate constant, denoted as k_0 (cm s^{-1}). In the context of reversible electrochemical reactions, a potential difference, ΔE_P, of 59/n mV is observed at 25 °C, where n represents the number of electrons participating in the charge transfer process.[58] This ΔE_P value is typically observed during cyclic voltammetry (CV) of LIG electrodes, characterized by high k_0 values at low scan rates (v). However, as v increases significantly, the rates of electron transfer begin to compete with the rate of the varying potential.[59] This results in a positive shift in the peak position for oxidation and a negative shift in the peak position for reduction, causing an overall increase in ΔE_P. The region in which electrode reactions are classified as *quasi-reversible* (200 mV > ΔE_P > 60 mV) is particularly valuable for examining the kinetics of these reactions. This analysis is facilitated by the Nicholson method,[59] which correlates ΔE_P and ν to k^0 through dimensionless parameter Ψ:

$$\Psi = k^0\left(\frac{D_O}{D_R}\right)^{\frac{\alpha}{2}}\sqrt{\frac{RT}{n\pi F D_O \nu}}$$

where D_O and D_R are the diffusion coefficients of the oxidised and reduced analyte forms respectively, α is charge transfer coefficient, R is the universal gas constant, T is temperature in °Kelvin, F is the Faraday's constant and n is number electrons transferred in the redox reaction. Ψ is derived from ΔE_P by the equation,[60]

$$\Psi = \frac{(-0.6288 + 0.0021 n \Delta E_P)}{(1 - 0.017 n \Delta E_P)}$$

Conducting a characterization of a standard redox couple, such as $[Fe(CN)_6]^{3-/4-}$, provides a framework for comparing the electrochemical performance of various LIG electrodes alongside other electrode materials. In the context of a diffusion-controlled reversible reaction, the relationship between the peak current (I_P) in cyclic voltammetry (CV) and the varying potential scan rate (ν) is described by the Randles-Sevcik equation[61], [62]:

$$I_P = 0.4463\ nFAC \left(\frac{nFvD}{RT}\right)^{1/2}$$

where A denotes the electrochemically active area of the working electrode in square centimetres (cm^2), C is the bulk concentration of the redox species (mol/cm^3), with all other symbols retaining their previous definitions.

The primary conclusion drawn from this equation is that the current response (I_P) is directly proportional to the square root of scan rate ($\nu^{1/2}$). This linear relationship provides clear evidence of the reversible nature of electrode reactions, consistent with theoretical predictions. Furthermore, the equation facilitates the determination of electroactive area of the working electrode. The unique microstructural features of LIG enable the analyte to interact with a broader surface area than the 2D area of the electrode. By analysing the impedance profile provides insights into the interactions between the analyte and the intricate peaked, valleyed, and porous architecture.

1.3.5 Electric Double-Layer Capacitance (EDLC)

According to the Electric Double-Layer Capacitance (EDLC) mechanism, energy is stored electrostatically through a non-faradic charge separation at the electrode–electrolyte interface. In an EDLC, ions in the electrolyte accumulate on the surfaces of active carbon electrodes of opposite polarity, forming an electric double layer (EDL) when the capacitor is charged. Positive and negative charges accumulate on opposite electrodes across a separator, as illustrated in figure 1.8.

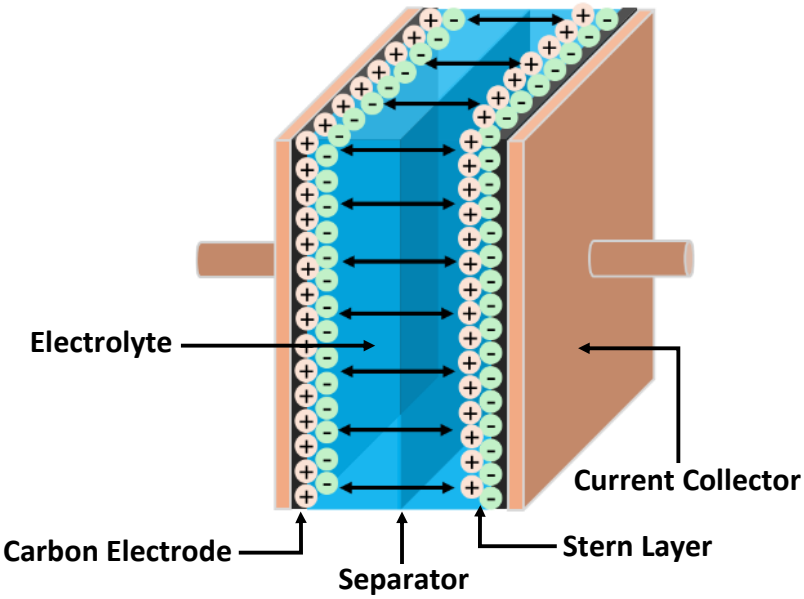

Figure 1.8 Schematic illustration of charge separation between oppositely charged electrodes through electric double layer capacitance (EDLC) mechanism. Adapted from [63]. Copyright 2024, Elesevier.

Stern Model of Electrical Double Layer

The Stern model,[64] proposed in 1924, combined the Helmholtz and Gouy–Chapman models, to describe the interfacial charging phenomena. This model refines earlier EDL theories by combining the compact layer (Helmholtz) concept[65] with the diffuse layer (Gouy–Chapman) description[66], while recognizing finite size of ions and their hydration shells. According to Stern:

- Ions have nonzero radius, so their centres cannot approach the electrode closer than the hydrated radius.
- Some ions can be temporarily adsorbed to the surface by electrostatic or van der Waals interactions, overcoming thermal motion.

In more advanced treatments, specific adsorption via covalent, coordination, or hydrogen bonding is also considered. In the Stern model, the EDL is divided by a Stern plane (approximately one hydrated-ion radius away from the electrode) into two regions:

- **Stern (Compact) Layer**

  This layer (sometimes called the Helmholtz layer) contains ions and solvent molecules closely bound to the electrode surface. The potential drop across it is nearly linear, behaving like a parallel-plate capacitor. It is bounded by the Inner Helmholtz Plane (IHP) (for specifically adsorbed species) and Outer Helmholtz Plane (OHP) (for solvated ions).

- **Diffuse (Gouy–Chapman) Layer**

  Beyond the Stern plane lies the diffuse zone, where ions are mobile and distributed following the Boltzmann distribution. Here the potential decays exponentially into the bulk electrolyte. The characteristic screening length is the Debye length.

Mathematically, the total EDL capacitance C_{dl} is expressed as a series combination:

$$\frac{1}{C_{dl}} = \frac{1}{C_H} + \frac{1}{C_D}$$

where C_H is the compact (Helmholtz) layer capacitance, and C_D is the diffuse (Gouy–Chapman) capacitance. At high ionic strength, C_D becomes large (diffuse layer is thin), and C_{dl} approaches C_H. At low ionic strength, the diffuse contribution becomes significant.

In supercapacitors, energy storage primarily arises from charge separation within the EDL as described by the Stern model. This model helps explain how ion concentration, dielectric properties, and surface potential influence overall capacitance. Porous electrodes such as activated carbon or graphene,[67] with high surface areas and tunable surface chemistry, enhance

the EDL capacitance.[68] As this charge storage mechanism is non faradaic in nature and does not involve electron transfer or redox reactions at electrode surface, the electrode materials and their structure remain unaltered over time providing extended cycle life and fast charge–discharge kinetics. The capacitive behavior of EDLCs is commonly characterized by cyclic voltammetry (CV) and galvanostatic charge–discharge (GCD). Experimentally, non-ideal capacitive behaviour observed in electrochemical impedance spectroscopy (EIS) and cyclic voltammetry is often modelled using equivalent circuits containing constant phase elements (CPEs) to account for surface roughness and structural heterogeneity.

Limitations of the Stern Model

Although the Stern model significantly improves upon earlier Helmholtz and Gouy–Chapman models, it has certain limitations:

- It does not fully account for specific ion adsorption via covalent or coordination interactions.
- It neglects solvent reorganization near the electrode interface.
- It oversimplifies finite ion size and confinement effects in nanoporous electrodes.

1.3.6 Non-faradaic (charging or capacitive) currents

In voltametric experiments, the total measured current consists of two components:

- **Faradaic currents:** Originating from charge transfer during redox reactions, and
- **Non-faradaic currents:** Arising from electrical double layer (EDL) at the electrode–electrolyte interface during charging and discharging of the electrochemical system.

When the electrode potential is varied during a scan, ions in the electrolyte rearrange near the electrode surface to maintain charge balance. This redistribution generates a time-dependent charging current even in the absence of any electrochemical reaction. Such current reflects electrostatic charge storage within the EDL rather than any chemical transformation at the

electrode. The charging current (i_c) is directly proportional to both the double-layer capacitance (C_{dl}) and the scan rate (dV/dt),[58] and is expressed as:

$$i_c = C_{dl}\frac{dV}{dt}$$

Thus, the faster the potential is swept, the greater the charging current observed. This relationship is frequently used to estimate C_{dl} by measuring i_c at different scan rates.

In cyclic voltammetry (CV), charging currents appear as rectangular or triangular background currents in the absence of redox peaks. This shape is characteristic of purely capacitive behaviour, such as that observed in electric double-layer capacitors (EDLCs), where current reverses instantaneously with the change in scan direction due to rapid charging and discharging of the EDL.

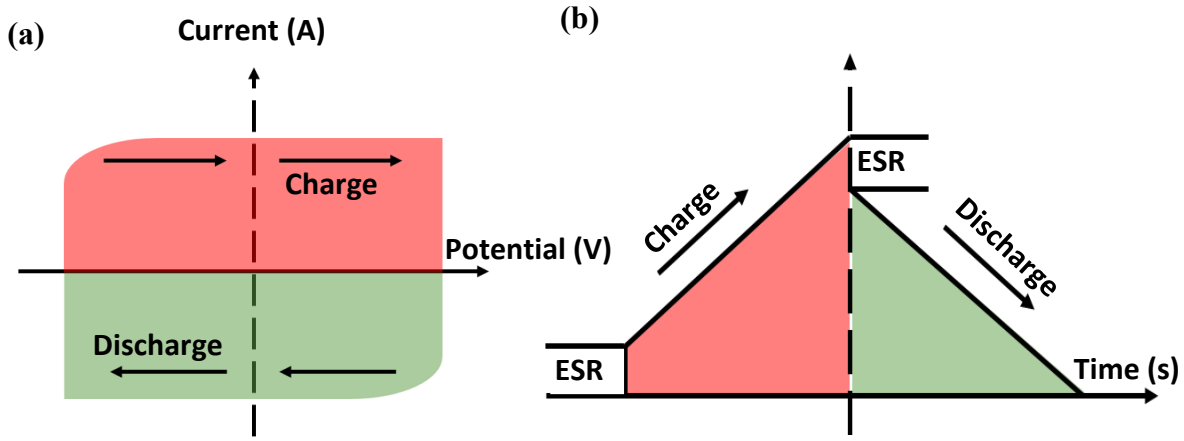

Figure 1.9: (a) Idealized cyclic voltammogram (CV), (b) Galvanostatic charge-discharge (GCD) illustrating charging currents in a purely capacitive system. Adapted from [69]. Copyright 2018, ACS Publications.

The cyclic voltammetry (CV) plot exhibits a rectangular-shaped current–potential (i–V) curve (Figure 1.9a), while the corresponding galvanostatic charge–discharge (GCD) profile displays a triangular chrono-potentiometric (V–t) curve (Figure 1.9b). These shapes are characteristic features of electric double-layer capacitive (EDLC) behaviour. During the forward potential sweep, current flows as the electrical double layer (EDL) charges, resulting in a nearly constant

current plateau. Upon reversal of the potential, the current polarity inverts symmetrically, representing the discharge of the EDL. The absence of redox peaks confirms a non-faradaic process, in which energy storage occurs purely through electrostatic charge separation at the electrode–electrolyte interface. In the GCD curve, a small voltage (IR) drop is typically observed at the start of the discharge process, attributed to the equivalent series resistance (ESR) of the system. This ESR originates from the solution resistance and the interfacial resistance at the electrode–electrolyte boundary, both of which influence the overall power performance of the supercapacitor.[70]

1.3.7 Equivalent Circuit Models

The electrochemical behaviour of the electrode–electrolyte interface can be represented by electrical equivalent circuit models (ECMs), which describe the interfacial charging processes—particularly in systems dominated by non-faradaic (capacitive) behaviour. These models are essential for interpreting data obtained from Electrochemical Impedance Spectroscopy (EIS) and for understanding charge transfer resistance, ion transport, and double-layer formation at the interface.[71] The two most commonly used ECMs to fit EIS data for non-faradaic interfaces, such as in Electric Double-Layer Capacitors (EDLCs), are the R–C model and the R–CPE model.

R–C Equivalent Circuit Model

In its simplest form, the electrode–electrolyte interface can be modeled as a resistor (R) and a capacitor (C) connected in series or parallel.

- The solution resistance (R_s) represents the combined resistance of the electrolyte, separator, wiring, and electrode material. It accounts for all frequency-independent ohmic losses within the system.

- The double-layer capacitance (C_{dl}) represents the ability of the electrical double layer (EDL) at the interface to store charge electrostatically. In the ideal case, this capacitor models a perfect, purely capacitive charge–discharge process.

In a non-faradaic system, such as an EDLC, no charge transfer occurs across the electrode–electrolyte interface. The R–C model effectively captures the electrostatic behavior of such systems. In EIS, the Nyquist plot typically exhibits a near-vertical line at low frequencies, characteristic of ideal capacitive behaviour. The impedance of a simple R–C circuit is given by:

$$Z(\omega) = R_s + \frac{1}{j\omega C_{dl}}$$

where ω is the angular frequency and $j = \sqrt{-1}$.

R–CPE Equivalent Circuit Model

In practical systems, the electrode–electrolyte interface rarely behaves as a perfect capacitor due to surface roughness, porosity, inhomogeneous current distribution, and non-uniform ion adsorption. To account for this non-ideal capacitive behavior, the capacitor in the R–C model is replaced by a Constant Phase Element (CPE).[72]

The impedance of a CPE is expressed as:

$$Z_{CPE} = \frac{1}{Q(j\omega)^n}$$

where:

Q is the CPE constant (with units of $F \cdot s^{n-1}$),

n is the phase factor ($0 \leq n \leq 1$), indicating deviation from ideal capacitive behavior.

When n =1, the CPE behaves like a pure capacitor; when n=0, it behaves like a pure resistor. Intermediate values of n represent distributed or fractal interfaces, typical of porous or heterogeneous electrodes commonly used in supercapacitors. The R–CPE model is thus widely used in EIS fitting to represent non-faradaic interfacial charging processes exhibiting frequency-dependent capacitance.

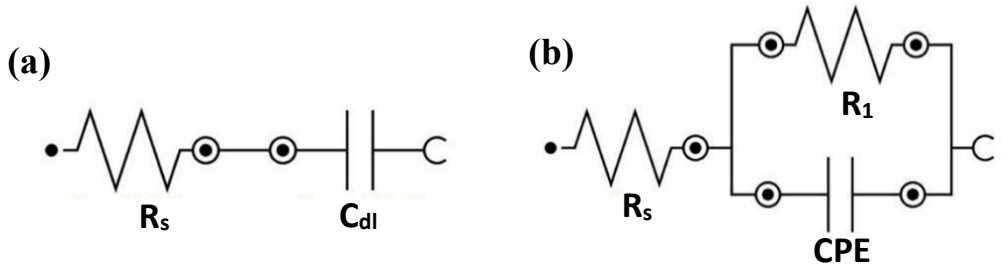

Figure 1.10 Equivalent circuit models for non-faradaic electrode–electrolyte interfaces. **(a)** R–C model, representing solution resistance (R_s) in series with double-layer capacitance (C_{dl}). **(b)** R–CPE model, where the ideal capacitor is replaced by a constant phase element (CPE) to account for surface roughness and non-uniform charge distribution.

Non-Faradaic Systems and EIS

These models are widely applied in EIS fitting to interpret the capacitive behaviour of electric double-layer capacitors (EDLCs) and other non-faradaic electrochemical systems. In non-faradaic systems, such as EDLCs, charge storage occurs solely via electrostatic accumulation of ions within the EDL, with no electron transfer or redox reaction taking place. Equivalent circuit models such as R–C and R–CPE accurately describe the frequency-dependent impedance associated with this process.[58] Since non-faradaic interfaces do not involve charge transfer (redox reactions), they do not include the parallel (Charge Transfer Resistance) or the Warburg element (Z_W) typically found in the Randles circuit, which is used for faradaic (redox-active) systems. In a typical EIS analysis:

- The high-frequency region corresponds to the solution resistance (R_s).
- The mid-to-low frequency region reflects double-layer charging, represented by C_{dl} (ideal case) or CPE (non-ideal case).
- A near-vertical line in the Nyquist plot signifies ideal capacitive behaviour, whereas a tilted line indicates non-ideal or distributed capacitance due to electrode heterogeneity.

1.4 LIG electrochemical properties

LIG has emerged as a particularly advantageous electrode material, due to its adjustable surface properties, high surface area and density of defects. To establish the suitability of LIG for electrochemical applications, its performance has been assessed using standard redox mediators. The as-fabricated LIG, without any surface modifications, has shown rapid electron transfer kinetics for a range of reactions. The electron transfer kinetics of the ferri/ferrocyanide reaction ($[Fe(CN)_6]^{3-/4-}$) or the hexa-amine-ruthenium reaction ($[Ru(NH_3)_6]^{2+/3+}$) have been utilized for LIG electrode characterization, given their well-documented and reversible one-electron transfer nature. Nayak et al., in their pioneering study on LIG-based electrochemical sensors fabricated via DLW of PI using a CO_2 laser, evaluated the heterogeneous electron transfer (HET) rate constant (k_0) for both inner-sphere and outer-sphere redox mediators.[73] For $[Fe(CN)_6]^{4-}$ and $[Ru(NH_3)_6]^{3+}$, the HET rate constants were determined to be 0.1150 $cm \cdot s^{-1}$ and 0.0868 $cm \cdot s^{-1}$, respectively-significantly higher than those reported for similar carbon-based electrodes. This enhancement was attributed to the binder-free 3D porous structure of LIG, which provides an abundance of edge-plane sites. Furthermore, the anchoring of Pt nanoparticles on LIG further improved k_0 to 0.2823 $cm \cdot s^{-1}$ and 0.2312 $cm \cdot s^{-1}$ for inner- and outer-sphere redox mediators, respectively, due to their additional catalytic contribution.[73]

Interestingly, Burke et al. [38] reported that LIG produced from inexpensive diode laser (450nm) showed promising sensing capabilities that are comparable with LIG electrodes fabricated with CO_2 laser engravers and with other carbon allotropes.[73] In their study, the authors employed a three-electrode system**,** with LIG as the working electrode**,** a Pt wire as the counter electrode**,** and Ag/AgCl as the reference electrode **(**figure 1.11**)**. They observed a minimum peak potential difference (ΔE_P) of 74.5 mV for the $[Ru(NH_3)_6]^{2+/3+}$ redox mediator, which is lower than the average ΔE_P value of 85.6 mV reported for pristine LIG fabricated using a CO_2 laser.

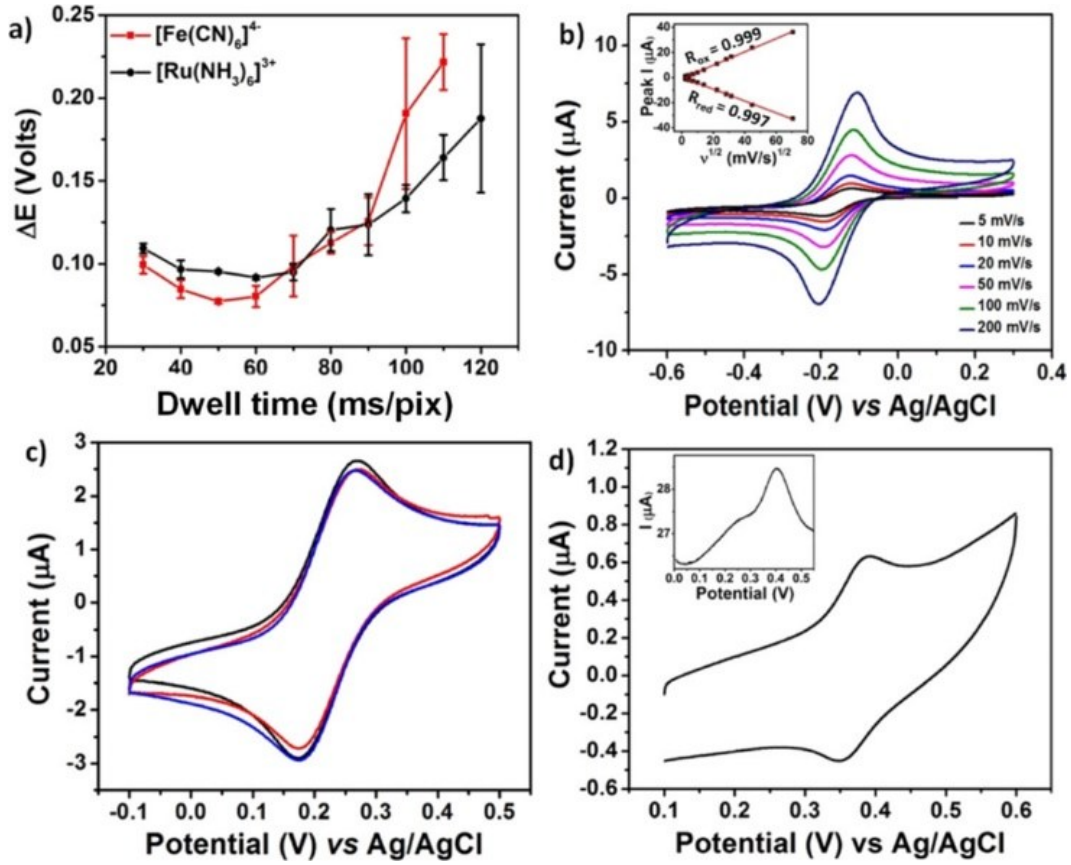

Figure 1.11 Electrochemical characterisation of LIG electrochemical sensors. **a)** ΔE_p for 5 mM $[Ru(NH_3)_6]^{2+/3+}$ and $[Fe(CN)_6]^{3-/4-}$ electrolytes; **b)** CV of LIG electrodes at different scan rates using $[Ru(NH_3)_6]^{2+/3+}$ electrolyte (inset: oxidation peak currents vs. square root of potential scan rates); **c)** CV of LIG electrodes at different scan rates using $[Fe(CN)_6]^{3-/4-}$ electrolyte; **d)** CV of benzocaine (0.5 mM) at LIG working electrode (inset: SWV response of the same). Reproduced from [38]. Copyright 2020, ACS Publications.

This result aligns with the 74.5 mV average ΔE_P value recorded for Hybrid LIG/Pt electrodes in previous studies.[73] Similarly, for the $[Fe(CN)_6]^{3-/4-}$ redox system, they found a ΔE_p value of 85.6 mV, which closely matches the literature-reported average value for pristine LIG electrodes.[73] The average HET rate constant (k_o) value for $[Ru(NH_3)_6]^{2+/3+}$ electrolyte was 0.0146 ± 2.08 cm/s, which was comparable to other sp^2 carbon materials, such as graphene on a copper electrode ($(15 \pm 2) \times 10^{-3}$ cm/s) and Q-graphene (18×10^{-3} cm/s) reported in literature.[74], [75] The authors also found favourable electron transfer (ET) kinetic compared to those of single layered graphene (1.1×10^{-3} cm/s), quasi-graphene (1.6×10^{-3} cm/s), and

graphite-based electrodes (edge plane pyrolytic graphite EPPG = 8.8 × 10^{-3} cm/s and basal plane pyrolytic graphite BPPG = 38 × 10^{-3} cm/s).[76] The uniqueness of this result originates from the nature of the $[Ru(NH_3)_6]^{2+/3+}$ electrolyte as an outer-sphere redox mediator, which is insensitive to the electrode surface structure and the presence of oxygen-containing species. Instead, its electron transfer process is primarily influenced by the density of electronic states (DOS) at the electrode. As a result, the reversible redox reaction on the LIG electrode is primarily enabled by the increased density of electronic states (DOS) at the graphene edges, which are more reactive than the basal planes. This enhanced DOS, combined with the highly porous 3D structure at edge sites, facilitates faster electron transfer kinetics, improving the overall electrochemical performance.[38]

Using an inner-sphere redox mediator, $[Fe(CN)_6]^{3-/4-}$ electrolyte, that is sensitive to both the electrode surface structure and oxygen content, the average heterogeneous electron transfer (HET) rate constant (k_0) was determined to be (13 ± 1) × 10^{-3} cm·s^{-1}. This value is comparable to HET rate constants reported for CVD-grown graphene (CVD-Gr) and Q-graphene.[73], [74]

1.5 LIG electrochemical sensors from visible lasers

Following the establishment of LIG suitability for electrochemical applications, many authors have reported its use for sensing. In a pioneering work from Vaughan et al.[77], LIG electrodes fabricated with visible laser were used to detect and differentiate different biomarkers such as dopamine (DA), ascorbic acid (AA) and uric acid (UA) in solution. To this end, a mixture solution of DA (1 mM), AA (1 mM), and UA (1 mM) in 0.1 M phosphate buffer saline (PBS) was investigated via CV and DPV (figure 1.12).

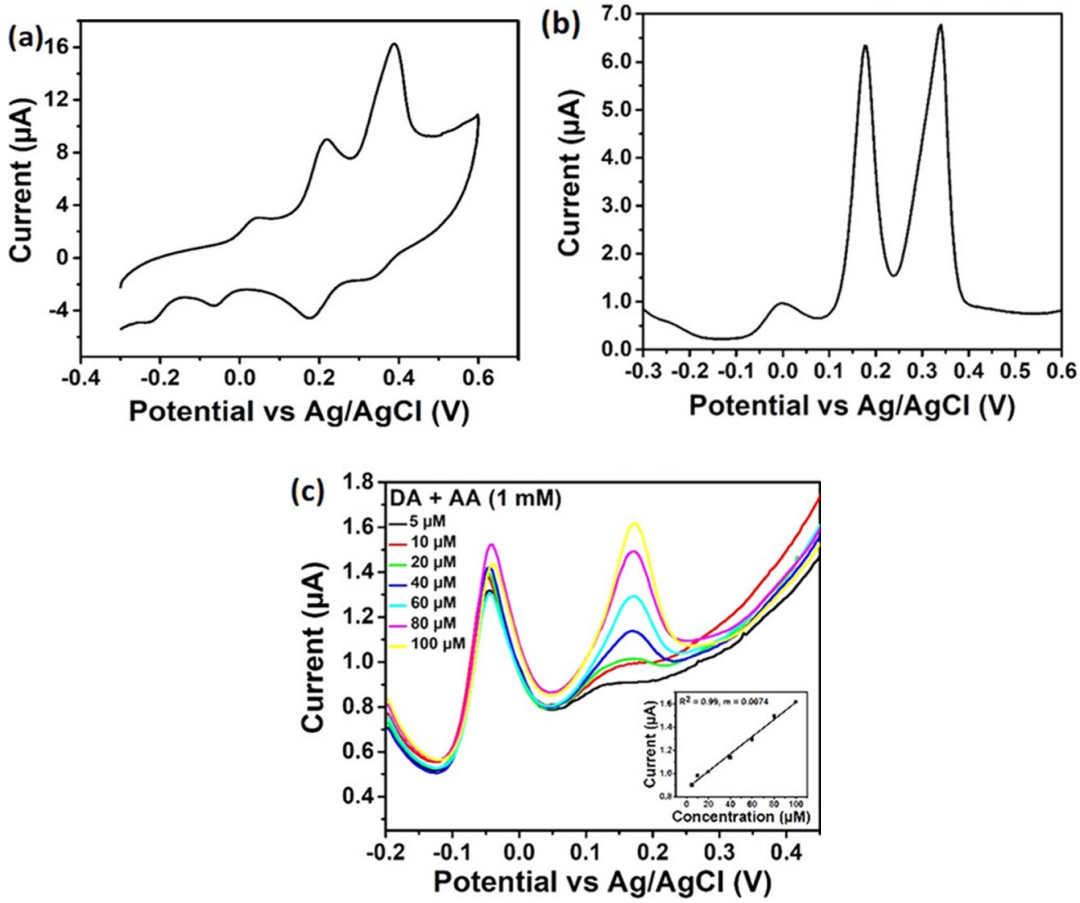

Figure 1.12 a) CV and **b)** DPV of 1 mM DA, 1 mM AA, and 1 mM UA in 0.1 M PBS; **c)** DPV response of DA at different concentrations in 0.1 M PBS in presence of 1 mM AA (inset: concentration vs current response for DA with same setup). Reproduced from [67]. Copyright 2020, ACS Publications.

As shown in figure 1.12a, the CV scan performed on the mixture of the three biomarkers at 100 mV/s scan rate presented well-defined oxidation peaks at 0.218 V (corresponding to DA), 0.044 V (corresponding to AA), and 0.389 V (corresponding to UA). The good separation of these oxidation peaks reflected the capacity of LIG electrodes for the selective analysis of separate species, superior to screen printed electrodes. Good peak separation was also observed for the DPV analysis of the same system (figure 1.12b), further confirming the possibility to easily identify concomitant species. The observed peak potential separation values were smaller than those reported for graphene-based electrodes and were comparable to those of graphitic carbon electrodes with enhanced catalytic properties. These improvements have been previously achieved through post-deposition of Pt or PEDOT on the surface of LIG materials synthesized

via CO_2 DLW of PI.[73], [78] This high selectivity observed in the LIG graphitic carbon electrode material was attributed to a synergistic effect of improved electron transfer linked to its porous structure, increased catalytic activity influenced by its abundance of edge planes and functional groups available on LIG surface, and extensive 3D porous structure to facilitate the accessibility of molecules. DPV of dopamine (DA) at different concentrations ranging from 5 to 100 µM shows prominent responses while maintaining a constant concentration of 1 mM ascorbic acid (figure 1.12c). In this case it was observed an increase in the oxidation peak current at 0.172 V, associated to the increase in dopamine (DA) concentration, while conversely oxidation peak at −0.44 V, related to ascorbic acid (AA), showed minimal variation in current response. This, once again, highlighted the electrode's strong ability to differentiate between potentially interfering species. Moreover, it is important to note that in this reported work the LIG electrode was fabricated using inexpensive and low-power blue lasers (450 nm) typically employed by hobbyists, and they were utilized without any subsequent enhancement processes obtaining results that were comparable with those reported in literature for electrodes produced with expensive and high-power CO_2 laser engravers as well as post-fabrication enhancements like Pt or PEDOT deposition to improve their electrocatalytic properties.[63, 68] Additionally, compared to earlier reported electrodes fabricated through 405 nm laser treatment, the electrodes Eoghan et al. reported [77] still exhibited greater sensitivity for dopamine (DA) and enhanced distinguishing capabilities from mixtures of DA, AA and UA. These results are particularly important, as they pave the way to the possibility to develop highly sensitive LIG electrode for biosensing application at a relatively low-cost and with low footprint impact.

1.6 Direct Laser Writing for Green LIG (gLIG) Production

Recently, there has been increased interested in using substrate materials beyond PI to produce LIG. Particularly, significant advancements have been reported in the fabrication of green LIG (gLIG) materials from renewable, eco-friendly bio-based carbon sources. This innovation has enabled the development of sustainable materials and their use into electronic devices, offering solutions to the increasingly concerning issue of electronic waste (e-waste) cause by disposal of electronics.[79] Various natural substrate materials such as coconut husks, wood and barks (cork), as well as paper and cloth have been proposed as precursors for green DLW, due to their abundance, renewability and opportunities for upcycling of wate from biomass.[80] These use natural bio-sources can be classified in different categories, depending on their composition:

- **Cellulose**, an extremely abundant carbohydrate polymer that is the main component of plant cells' walls.[79], [81] This aliphatic compound can be further processed to fabricate paper and cotton textiles.[81] Its structure in composed of β-1, 4-linked glucose monomers with approximately equal quantity of elemental carbon and oxygen in its functional groups. These monomers form complex structures such fibrils and fibres through hydrogen bonding between oxygen containing functional groups both at intra and intermolecular levels.[79]
- **Lignocellulose materials** originate from natural raw materials such as wood, cork, and leaves and are characterised by the presence of aromatic chemical structures, which facilitate conversion and aromatisation.[79], [82] For example, lignin is an amorphous, branched aromatic polymer, rich in benzene rings bound to various functional groups. Its structure consists of three distinct aromatic ring substitution patterns: guaiacyl, p-hydroxyphenyl, and syringyl monomers.[79]
- **Chitosan**, a bio-product of chitin deacetylation. Its structure is a copolymer of D-glucosamine and N-acetyl-D-glucosamine in different percentages that depend on the degree of deacetylation. Moreover, the presence of positive ionic charge on chitosan makes it

possible to bind it to negatively charged substances.[83] Chitosan can be sourced from exoskeletons of crustaceans, crabs and shrimps, whose high porosity, biodegradability, non-toxicity and biocompatibility have already made it the ideal candidate for bioengineering applications.[84], [85] Chitosan-based films have already shown compatibility with screen printing techniques, with a Young's modulus of 151 kPa, good electrochemical response and biocompatibility suitable for wearable sensing applications.[86]

1.6.1 Direct Laser Writing for gLIG production from bio-sources

The formation mechanism of gLIG from bio-sources via DLW technique follows similar principles of those presented earlier in this chapter for the conversion of synthetic polymers: graphitization takes place through photo-thermal and/or photochemical mechanisms, leading to the transformation of surface carbon atoms from sp^3 to sp^2 hybridization. The specific chemical reactions involved in DLW process are largely influenced by the composition of substrate materials based on aromatic or aliphatic monomer units. Additionally, the choice of laser system and its operational parameters play a crucial role in governing this conversion process, particularly by affecting bond cleavage, molecular rearrangement, and the efficiency of synthesizing the graphitic carbon structures characteristic of gLIG. (figure 1.13).[79]

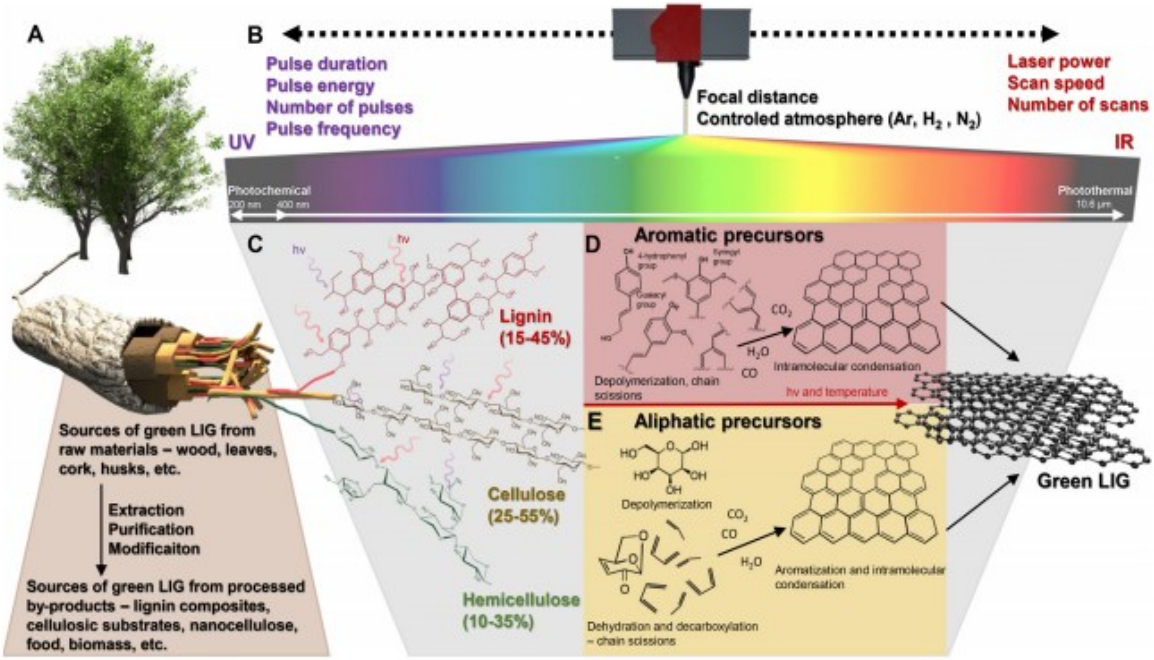

Figure 1.13 Conversion mechanism of gLIG, a) bio-sources, b) laser parameters, c) molecular structure of lignocellulose biopolymers, d) aromatic and e) aliphatic precursors. Reproduced from [79]. Copyright 2022, AIP Publishing.

In the context of gLIG synthesis, the interplay of photochemical and thermochemical mechanisms promotes the bonds breaking and rearrangement within chemical structure of natural organic polymers. The possibility of certain bonds being degraded and cleaved through photochemical processes is influenced by the chemical composition of substrate materials and the characteristics of the selected laser source causing depolymerization of the polymeric structure and the cleavage of unwanted carbon-oxygen bonds.[79] The incident laser pulse radiation produces phonons within the substrate material, which possess quantized vibrational energies that can break weaker bonds leading to micro-ablation along with the release of volatile gaseous materials that become ionized, creating a plasma discharge that is marked by bright flashes on the surface irradiated material.[79], [87] This plasma plume acts as a protective barrier, limiting further laser penetration while simultaneously generating intense localized temperatures. These extreme conditions promote carbonization and graphitization by

facilitating the rearrangement of cleaved carbon bonds through aromatization and condensation processes. As a result, sp^2 carbon-rich lattice domains characteristic of gLIG are synthesized.[79] According to Chyan et al.,[80] any carbon-based material capable of producing amorphous carbon can be converted into gLIG. In their work, they implemented a two-steps DLW process where the first step resulted in formation of amorphous carbon, and the second step induced its conversion in laser induced graphene. When applying the two-steps DLW process to natural substrates, they found out that the fabrication of gLIG from wood required an inert atmosphere to mitigate the risk of ablation, resulting in the production of high-quality LIG with a sheet resistance as low as 10 Ω/sq. Their findings indicated that a higher lignin concentration in the wood contributed to improved LIG quality, highlighting the critical role of cross-linked aromatic structures in the precursor.[80] Another study by Ye et al.[88] highlighted the benefits of lignin in comparison to cellulose and hemicellulose, pointing out that the aliphatic components of cellulose are more susceptible to rapid decomposition during laser treatment than those of lignin (figure 1.13c**)**.

As mentioned previously in this chapter, the quality of gLIG is influenced by both the laser parameters employed in its production and the specific type of substrate used. The latter can be divided into two primary categories: **(i)** natural raw materials, such as wood, leaf, bark etc. and **(ii)** derived from natural raw materials as processed by-products, such as lignin and cellulose. The processed by-products can be engineered into various forms, including lignin-rich polymers and composites, exhibiting diverse mechanical properties such as grammage (g/m^2), porosity, pore size, flexibility, and transparency. Furthermore, these polymeric precursors can be functionalized with additional chemicals to formulate specialized inks and bio-composites, expanding their potential applications. Additionally, alternative sources, including agricultural husks and food waste, have demonstrated potential as effective materials for gLIG production, leading to the creation of high-performance electronic devices (figure 1.13d, e).[89]

1.6.2 Green Laser Iinduced Graphene (gLIG) from Cork

gLIG can be obtained from cork, a naturally occurring and renewable material harvested every 9 to 12 years from the bark of *Quercus suber L.* tree. Unlike wood, cork contains lower levels of cellulose and hemicellulose but is rich in lignin (18%), an aromatic biopolymer, suberin (40%) and wax, having both aliphatic and aromatic characteristics.[90] On a microscopic scale, cork exhibits a honeycomb-like structure composed of hollow cells arranged in pentagonal and hexagonal patterns, with cell walls rich in suberin and lignin, making it highly water-resistant (figure 1.14). This combination of a high surface area, hollow structure, and unique chemical composition gives cork remarkable properties such as being lightweight, fire-resistant, low-density, highly compressible, and possessing low thermal conductivity, leading to its widespread use in applications like bottle stoppers, seals, acoustic insulation, and even as thermal insulation and vibration-damping material in spacecraft.

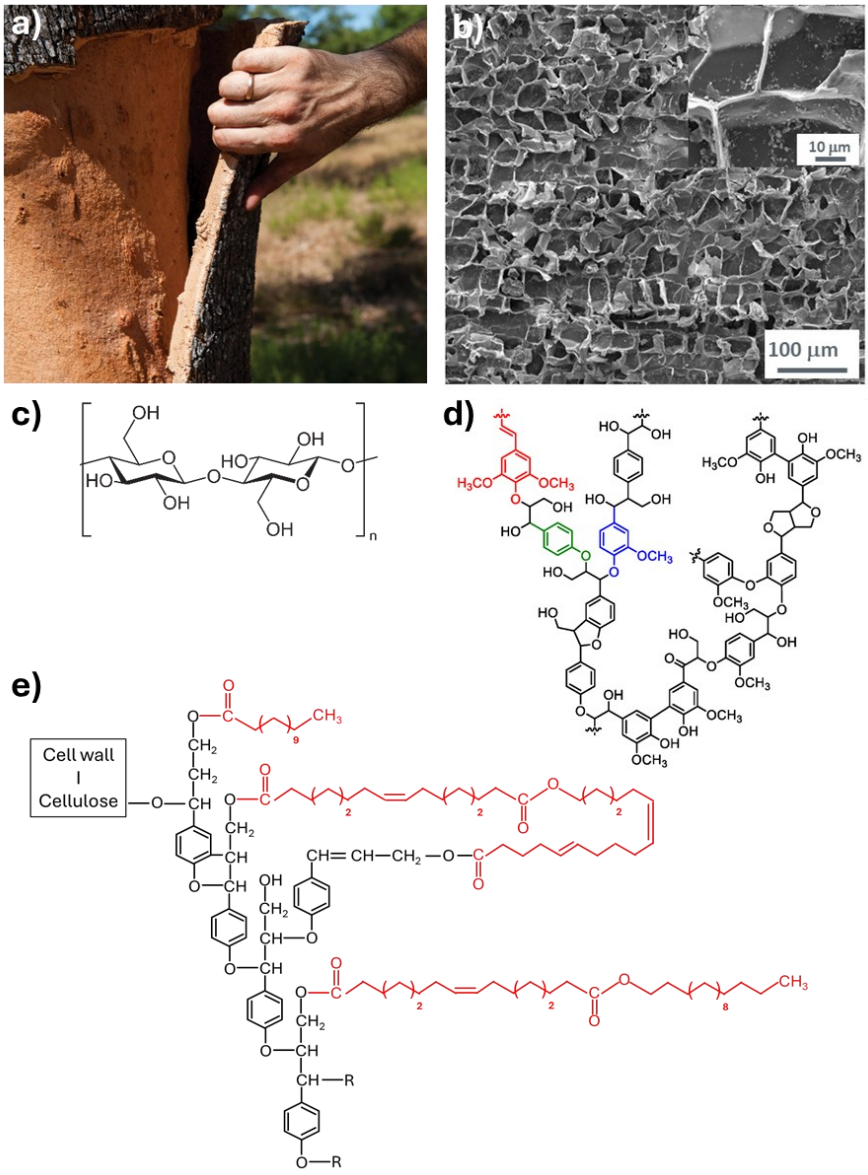

Figure 1.14 (a) Image of Cork wood cultivation, (b) SEM image of LIG on Cork substrate, Chemical structure of (c) cellulose, (d) lignin and (e) suberin [91]

Recent advancements in direct laser writing (DLW) techniques have led to the possibility of generating gLIG from cork. Similarly to the process observed for the conversion of polyimide to LIG, a highly localized and point-specific laser treatment at elevated temperatures and pressures induces carbonization, transforming the cork surface into LIG, which is characterized by typical Raman spectroscopic peaks of graphene-like materials, with I_{2D}/I_G ratios > 0.6, I_D/I_G ratios close to 1, and low sheet resistances (< 100 Ω sq^{-1}).[92], [93] The resulting LIG also features a three-dimensional, porous structure with a high surface area and a high density of defects,

making it suitable for applications in electrochemical sensing and energy harvesting/storage technologies. The conversion mechanism of π-ring-containing natural polymers in cork into graphitic structures is proposed to be driven by the absorption of photon energy from the laser, which transforms into high pressure and temperature, causing localized explosions that induce carbonization. This process occurs at high speeds, limiting the availability of environmental oxygen and moisture, thereby preventing full oxidation into gaseous products such as CO_2 or NO_x and avoiding complete ablation. However, trace amounts of oxygen in the environment lead to a limited degree of oxidation, producing gaseous by-products that contribute to the observed porous structure of the LIG. Thus, the production of gLIG from cork not only offers a sustainable approach to synthesizing conductive carbon materials but also aligns with the growing emphasis on eco-friendly technologies, highlighting its potential for advanced applications in energy storage and sensor technologies.

1.6.3 gLIG from Chitosan

In 2019, global crustacean production exceeded 16 million metric tonnes, generating substantial waste as approximately 60% of crustaceans are inedible.[94] This waste primarily consists of chitin, the second most abundant natural polysaccharide after cellulose, which is a key structural component of crustaceans' exoskeletons and is valued for its biocompatibility and biodegradability.[95] Chitin can be converted into chitosan through enzymatic or chemical deacetylation, enhancing its solubility and expanding its potential applications.[96] Due to its non-toxicity, biodegradability, and biocompatibility, chitosan is extensively utilized in biotechnology, including implants, drug delivery systems, as well as in cosmetics, food packaging, and dietary supplements.[97] The valorisation of crustacean waste into chitosan not only mitigates waste accumulation but also aligns with the United Nations Sustainable Development Goals (SDGs) by advocating utilization of sustainable resources and waste management.[95]

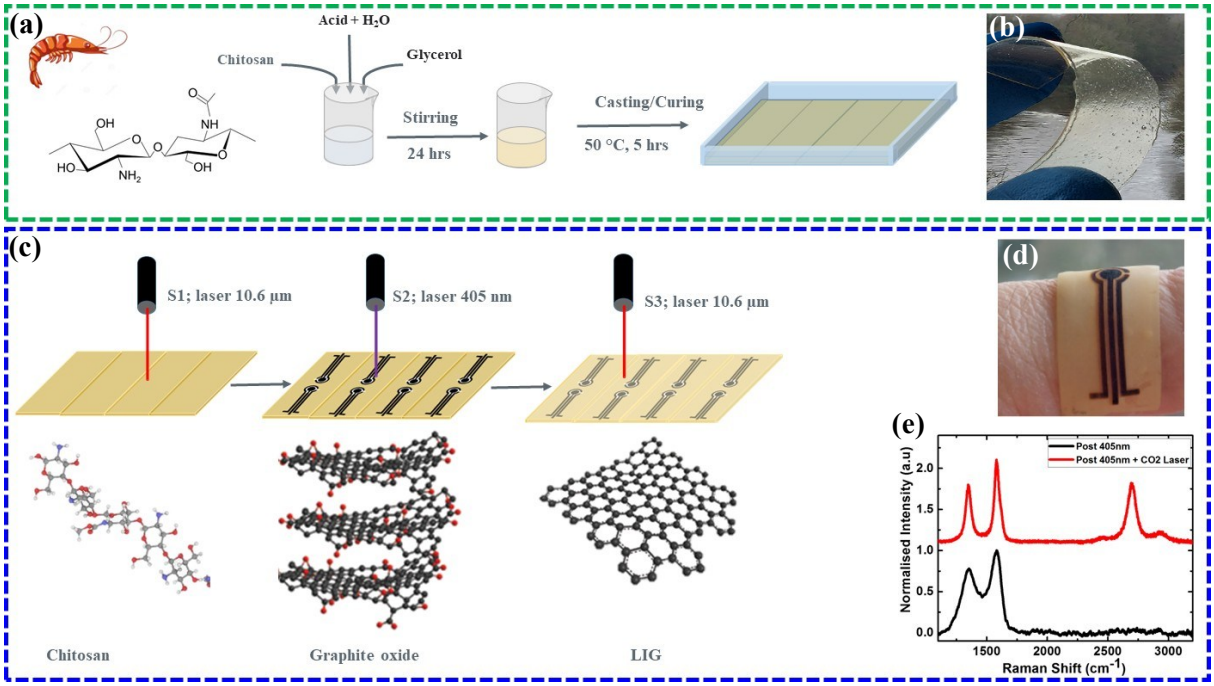

Figure 1.15 Chitosan gLIG biosensor fabrication: a) schematic process of chitosan biofilm synthesis, b) Image of biofilm, c) 3-steps DLW process on biofilm. d) Image of a 3-electrode design written on biofilm e) Raman spectra of LIG at different steps. Reproduced from [98], Copyright 2023, Elsevier.

Recently, biopolymers such as chitosan have emerged as alternative to ligno-cellulosic precursors for the fabrication of gLIG. These materials are important as they offer an alternative to address the lack of transparency and limited mechanical stability/flexibility of ligno-cellulosic materials. Recently, DLW methodologies have been implemented to successfully graphitise chitosan, opening the way to the use of biopolymers for gLIG production. Specifically, three-steps DLW processes were used to ensure the formation of gLIG, as reported by Larrigy et al. (figure 1.15).[99] The first step involved raster-patterning a rectangular area on the chitosan substrate using a 10.6 µm CO_2 laser, which proved to be essential. Chitosan films contain interstitial networks of water molecules that are transiently linked via hydrogen bonds to the polysaccharide backbone. While these interactions impart flexibility and stretchability to the biopolymer film, they also inhibit graphitization in a single-step process. Therefore, the initial laser treatment was necessary to locally desorb water and reduce hydrogen-bonded interactions between the chitosan side groups and interstitial water molecules, thereby

facilitating the subsequent graphitization process. The second step used a 450 nm laser, which further diminished the water content in the film and caused a significant, despite incomplete carbonisation. During this step, electrode patterns were written on the chitosan film and showed a 3D micro/nanoporous morphology with amorphous characteristics. The third step was a repetition of step 1 using again the 10.6 µm CO_2 laser, causing significantly higher levels of graphitization and increased nano-structuring of the hierarchical porous surface.[99]

1.7 gLIG applications

The interest of the scientific community towards gLIG has increased in the past few years, with several publications focusing on the integration of gLIG in applications such as electronic circuit,[100] electrocatalysts,[101] supercapacitors,[82] strain sensors,[93] and solar steam generation[102] as shown in figure 1.16

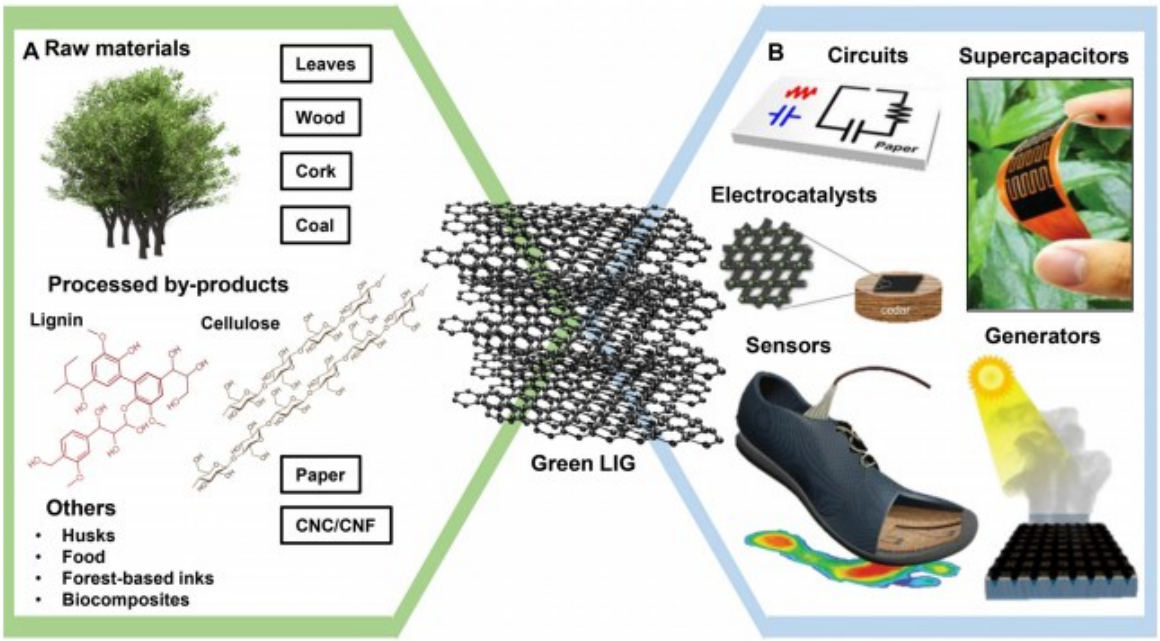

Figure 1.16 Scheme of gLIG production: a) bio-sources, b) applications. Reproduced from [79]. Copyright 2022, AIP Publishing.

Energy storage is among the most promising application of gLIG. Supercapacitors are devices capable to store electrical energy in the electrical double layer that forms between electrolyte solution and electronic conductor (electrodes) and have attracted interest for their applications

as memory protection in electronic circuitry, and their potential as energy storage in portable electronic devices.[89]

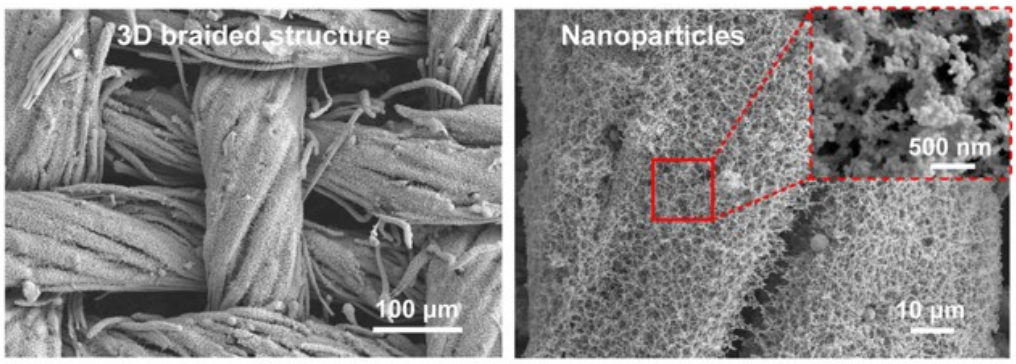

Figure 1.17 SEM characterisation of gLIG formation on cotton (left) LIG/MnOx and (right) magnified image showing the uniform coating with MnOx nanoparticles. Readapted from [103]. Copyright 2022, Elsevier.

Longsheng et al. investigated the fabrication of supercapacitors using gLIG obtained from DLW of cotton cloth.[103] Initially, the cotton was pre-carbonised by subjecting it to temperatures 300 ℃ for 2 h, causing the conversion of cellulose into amorphous carbon, and then coated with a Mn ion hydrogel ink. The cloth was then irradiated with CO_2 laser, producing a gLIG doped with MnOx nanoparticles (figure 1.17). The authors suggest that the Mn-coated cotton cloth absorbed and accumulated heat during the lasing process, causing the oxidation of Mn ions and promoting the formation of MnOx nanoparticles, which adhered uniformly on the surface of the amorphous carbon. Their interaction with the incident laser radiation generated a photothermal effect, responsible of the graphitization and formation of gLIG. The supercapacitors electrodes obtained from this procedure showed promising areal capacitance of 54.97 mF/cm^2, and areal energy density of 7.63 µWh/cm^2.

Figure 1.18 Fallen leaves gLIG electrodes used to power: a) LED, b) table clock; c) gLIG electrode on fallen leave showing good flexibility. Readapted from [82], Copyright 2021, John Wiley and Sons.

The fabrication of supercapacitors from natural raw materials was investigated, as mentioned before by using fallen leaves as carbon-source for DLW processes. In their pioneering work, Le et al. demonstrated that it is possible to write electrode patterns directly onto fallen leaves.[82] *Nageia fleuryi* leaves were chosen for their thickness (~330 µm), high lignin content (~39.3%), and excellent mechanical flexibility, making them suitable for laser-induced graphene (LIG) fabrication. The leaves were first collected and cleaned using ethanol-wetted tissues to remove surface debris and contaminants. They were then flattened between two metal plates and dried in an oven at 100°C for 2 hours to remove residual moisture and enhance their stability.

For the direct laser writing (DLW) process, a femtosecond laser was employed with parameters of 346 nm wavelength, 255 fs pulse duration, and a repetition rate of 201.5 kHz, operating in raster mode. This approach resulted in the formation of graphene-like laser-induced graphene (gLIG) electrodes with a low sheet resistance of 23.3 Ω sq^{-1}. The electrodes exhibited excellent capacitive performance, with an areal capacitance of 34.68 mF/cm^2 at 5 mV/s and remarkable capacitance retention (~99%) after 50,000 charge/discharge cycles. To demonstrate the feasibility of these electrodes in green electronics, the fabricated fallen-leaf electrodes were successfully used to power LEDs and table clocks, showcasing their potential for sustainable energy storage applications (figure 1.18).[82]

Laser-Induced Graphene (LIG) has emerged as a highly versatile material, capable of being tailored for a wide range of applications. Its properties such as porosity, conductivity, and surface chemistry can be finely tuned by adjusting laser parameters, doping materials and the choice of precursor substrate. This adaptability makes LIG suitable for applications spanning sensors, energy storage, harvesting as well as flexible electronics. The field continues to grow rapidly, driven by innovations in laser technologies, the development of novel and eco-friendly precursor materials, and the increasing demand for sustainable, high-performance materials in next-generation devices.

This thesis focuses on developing low-cost, sustainable electrochemical devices for sensing, energy storage, and harvesting. Using a low-power laser system, Laser-Induced Graphene (LIG) was fabricated from synthetic polyimide, cork, and chitosan-based bio-composite substrates. These materials were characterized and evaluated for their electrochemical performance.

Chapter 2 details the fabrication of Ag nanoparticle-functionalized LIG electrodes on polyimide for Electrochemical Surface-Enhanced Raman Spectroscopy (EC-SERS). These sensors enabled rapid, sensitive detection of analytes like 4-ABT, melamine, and difloxacin without pre-treatment, highlighting their potential in food and environmental monitoring.

Chapter 3 explores cork-derived LIG for supercapacitors. The material showed high surface area, good conductivity, and mechanical flexibility, making it suitable for eco-friendly, wearable energy storage devices.

Chapter 4 presents supercapacitors and triboelectric nanogenerators (TENGs) made from LIG on chitosan-lignin-boric acid composite films via a one-step process. The devices demonstrated good capacitance, stability, and energy output, showcasing the promise of biodegradable materials for green energy applications.

1.8 References

[1] K. S. Novoselov et al, “Electric Field Effect in Atomically Thin Carbon Films,” vol. 306, no. 5696, pp. 666–669, 2016.

[2] A. K. Geim and K. S. Novoselov, “The rise of graphene PROGRESS,” *Nat. Mater.*, vol. 6, no. 3, pp. 183–191, 2007.

[3] M. D. Stoller, S. Park, Y. Zhu, J. An, and R. S. Ruoff, “Graphene-Based Ultracapacitors,” pp. 6–10, 2008.

[4] I. W. Frank, D. M. Tanenbaum, A. M. van der Zande, and P. L. McEuen, “Mechanical properties of suspended graphene sheets,” *J. Vac. Sci. Technol. B Microelectron. Nanom. Struct. Process. Meas. Phenom.*, vol. 25, no. 6, pp. 2558–2561, 2007, doi: 10.1116/1.2789446.

[5] A. E. Galashev and O. R. Rakhmanova, “Mechanical and thermal stability of graphene and graphene-based materials,” *Physics-Uspekhi*, vol. 57, no. 10, pp. 970–989, 2014, doi: 10.3367/ufne.0184.201410c.1045.

[6] R. Ye *et al.*, “In Situ Formation of Metal Oxide Nanocrystals Embedded in Laser-Induced Graphene,” *ACS Nano*, vol. 9, no. 9, pp. 9244–9251, 2015, doi: 10.1021/acsnano.5b04138.

[7] A. Nag, A. Mitra, and S. C. Mukhopadhyay, “Graphene and its sensor-based applications: A review,” *Sensors Actuators, A Phys.*, vol. 270, pp. 177–194, 2018, doi: 10.1016/j.sna.2017.12.028.

[8] S. H. Bae, Y. Lee, B. K. Sharma, H. J. Lee, J. H. Kim, and J. H. Ahn, “Graphene-based transparent strain sensor,” *Carbon N. Y.*, vol. 51, no. 1, pp. 236–242, 2013, doi: 10.1016/j.carbon.2012.08.048.

[9] K. Pal *et al.*, “Cutting edge development on graphene derivatives modified by liquid crystal and CdS/TiO2 hybrid matrix: optoelectronics and biotechnological aspects,” *Crit. Rev. Solid State Mater. Sci.*, vol. 46, no. 5, pp. 385–449, Sep. 2021, doi: 10.1080/10408436.2020.1805295.

[10] Z. Niu, L. Liu, L. Zhang, and X. Chen, “Porous graphene materials for water remediation.,” *Small*, vol. 10, no. 17, pp. 3434–3441, Sep. 2014, doi: 10.1002/smll.201400128.

[11] J. Zhu, D. Yang, Z. Yin, Q. Yan, and H. Zhang, “Graphene and graphene-based materials for energy storage applications,” *Small*, vol. 10, no. 17, pp. 3480–3498, 2014, doi: 10.1002/smll.201303202.

[12] A. G. Olabi, M. A. Abdelkareem, T. Wilberforce, and E. T. Sayed, “Application of graphene in energy storage device – A review,” *Renew. Sustain. Energy Rev.*, vol. 135, no. June 2020, p. 110026, 2021, doi: 10.1016/j.rser.2020.110026.

[13] Y. Xu, H. Cao, Y. Xue, B. Li, and W. Cai, “Liquid-phase exfoliation of graphene: An overview on exfoliation media, techniques, and challenges,” *Nanomaterials*, vol. 8, no. 11, 2018, doi: 10.3390/nano8110942.

[14] Y. Bleu *et al.*, “Review of graphene growth from a solid carbon source by pulsed laser deposition (PLD),” *Front. Chem.*, vol. 6, no. NOV, 2018, doi: 10.3389/fchem.2018.00572.

[15] Y. I. Zhang, L. Zhang, and C. Zhou, “Graphene and Related Applications,” *Acc. Chem. Res.*, vol. 46, pp. 2329–2339, 2013.

[16] L. Lin, B. Deng, J. Sun, H. Peng, and Z. Liu, “Bridging the Gap between Reality and Ideal in Chemical Vapor Deposition Growth of Graphene,” *Chem. Rev.*, vol. 118, no. 18, pp. 9281–9343, 2018, doi: 10.1021/acs.chemrev.8b00325.

[17] M. A. Islam *et al.*, “Exfoliation mechanisms of 2D materials and their applications,” *Appl. Phys. Rev.*, vol. 9, no. 4, p. 41301, Oct. 2022, doi: 10.1063/5.0090717.

[18] S. H. Choi *et al.*, “Large-scale synthesis of graphene and other 2D materials towards industrialization,” *Nat. Commun.*, vol. 13, no. 1, pp. 1–5, 2022, doi: 10.1038/s41467-022-29182-y.

[19] Z. Sun, S. Fang, and Y. H. Hu, “3D Graphene Materials: From Understanding to Design and Synthesis Control,” *Chem. Rev.*, vol. 120, no. 18, pp. 10336–10453, 2020, doi: 10.1021/acs.chemrev.0c00083.

[20] C. Li and G. Shi, “Three-dimensional graphene architectures,” *Nanoscale*, vol. 4, no. 18, pp. 5549–5563, 2012, doi: 10.1039/c2nr31467c.

[21] J. Wang, Z. Shi, J. Fan, Y. Ge, J. Yin, and G. Hu, “Self-assembly of graphene into three-dimensional structures promoted by natural phenolic acids,” *J. Mater. Chem.*, vol. 22, no. 42, pp. 22459–22466, 2012, doi: 10.1039/c2jm35024f.

[22] H. Hu, Z. Zhao, W. Wan, Y. Gogotsi, and J. Qiu, “Ultralight and highly compressible graphene aerogels,” *Adv. Mater.*, vol. 25, no. 15, pp. 2219–2223, 2013, doi: 10.1002/adma.201204530.

[23] T. Wu *et al.*, “Three-dimensional graphene-based aerogels prepared by a self-assembly process and its excellent catalytic and absorbing performance,” *J. Mater. Chem. A*, vol. 1, no. 26, pp. 7612–7621, 2013, doi: 10.1039/c3ta10989e.

[24] W. Zeng *et al.*, “Defect-engineered reduced graphene oxide sheets with high electric conductivity and controlled thermal conductivity for soft and flexible wearable thermoelectric generators,” *Nano Energy*, vol. 54, no. October, pp. 163–174, 2018, doi: 10.1016/j.nanoen.2018.10.015.

[25] V. Abdelsayed, S. Moussa, H. M. Hassan, H. S. Aluri, M. M. Collinson, and M. S. El-Shall, “Photothermal deoxygenation of graphite oxide with laser excitation in solution and graphene-aided increase in water temperature,” *J. Phys. Chem. Lett.*, vol. 1, no. 19, pp. 2804–2809, 2010, doi: 10.1021/jz1011143.

[26] S. Gilje, S. Dubin, A. Badakhshan, J. Farrar, S. A. Danczyk, and R. B. Kaner, “Photothermal deoxygenation of graphene oxide for patterning and distributed ignition applications,” *Adv. Mater.*, vol. 22, no. 3, pp. 419–423, 2010, doi: 10.1002/adma.200901902.

[27] C. Zhu *et al.*, “Highly compressible 3D periodic graphene aerogel microlattices,” *Nat. Commun.*, vol. 6, pp. 1–8, 2015, doi: 10.1038/ncomms7962.

[28] Y. Ito, H. J. Qiu, T. Fujita, Y. Tanabe, K. Tanigaki, and M. Chen, “Bicontinuous nanoporous N-doped graphene for the oxygen reduction reaction,” *Adv. Mater.*, vol. 26, no. 24, pp. 4145–4150, 2014, doi: 10.1002/adma.201400570.

[29] Y. Ito *et al.*, “High-quality three-dimensional nanoporous graphene,” *Angew. Chemie - Int. Ed.*, vol. 53, no. 19, pp. 4822–4826, 2014, doi: 10.1002/anie.201402662.

[30] E. Umar, M. Ikram, J. Haider, W. Nabgan, M. Imran, and G. Nazir, “3D graphene-based material: Overview, perspective, advancement, energy storage, biomedical engineering and environmental applications a bibliometric analysis,” *J. Environ. Chem. Eng.*, vol. 11, no. 5, 2023, doi: 10.1016/j.jece.2023.110339.

[31] J. Lin *et al.*, “Laser-induced porous graphene films from commercial polymers,” *Nat. Commun.*, vol. 5, pp. 5–12, 2014, doi: 10.1038/ncomms6714.

[32] R. Ye, D. K. James, and J. M. Tour, “Laser-Induced Graphene,” *Acc. Chem. Res.*, vol. 51, no. 7, pp. 1609–1620, 2018, doi: 10.1021/acs.accounts.8b00084.

[33] A. Imbrogno *et al.*, “Laser-Induced Graphene Supercapacitors by Direct Laser Writing of Cork Natural Substrates,” *ACS Appl. Electron. Mater.*, vol. 4, no. 4, pp. 1541–1551, Apr. 2022, doi: 10.1021/acsaelm.1c01202.

[34] H. Yu, M. Gai, L. Liu, F. Chen, J. Bian, and Y. Huang, “Laser-induced direct graphene patterning: from formation mechanism to flexible applications,” *Soft Sci.*, vol. 3, no. 1, 2023, doi: 10.20517/ss.2022.26.

[35] S. Chatani, C. J. Kloxin, and C. N. Bowman, “The power of light in polymer science: Photochemical processes to manipulate polymer formation, structure, and properties,” *Polym. Chem.*, vol. 5, no. 7, pp. 2187–2201, 2014, doi: 10.1039/c3py01334k.

[36] R. Murray, M. Burke, D. Iacopino, and A. J. Quinn, “Design of Experiments and Optimization of Laser-Induced Graphene,” *ACS Omega*, vol. 6, no. 26, pp. 16736–16743, 2021, doi: 10.1021/acsomega.1c00309.

[37] T. S. D. Le *et al.*, “Recent Advances in Laser-Induced Graphene: Mechanism, Fabrication, Properties, and Applications in Flexible Electronics,” *Adv. Funct. Mater.*, vol. 32, no. 48, pp. 1–39, 2022, doi: 10.1002/adfm.202205158.

[38] M. Burke *et al.*, “Fabrication and Electrochemical Properties of Three-Dimensional (3D) Porous Graphitic and Graphenelike Electrodes Obtained by Low-Cost Direct Laser Writing Methods,” *ACS Omega*, vol. 5, no. 3, pp. 1540–1548, 2020, doi: 10.1021/acsomega.9b03418.

[39] A. Vashisth, M. Kowalik, J. C. Gerringer, C. Ashraf, A. C. T. Van Duin, and M. J. Green, “ReaxFF Simulations of Laser-Induced Graphene (LIG) Formation for Multifunctional Polymer Nanocomposites,” *ACS Appl. Nano Mater.*, vol. 3, no. 2, pp. 1881–1890, 2020, doi: 10.1021/acsanm.9b02524.

[40] Z. Peng, J. Lin, R. Ye, E. L. G. Samuel, and J. M. Tour, “Flexible and stackable laser-induced graphene supercapacitors,” *ACS Appl. Mater. Interfaces*, vol. 7, no. 5, pp. 3414–3419, Feb. 2015, doi: 10.1021/am509065d.

[41] A. Dallinger, K. Keller, H. Fitzek, and F. Greco, “Stretchable and Skin-Conformable Conductors Based on Polyurethane/Laser-Induced Graphene,” *ACS Appl. Mater. Interfaces*, vol. 12, no. 17, pp. 19855–19865, 2020, doi: 10.1021/acsami.0c03148.

[42] D. Vacher, S. Menecier, M. Dudeck, M. Dubois, B. Devouard, and E. Petit, "Solid carbon produced in an inductively coupled plasma torch with a Titan like atmosphere," *Int. J. Aerosp. Eng.*, vol. 2013, 2013, doi: 10.1155/2013/546385.

[43] F. A. Stevie and C. L. Donley, "Introduction to x-ray photoelectron spectroscopy," *J. Vac. Sci. Technol. A Vacuum, Surfaces, Film.*, vol. 38, no. 6, 2020, doi: 10.1116/6.0000412.

[44] E. Jabari and E. Toyserkani, "Laser heat treatment of aerosol-jet additive manufactured graphene patterns," *J. Phys. D. Appl. Phys.*, vol. 48, no. 37, 2015, doi: 10.1088/0022-3727/48/37/375503.

[45] M. Smith, L. Scudiero, J. Espinal, J. S. McEwen, and M. Garcia-Perez, "Improving the deconvolution and interpretation of XPS spectra from chars by ab initio calculations," *Carbon N. Y.*, vol. 110, pp. 155–171, 2016, doi: 10.1016/j.carbon.2016.09.012.

[46] S. Yumitori, "Correlation of C1s chemical state intensities with the O1s intensity in the XPS analysis of anodically oxidized glass-like carbon samples," *J. Mater. Sci.*, vol. 35, no. 1, pp. 139–146, 2000, doi: 10.1023/A:1004761103919.

[47] A. V. Shchukarev and D. V. Korolkov, "XPS study of group IA carbonates," *Cent. Eur. J. Chem.*, vol. 2, no. 2, pp. 347–362, 2004, doi: 10.2478/BF02475578.

[48] T. Takahagi and A. Ishitani, "XPS studies by use of the digital difference spectrum technique of functional groups on the surface of carbon fiber," *Carbon N. Y.*, vol. 22, no. 1, pp. 43–46, 1984, doi: https://doi.org/10.1016/0008-6223(84)90131-3.

[49] B. Lesiak *et al.*, "C sp 2 /sp 3 hybridisations in carbon nanomaterials – XPS and (X)AES study," *Appl. Surf. Sci.*, vol. 452, pp. 223–231, 2018, doi: 10.1016/j.apsusc.2018.04.269.

[50] S. Kaciulis, A. Mezzi, S. K. Balijepalli, M. Lavorgna, and H. S. Xia, "Electron spectroscopy of rubber and resin-based composites containing 2D carbon," *Thin Solid Films*, vol. 581, pp. 80–85, 2015, doi: 10.1016/j.tsf.2014.11.039.

[51] A. C. Ferrari and D. M. Basko, "Raman spectroscopy as a versatile tool for studying the properties of graphene," *Nat. Nanotechnol.*, vol. 8, no. 4, pp. 235–246, 2013, doi: 10.1038/nnano.2013.46.

[52] A. C. Ferrari *et al.*, "Raman spectrum of graphene and graphene layers," *Phys. Rev. Lett.*, vol. 97, no. 18, pp. 1–4, 2006, doi: 10.1103/PhysRevLett.97.187401.

[53] A. Ferrari and J. Robertson, “Interpretation of Raman spectra of disordered and amorphous carbon,” *Phys. Rev. B - Condens. Matter Mater. Phys.*, vol. 61, no. 20, pp. 14095–14107, 2000, doi: 10.1103/PhysRevB.61.14095.

[54] B. J. Venton and D. J. DiScenza, “Chapter 3 - Voltammetry,” B. B. T.-E. for B. Patel, Ed., Elsevier, 2020, pp. 27–50. doi: https://doi.org/10.1016/B978-0-12-821203-5.00004-X.

[55] E. Cesewski and B. N. Johnson, “Electrochemical biosensors for pathogen detection,” *Biosens. Bioelectron.*, vol. 159, no. October 2019, 2020, doi: 10.1016/j.bios.2020.112214.

[56] F. G. Wilhelm, N. F. A. Van der Vegt, M. Wessling, and H. Strathmann, “Chronopotentiometry for the advanced current-voltage characterisation of bipolar membranes,” *J. Electroanal. Chem.*, vol. 502, no. 1–2, pp. 152–166, 2001, doi: 10.1016/S0022-0728(01)00348-5.

[57] A. C. Lazanas and M. I. Prodromidis, “Electrochemical Impedance Spectroscopy─A Tutorial,” *ACS Meas. Sci. Au*, vol. 3, no. 3, pp. 162–193, 2023, doi: 10.1021/acsmeasuresciau.2c00070.

[58] C. G. Bard, Allen J. and Faulkner, Larry R. and White, Henry S. and Zoski, *Electrochemical Methods: Fundamentals and Applications*, 3rd ed. John Wiley & Sons, 2022.

[59] R. S. Nicholson, “Theory and Application of Cyclic Voltammetry for Measurement of Electrode Reaction Kinetics,” *Anal. Chem.*, vol. 37, no. 11, pp. 1351–1355, 1965, doi: 10.1021/ac60230a016.

[60] I. Lavagnini, R. Antiochia, and F. Magno, “An extended method for the practical evaluation of the standard rate constant from cyclic voltammetric data,” *Electroanalysis*, vol. 16, no. 6, pp. 505–506, 2004, doi: 10.1002/elan.200302851.

[61] J. E. B. Randles, “A cathode ray polarograph.The current-voltage curves.,” *Trans. Faraday Soc.*, vol. 44, pp. 327–338, 1948.

[62] A. Ševčík, “Oscillographic polarography with periodical triangular voltage,” *Collect. Czechoslov. Chem. Commun.*, vol. 13, pp. 349–377, 1948, doi: https://doi.org/10.1135/cccc19480349.

[63] K. Dissanayake and D. Kularatna-Abeywardana, “A review of supercapacitors:

Materials, technology, challenges, and renewable energy applications," *J. Energy Storage*, vol. 96, no. February, 2024, doi: 10.1016/j.est.2024.112563.

[64] O. Stern, "ZUR THEORIE DER ELEKTROLYTISCHEN DOPPELSCHICHT," *Zeitschrift für Elektrochemie und Angew. Phys. Chemie*, 1924, [Online]. Available: https://api.semanticscholar.org/CorpusID:138033996

[65] H. von Helmholtz, "Studien über electrische Grenzschichten," *Ann. Phys.*, vol. 243, pp. 337–382, [Online]. Available: https://api.semanticscholar.org/CorpusID:122723596

[66] M. Gouy, "Sur la constitution de la charge électrique à la surface d'un électrolyte," [Online]. Available: https://api.semanticscholar.org/CorpusID:194091054

[67] L. L. Zhang and X. S. Zhao, "Carbon-based materials as supercapacitor electrodes," *Chem. Soc. Rev.*, vol. 38, no. 9, pp. 2520–2531, 2009, doi: 10.1039/B813846J.

[68] P. Simon and Y. Gogotsi, "Materials for electrochemical capacitors," *Nat. Mater.*, vol. 7, no. 11, pp. 845–854, 2008, doi: 10.1038/nmat2297.

[69] Y. Shao *et al.*, "Design and Mechanisms of Asymmetric Supercapacitors," *Chem. Rev.*, vol. 118, no. 18, pp. 9233–9280, Sep. 2018, doi: 10.1021/acs.chemrev.8b00252.

[70] Y. Wang, Y. Song, and Y. Xia, "Electrochemical capacitors: mechanism{,} materials{,} systems{,} characterization and applications," *Chem. Soc. Rev.*, vol. 45, no. 21, pp. 5925–5950, 2016, doi: 10.1039/C5CS00580A.

[71] J. R. Macdonald and W. B. Johnson, "Fundamentals of Impedance Spectroscopy," in *Impedance Spectroscopy*, John Wiley & Sons, Ltd, 2005, pp. 1–26. doi: https://doi.org/10.1002/0471716243.ch1.

[72] C. Lämmel, M. Schneider, M. Weiser, and A. Michaelis, "Investigations of electrochemical double layer capacitor (EDLC) materials - A comparison of test methods," *Materwiss. Werksttech.*, vol. 44, no. 7, pp. 641–649, 2013, doi: 10.1002/mawe.201300122.

[73] P. Nayak, N. Kurra, C. Xia, and H. N. Alshareef, "Highly Efficient Laser Scribed Graphene Electrodes for On-Chip Electrochemical Sensing Applications," *Adv. Electron. Mater.*, vol. 2, no. 10, pp. 1–11, 2016, doi: 10.1002/aelm.201600185.

[74] E. P. Randviir, D. A. C. Brownson, M. Gómez-Mingot, D. K. Kampouris, J. Iniesta, and C. E. Banks, "Electrochemistry of Q-Graphene," *Nanoscale*, vol. 4, no. 20, pp. 6470–

6480, 2012, doi: 10.1039/c2nr31823g.

[75] C. Bosch-Navarro, Z. P. L. Laker, J. P. Rourke, and N. R. Wilson, “Reproducible, stable and fast electrochemical activity from easy to make graphene on copper electrodes,” *Phys. Chem. Chem. Phys.*, vol. 17, no. 44, pp. 29628–29636, 2015, doi: 10.1039/c5cp04070a.

[76] D. A. C. Brownson, S. A. Varey, F. Hussain, S. J. Haigh, and C. E. Banks, “Electrochemical properties of CVD grown pristine graphene: Monolayer- vs. quasi-graphene,” *Nanoscale*, vol. 6, no. 3, pp. 1607–1621, 2014, doi: 10.1039/c3nr05643k.

[77] D. Iacopino *et al.*, “Visible laser scribing fabrication of porous graphitic carbon electrodes: Morphologies, electrochemical properties, and applications as disposable sensor platforms,” *ACS Appl. Electron. Mater.*, vol. 2, no. 10, pp. 3279–3288, 2020, doi: 10.1021/acsaelm.0c00612.

[78] G. Xu, Z. A. Jarjes, V. Desprez, P. A. Kilmartin, and J. Travas-Sejdic, “Sensitive, selective, disposable electrochemical dopamine sensor based on PEDOT-modified laser scribed graphene,” *Biosens. Bioelectron.*, vol. 107, no. November 2017, pp. 184–191, 2018, doi: 10.1016/j.bios.2018.02.031.

[79] P. I. C. Claro *et al.*, “Sustainable carbon sources for green laser-induced graphene: A perspective on fundamental principles, applications, and challenges,” *Appl. Phys. Rev.*, vol. 9, no. 4, Dec. 2022, doi: 10.1063/5.0100785.

[80] Y. Chyan, R. Ye, Y. Li, S. P. Singh, C. J. Arnusch, and J. M. Tour, “Laser-Induced Graphene by Multiple Lasing: Toward Electronics on Cloth, Paper, and Food,” *ACS Nano*, vol. 12, no. 3, pp. 2176–2183, 2018, doi: 10.1021/acsnano.7b08539.

[81] H. R. Moon and B. Ryu, “Review of Laser-Induced Graphene (LIG) Produced on Eco-Friendly Substrates,” *Int. J. Precis. Eng. Manuf. - Green Technol.*, vol. 11, no. 4, pp. 1279–1294, 2024, doi: 10.1007/s40684-024-00595-y.

[82] T. S. D. Le *et al.*, “Green Flexible Graphene–Inorganic-Hybrid Micro-Supercapacitors Made of Fallen Leaves Enabled by Ultrafast Laser Pulses,” *Adv. Funct. Mater.*, vol. 32, no. 20, May 2022, doi: 10.1002/adfm.202107768.

[83] R. Al, I. Reshad, T. A. Jishan, and N. N. Chowdhury, “JOURNAL OF CLINICAL AND EXPERIMENTAL INVESTIGATIONS Chitosan and its Broad Applications : A Brief Review,” vol. 12, no. 4, pp. 1–13, 2021.

[84] F. Croisier and C. Jérôme, “Chitosan-based biomaterials for tissue engineering,” *Eur. Polym. J.*, vol. 49, no. 4, pp. 780–792, 2013, doi: 10.1016/j.eurpolymj.2012.12.009.

[85] S. Sayyar *et al.*, “Processable conducting graphene/chitosan hydrogels for tissue engineering,” *J. Mater. Chem. B*, vol. 3, no. 3, pp. 481–490, 2015, doi: 10.1039/c4tb01636j.

[86] Y. H. Lin *et al.*, “Preparation and evaluation of chitosan biocompatible electronic skin,” *Comput. Ind.*, vol. 100, no. November 2016, pp. 1–6, 2018, doi: 10.1016/j.compind.2018.03.040.

[87] M. Devi and S. Rawat, “A comprehensive review of the pyrolysis process: From carbon nanomaterial synthesis to waste treatment,” *Oxford Open Mater. Sci.*, vol. 1, no. 1, pp. 1–30, 2021, doi: 10.1093/oxfmat/itab014.

[88] R. Ye *et al.*, “Laser-Induced Graphene Formation on Wood,” *Adv. Mater.*, vol. 29, no. 37, pp. 1–7, 2017, doi: 10.1002/adma.201702211.

[89] M. Winter and R. J. Brodd, “What are batteries, fuel cells, and supercapacitors?,” *Chem. Rev.*, vol. 104, no. 10, pp. 4245–4269, 2004, doi: 10.1021/cr020730k.

[90] H. Pereira, “Variability of the chemical composition of cork,” *BioResources*, vol. 8, no. 2, pp. 2246–2256, 2013, doi: 10.15376/biores.8.2.2246-2256.

[91] H.-W. Heldt and B. Piechulla, “Chapter 18 - Phenylpropanoids Comprise a Multitude of Plant-Specialized Metabolites and Cell Wall Components,” H.-W. Heldt and B. B. T.-P. B. (Fifth E. Piechulla, Eds., Academic Press, 2021, pp. 411–429. doi: https://doi.org/10.1016/B978-0-12-818631-2.00018-0.

[92] M. Setti *et al.*, “Sustainable electrochemical sensors from cork-derived laser induced graphene: Non-enzymatic glucose detection in urine,” *Sensors Actuators B Chem.*, vol. 430, no. October 2024, 2025, doi: 10.1016/j.snb.2025.137352.

[93] A. F. Carvalho, A. J. S. Fernandes, R. Martins, E. Fortunato, and F. M. Costa, “Laser-Induced Graphene Piezoresistive Sensors Synthesized Directly on Cork Insoles for Gait Analysis,” *Adv. Mater. Technol.*, vol. 5, no. 12, pp. 1–8, 2020, doi: 10.1002/admt.202000630.

[94] M. Amiri, H., Aghbashlo, M., Sharma, “Chitin and chitosan derived from crustacean waste valorization streams can support food systems and the UN Sustainable Development Goals,” *Nat. food*, vol. 3, pp. 822–828, 2022, doi:

https://doi.org/10.1038/s43016-022-00591-y.

[95] M. N. V. R. Kumar, “A review of chitin and chitosan applications,” *React. Funct. Polym.*, vol. 46, pp. 1–27, 2000, doi: https://doi.org/10.1016/S1381-5148(00)00038-9.

[96] M. Rinaudo, “Chitin and chitosan: Properties and applications,” *Prog. Polym. Sci.*, vol. 31, no. 7, pp. 603–632, 2006, doi: 10.1016/j.progpolymsci.2006.06.001.

[97] M. Dash, F. Chiellini, R. M. Ottenbrite, and E. Chiellini, “Chitosan - A versatile semi-synthetic polymer in biomedical applications,” *Prog. Polym. Sci.*, vol. 36, no. 8, pp. 981–1014, 2011, doi: 10.1016/j.progpolymsci.2011.02.001.

[98] H. Hamidi *et al.*, “Laser induced graphene (LIG) biosensors derived from chitosan: Towards sustainable and green electronics,” *Biosens. Bioelectron. X*, vol. 15, no. June, p. 100403, 2023, doi: 10.1016/j.biosx.2023.100403.

[99] C. Larrigy *et al.*, “Porous 3D Graphene from Sustainable Materials: Laser Graphitization of Chitosan,” *Adv. Mater. Technol.*, vol. 8, no. 4, 2023, doi: 10.1002/admt.202201228.

[100] H. Park, M. Kim, B. G. Kim, and Y. H. Kim, “Electronic Functionality Encoded Laser-Induced Graphene for Paper Electronics,” *ACS Appl. Nano Mater.*, vol. 3, no. 7, pp. 6899–6904, 2020, doi: 10.1021/acsanm.0c01255.

[101] X. Han *et al.*, “Laser-Induced Graphene from Wood Impregnated with Metal Salts and Use in Electrocatalysis,” *ACS Appl. Nano Mater.*, vol. 1, no. 9, pp. 5053–5061, 2018, doi: 10.1021/acsanm.8b01163.

[102] H. Jang, J. Choi, H. Lee, and S. Jeon, “Corrugated Wood Fabricated Using Laser-Induced Graphitization for Salt-Resistant Solar Steam Generation,” *ACS Appl. Mater. Interfaces*, vol. 12, no. 27, pp. 30320–30327, 2020, doi: 10.1021/acsami.0c05138.

[103] L. Lu, D. Zhang, Y. Xie, and W. Wang, “A stretchable, high-voltage and biobased microsupercapacitor using laser induced graphene/MnOx electrodes on cotton cloth,” *J. Energy Storage*, vol. 51, no. January, 2022, doi: 10.1016/j.est.2022.104458.

Chapter 2: Silver nanoparticles – laser induced graphene (Ag NPs – LIG) hybrid electrodes for sensitive electrochemical-surface enhanced Raman spectroscopy (EC-SERS) detection

2.1 Abstract

This paper presents a novel approach for the fabrication of low cost Electrochemical-Surface Enhanced Raman Scattering (EC-SERS) sensing platforms. Laser Induced Graphene (LIG) electrodes were readily fabricated by direct laser writing of polyimide tapes and functionalized with silver nanoparticles (Ag NPs) to obtain hybrid Ag NPs – LIG electrodes suitable for EC-SERS analysis. Detection was achieved by coup- ling a handheld potentiostat with a Raman spectrograph, enabling measurement of SERS spectra of target analytes generated during voltage sweeps in the 0.0 to −1.0 V interval range. The sensing capabilities of the fabricated system were first tested with model molecule 4-aminobenzenethiol (4-ABT). Following sensitive detection of 4-ABT, EC-SERS analysis of food contaminant melamine in milk and antibiotic difloxacin hydrochloride (DIF) in river water was demonstrated, achieving sensitive detection of both analytes without pre-treatment steps. The easiness of fabrication, versatility of design, rapid analysis time and potential miniaturization of the system make Ag NPs – LIG electrodes suitable for a large range of in situ applications in the field of food monitoring and for environmental analysis.

2.2 Introduction

In the last three decades, Surface Enhanced Raman Scattering (SERS) has been employed for the detection of a wide range of analytes for a plethora of applications, including environmental and health/wellbeing monitoring,[1,2] agri-food,[3] chemical and warfare detection,[4] food safety,[5] forensic analysis,[6] art conservation[7] and general point-of-care analysis.[8] The versatility of SERS is due to its sensitive fingerprinting detection, based on the enhancement of Raman signals (up to a factor of 108–1012), generated by the close proximity of an analyte to plasmonic nanoparticles. This phenomenon has been investigated in depth and it has now been mainly attributed to the formation of large localized surface plasmons resulting in enhanced electromagnetic fields.[9] Along with this electromagnetic (EM) enhancement, chemical enhancement processes (CE) also come into play, leading to the large observed enhancement factors.[10] The combination of high sensitivity, fingerprinting capabilities and recent technological advances in instrumental miniaturization, gives SERS opportunities for fast analysis time, non-destructive and in situ analysis, with minimum pre-treatment steps.[11,12] In parallel, electrochemical analysis is also an attractive and versatile technique suitable for fast, low cost and in situ detection of a wide range of analytes.[13,14] Recently, direct laser writing methods have been used to fabricate Laser Induced Graphene (LIG) electrodes for electrochemical sensing and biosensing.[15–20] As well as versatility of design and low cost, LIG electrode materials displayed enhanced sensitivity com- pared to other carbon-based materials and screen printed electrodes, associated to their high surface area and high defect density.[21,22] Furthermore, SERS platforms obtained by the combination of graphene-like materials and plasmonic nano-particles have been shown to improve Raman enhancement effects through mechanical stability and reproducibility factors, leading to low concentration molecular detections.[23–25] In this context, the combination of electrochemical and SERS techniques (EC-SERS) in a single platform is very attractive to widen the range of the capabilities of the

individual techniques and to increase selectivity and sensitivity of ana- lysis. In EC-SERS measurements the SERS spectra of selected analytes adsorbed on SERS-active electrodes are recorded while controlling the electrode polarization in an electro- chemical cell.[26] The changes occurring at the metal surface during the sweeping process can enhance the analyte's SERS response by promoting increased chemical enhancement contribution through electrode voltage induced variation of the metal's Fermi level or through analyte re-orientation induced by potential changes.[27] Moreover, enhanced electrostatic inter- actions or desorption of interfering matrix species at negative potentials can also occur, leading to control of adsorption and redox states of the analytes and leading to improved performance compared to SERS analysis alone. Recently, EC-SERS has been successfully applied to the detection of herbicides,[28] chemotherapy drugs,[29] melamine,[30] cannabinoids[31] and seized drugs.[32] Low cost and disposable commercial screen printed electrodes (SPEs) modified with Ag nanoparticles (Ag NPs) were used in combination with portable electrochemical and spectroscopic instrumentation, thus making the analysis amenable to point-of-need analysis. The same approach was also used by Eisnor et al. in the field of cultural heritage diagnostics for the identification of polyphenolic components in natural lake pigments.[33] In a recent development, monitoring of biomarkers was achieved with EC-SERS fabric-based plasmonic sensors, suggesting that such platforms could become suitable also for patient point-of-care applications.[34]

In this work, novel LIG electrodes of different morphologies were readily fabricated by direct laser writing of polyimide tapes using low-cost hobbyist lasers. A concentrated solution of Ag NPs was dropped on the LIG surfaces to obtain hybrid Ag NPs–LIG electrodes suitable for EC-SERS analysis. The hybrid electrodes showed sensitive SERS responses for model molecule 4-ABT and target analytes melamine and difloxacin hydrochloride in milk and river water, respectively. EC-SERS measurements of target analytes in relevant matrices allowed sensitive

detection without any need of pre-treatment steps. Taking in consideration the low cost of production, the versatility in electrode design geometry and the inherent flexibility of the developed sensing platforms, these electrodes could be implemented for many point-of-care and point-of need applications across multiple sectors from health to food and environmental monitoring.

2.3 Experimental section

2.3.1 Materials

Polyimide tape with thickness of 80 μm was purchased from Radionics and used without further treatment. Silver nitrate ($AgNO_3$, ≥99.0%), sodium citrate ($C_6H_5Na_3O_7{\cdot}2H_2O$, ≥99.0%), 4-aminobenzenethiol (C_6H_7NS ≥97.0%), melamine ($C_3H_6N_6$, 99%), difloxacin hydrochloride ($C_{21}H_{19}F_2N_3O{\cdot}3HCl$, ≥98.0%), acetonitrile (C_2H_3N, ≥99.9%), acetone, isopropanol, ethanol, sodium fluoride (NaF, 99%), phosphate buffered saline (PBS, pH 7.4) were purchased from Sigma Aldrich and used without further purification. All solutions were prepared using de-ionized (DI) Milli-Q water (resistivity 18.2 MΩ cm).

2.3.2 Electrode Fabrication

LIG electrodes were fabricated using three different lasers: a Colemeter DK-8 Pro-5 Square Haste Edition equipped with a diode laser at 405 nm and 500 mW laser power, a KKmoon Compact Automatic Desktop Laser Engraving Machine equipped with a 3 W power laser with illumination wavelength of 450 nm; a 10.6 μm universal Laser System 4.75, 30 W maximum average power. Electrode structures were designed in Microsoft PowerPoint and transferred to the laser engraving software. Laser writing occurred by raster scanning of the laser beam on the polyimide substrates. The following conditions were used to write LIG structures: 405 nm laser, power 500 mW, dwelling time 40 ms; 450 nm laser, power 30% (0.9 W), contrast ratio

160%, depth of engraving 30%; 10.6 μm laser, power 12.5% (3.75 W), scan speed 12%. Conductive silver paint (Radionics) was used to electrically contact the electrodes to the potentiostat.

2.3.3 Ag NPs synthesis

Ag NPs were synthesized following the classic Lee–Meisel method.[35] Specifically, 45 mg $AgNO_3$ was dissolved in 250 mL of H_2O and added to a 1 L of H_2O in a conical flask equipped with a reflux condenser. The mixture was brought to boiling by a heating mantle for 1 hour. Next, 5 mL of 1% citrate solution was added to the reaction solution. The solution was kept boiling under vigorous mechanical stirring for 1 hour and was then slowly cooled to room temperature. Next, 1000 μL of the prepared Ag NP solution was centrifuged for 10 min at 10,000 rpm, the supernatant was removed and the solid residue re-dispersed into 25 μL of DI water.

2.3.4 Hybrid Ag NPs – LIG electrode fabrication

LIG electrodes were modified by dropping 50–120 μL of concentrated Ag NP solution on the LIG working electrodes. The hybrid electrodes were left to dry in air and washed with DI water prior use to remove unbound NPs.

2.3.5 Characterization

Morphological characterization was performed by a cold- cathode field-emission Scanning Electron Microscope (SEM, FEI Quanta 650) operating at 30 kV acceleration voltage. Surface wettability was measured by a Data physics OCA 20 Wetting angle system in air at ambient temperature by drop- ping distilled water droplets (1 mm diameter) on the surfaces. The average contact angle value was acquired by measuring at six different positions per sample. Raman investigation was performed with Horiba-XPlora Plus equipped with 532 nm (70 mW power) and 785 nm (60 mW power) lasers. Spectra were acquired at a laser power of 1% and 10 s

acquisition time. Cyclic voltammetry (CV) electrochemical measurements were performed with a CHI760 bipotentiostat.

2.3.6 EC-SERS measurements

EC-SERS analysis was carried out by combining the SERS readout from the benchtop Raman spectrograph with the EC readout from a handheld mini potentiostat (Palmsens-Sensit Smart) connected either to an android tablet or to a cell phone for data acquisition and display. In order to perform EC-SERS measurements, a teflon custom made cell was designed and fabricated by 3D printing. Before EC-SERS measurements analyte solutions were dropped on the work electrodes and left to dry. Then, chronoamperometric (CA) electrochemical measurements were performed by systematically decreasing the potential between 0 V and −1.0 V vs. Ag/ AgCl paste in 100 mV steps. Simultaneously, SERS spectra were recorded at each potential step with 785 nm laser illumination and power between 0.25% and 25%.

2.4 Results and Discussion

Scheme 3.1 shows a diagram of the EC-SERS electrode fabrication and the instrumental setup used to record spectra. Photographs of electrodes and instrumentation setup are also included. First LIG electrodes were fabricated by direct laser writing of polyimide with a range of hobbyist lasers with illumination wavelengths 10.6 μm, 450 nm and 405 nm (Scheme 2.1a). A three-electrode system was designed whereby LIG was used as working electrode (WE) and counter electrode (CE) and an Ag/AgCl paste modified LIG was used as reference electrode (RE). The surface of the LIG working electrodes were then modified with Ag NPs (Scheme 2.1b). Following deposition of the analyte, the hybrid Ag NPs – LIG electrode was incorporated in a custom-built electrochemical cell in presence of an electrolyte (Scheme 2.1c). EC-SERS spectra were recorded with a bench top Raman system (785 nm excitation wavelength) coupled with a handheld potentiostat (Scheme 2.1d).

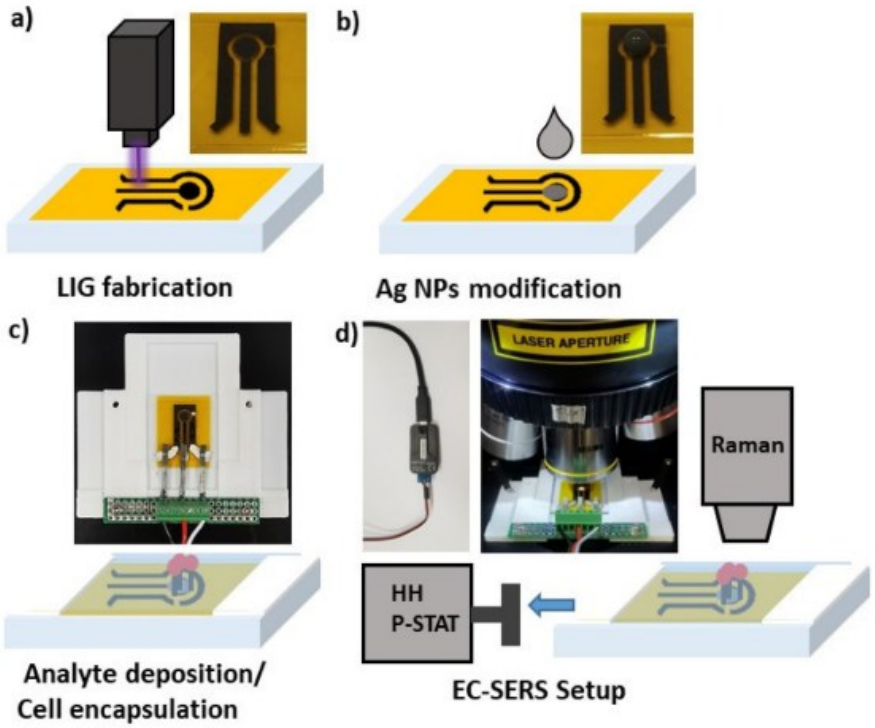

Scheme 2.1 Schematic illustration and photographs of (a) LIG three electrode system fabricated by direct laser writing of polyimide; (b) modification of LIG WE surface with Ag NPs; (c) deposition of analyte and custom-made cell encapsulation; (d) EC-SERS measurement setup.

Figure 2.1 shows SEM images of LIG structures obtained by direct laser writing of polyimide using lasers of different wave- lengths. LIG structures obtained with 405 nm laser (figure 2.1a) showed smooth surface with some particulate likely arising from the laser burning process. The dwell time of the 405 nm laser was kept low on purpose, in order to maintain the surface topography of the resulting LIG material smooth and flat, with the intention to promote homogeneous distribution of Ag NPs on the LIG electrode surface. Figure 2.1b shows a representative SEM image of a LIG structure obtained by writing with 450 nm laser. In contrast with the smooth surface previously obtained at 405 nm, the features obtained at 450 nm displayed the typical 3D, highly porous and rich in defect/edge planes LIG structure, characterised by "exploded" features associated with outgassing generated by laser-assisted local high temperature, high pressure process.[36] A similar morphology was observed in the LIG structures obtained by 10.6 μm laser writing (figure 2.1c), which displayed a high density

of defects and high surface area, in agreement with the morphology already reported for other CO_2 laser written features on polyimide.[37]

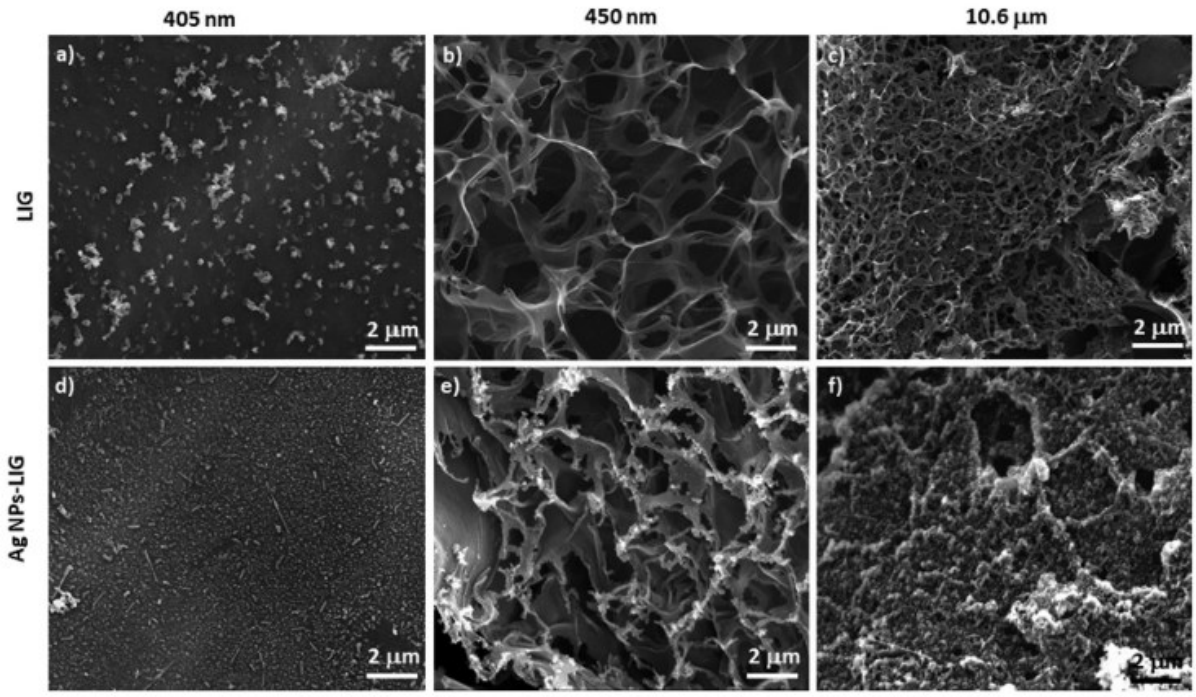

Figure 2.1 SEM images of LIG structures obtained by laser irradiation of polyimide at (a) 405 nm; (b) 450 nm; (c) 10.6 µm. SEM images of (d) 405 nm LIG; (e) 450 nm LIG; (f) 10.6 µm LIG structures after Ag NPs deposition.

Figure 2.1d–f show SEM images of LIG structures written with the three lasers following Ag NP deposition. For this electrode modification, a drop of concentrated Ag NP solution (average particle size ~50 nm) was deposited on the LIG surface and left to evaporate at room temperature. The hybrid structure of Ag NPs modified LIG written with 405 nm laser displayed accumulation of NPs in the grooves formed by the laser writing process, whereas the top LIG surface remained largely unmodified (figure 2.1d). In contrast, for LIG structures fabricated with 450 nm laser, Ag NPs preferentially attached to the top of the edge planes, whereas most of the plane walls remained virtually unmodified (figure 2.1e). The Ag NPs – LIG 10.6 µm structure showed the most uniform nano-particle coverage, as evident from the SEM image showing uniform coverage of the LIG planes (figure 2.1f).

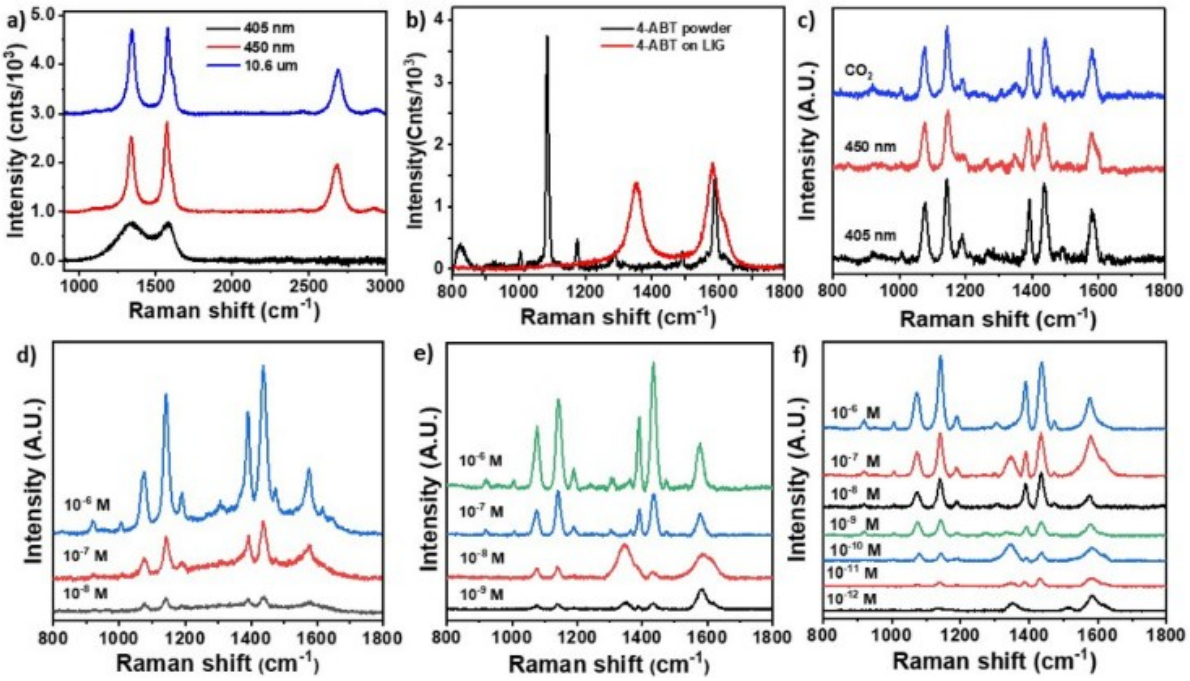

Figure 2.2 (a) Raman spectra of LIG structures obtained with different lasers; (b) Raman spectra of 4-ABT powder and 4-ABT deposited on 450 nm LIG in absence of Ag NPs; (c) SERS spectra of 4-ABT obtained on Ag NPs – LIG substrates. SERS spectra of decreasing concentration 4-ABT solutions recorded on (d) Ag NPs – LIG 405 nm, (e) Ag NPs – LIG 450 nm; (f) Ag NPs – LIG 10.6 μm. All spectra were recorded with 532 nm laser excitation wavelength, laser power 0.7 mW, 10 s integration time.

Figure 2.2a shows the Raman spectra of LIG materials obtained with the three laser illuminations. The structure written at 405 nm (black line) only displayed two broad bands at 1343 and 1579 cm^{-1} corresponding the D and G vibrations typical of amorphous carbon materials.[38] This corresponds with incomplete LIG formation, as evidenced by the smooth morphology of the carbonaceous material formed under the above writing conditions (see figure 2.1a). In contrast, LIG materials obtained with visible and CO_2 illumination (figure 2.2a red and blue lines) displayed sharp and well-defined D (1342 cm^{-1}), G (1572 cm^{-1}) and 2D (2680 cm^{-1}) bands, typical of crystalline graphene-like materials and very much in line with the characteristic bands obtained for other reported LIG materials on polyimide. The contact angle of the three LIG structures were 87°, 138° and 145°, respectively. Investigation of the SERS capabilities of fabricated hybrid Ag NPs – LIG structures was carried out using 4-ABT

as model molecule. Figure 2.2b reports Raman spectra of 4-ABT powder displaying sharp bands at 1006, 1084, 1174, 1492 and 1590 cm^{-1}, in agreement with literature data.[39] Figure 2.2b also shows a spectrum of 4-ABT (1×10^{-6} M) deposited on a LIG-450 nm surface in absence of Ag NPs. The spectrum dis- played only LIG peaks and absence of any SERS effect. Figure 2.2c shows spectra of 4-ABT (1×10^{-6} M) obtained from Ag NPs – LIG structures written with the different lasers. All spectra dis- played the typical SERS features of 4-ABT, characterized by 1075 (a_1), 1146 (b_2), 1188 (a_1), 1388 (b_2), 1436 (b_2) and 1578 (b_2) cm^{-1} peaks. The SERS bands at 1146 (b_2), 1388 (b_2), 1436 (b_2) and 1578 (b_2) cm^{-1} were assigned to the fundamental benzene ring vibrations.[40] The concomitant shift of a_1 peaks and the appearance of b_2 in plane, out of phase vibrational modes peaks was ascribed to the interaction between the 4-ABT and the Ag NPs, resulting from a metal-molecule charge transfer and has been identified as clear proof of the occurrence of a chemical enhanced process related to SERS effect.[39,40] The enhancement of b_2 modes (peaks assigned at 1146, 1388, 1436 and 1578 cm^{-1}) has also been reported to be indicative of a 4-ABT orientation perpendicular to the Ag NPs.[41] Figure 2.2d–f report the SERS capabilities of the three Ag NPs – LIG substrates exposed to solutions of 4-ABT of decreasing concentrations. Using the Ag NPs – LIG 405 nm substrate concentrations as low as 1×10^{-8} M were detected, whereas 1×10^{-9} M and 1×10^{-12} M were reached for Ag NPs – LIG 450 nm and Ag NPs – LIG 10.6 μm, respectively.

Even though Ag NPs – LIG 10.6 μm gave the strongest SERS effect with 4-ABT, EC-SERS characterization was carried out with Ag NPs – LIG 450 nm substrates, as they provided more reproducible SERS results.

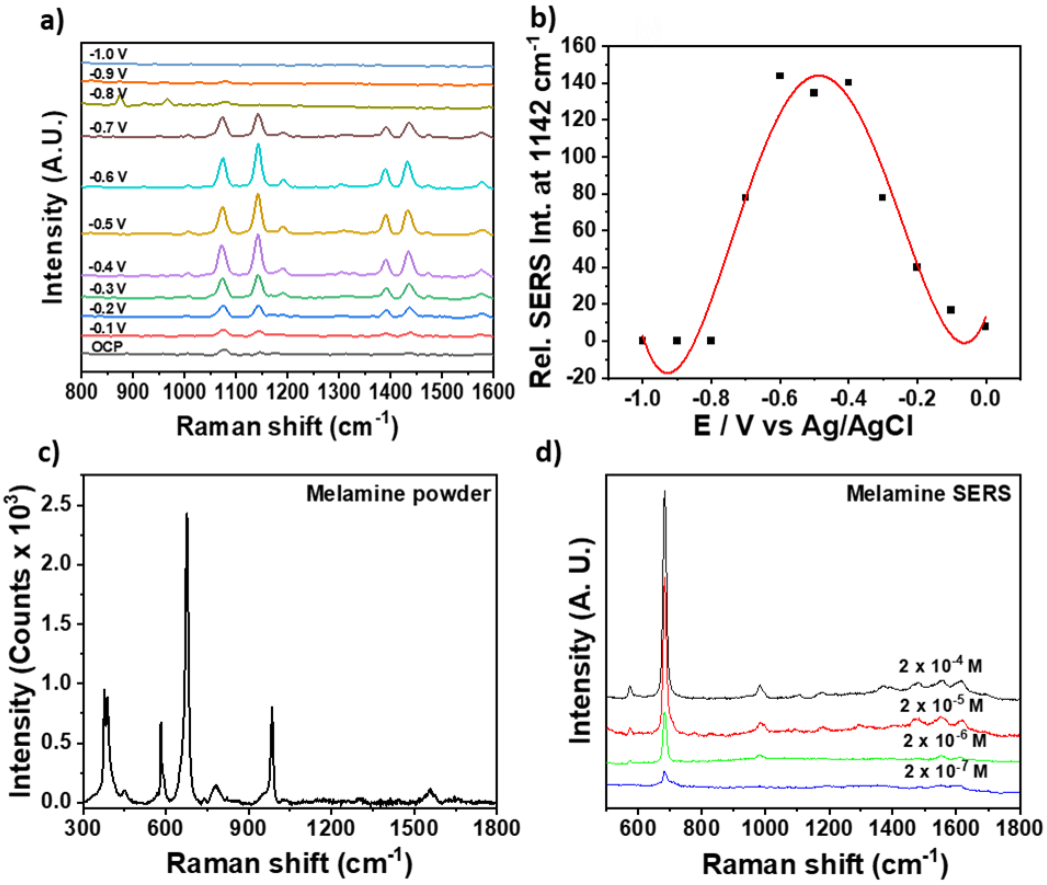

Figure 2.3 (a) EC-SERS spectra of 1×10^{-5} M 4-ABT recorded on 450 nm Ag NP-LIG electrode in 0.1 M NaF; **(b)** potential dependence of 4-ABT SERS intensity band at 1142 cm^{-1}. Red line is the fitting curve of the data. **(c)** Raman spectrum of melamine powder; **(d)** SERS spectrum of melamine solutions of different concentrations (PBS) deposited on Ag NPs – LIG 450 nm substrate. All spectra were recorded with at 785 nm excitation, 10 s acquisition time and 0.15 mW laser power.

Figure 2.3a shows the EC-SERS spectra measured for 4-ABT in the electrochemical cell in presence of 0.1 M NaF as supporting electrolyte. SERS spectra were recorded while stepping the potential in the cathodic direction (from 0.0 to −0.1 V) in 100 mV increments. An open circuit potential (OCP) spectrum was also measured, equivalent to the signal produced by the system in absence of applied potential. Under OCP conditions only the peaks at 1074 and 1141 cm^{-1} were visible. As the potential was stepped in the cathodic direction, significant changes were observed in the corresponding 4-ABT SERS spectra as the intensity of the b_2 bands at 1141, 1391 and 1432 cm^{-1} gradually increased between −0.1 and −0.6 V and decreased upon

further potential decrease. The observed trend is in line with data reported by Robinson et al., and is ascribed to the transition from 4-aminobenzenethiol to p,p′-dimercaptoazobenzene (DMAB) by selective catalytic coupling reaction on the Ag NPs.[30] The occurrence of this transition in the SERS spectra of 4-ABT has been investigated in details, and is sup- ported here by the strong increase of all b_2 vibrations (1142, 1391 and 1432 cm^{-1}) associated with formation of –N=N– bonds. Figure 2.3b shows the variation of peak intensity for the b_2 vibration at 1141 cm^{-1} across the potential range analysed. The intensity of the band increased up to −0.6 V and then decreased signalling the re-conversion of DMAB to 4-ABT at negative potentials. The EC-SERS response of hybrid LIG electrodes was further characterized with melamine, a product often added to food to boost its apparent nitrogen content. The Raman spectrum of melamine powder is shown in figure 2.3c and it was characterized by two main peaks at 675 and 985 cm^{-1}, both associated to ring breathing modes of the triazine ring.[42]

Figure 2.4a shows the EC-SERS response of melamine (2×10^{-5} M) in PBS buffer as the electrode potential is stepped in the cathodic direction from −0.1 to −0.9 V. Starting from the OCP spectrum, the intensity of 680 cm^{-1} peak decreased and then increased to relative maximum value until the potential reached −0.4 V. As the voltage became increasingly negative, the intensity of the 680 cm^{-1} peak decreased and its maximum shifted to 677 cm^{-1}, as already reported elsewhere.[30] Fig. 4b shows SERS spectra of melamine in milk (diluted 10 times) at different concentrations. Concentrations as low as 0.2 ppm of melamine in milk matrix were identified by the characteristic peak at 683 cm^{-1} by using Ag NPs – LIG 450 nm electrodes. This con- centration is ten times lower than the maximum residue limit (MRL) of 2.5 ppm set by the standard of US Food and Drug Administration.[43] It is worth noting that this low detection limit was reached even in the milk complex matrix and in absence of cumbersome extraction or pre-treatment processes. Figure 2.4c and 2.4d show cathodic and anodic voltage sequences for melamine (2×10^{-5} M) in milk recorded with Ag NPs – LIG 450 nm electrodes.

At OCP a prominent band at 685 cm^{-1} was observed. This band decreased in intensity as the voltage became more negative. The opposite trend was observed in the anodic sequence (**figure 2.4d**) as the intensity of the 684 cm^{-1} band increased gradually with the stepping of the potential to more positive values. These data show how the combination of SERS and EC readout contributed to provide a clear signal for melamine even in a complex matrix such as milk with only a simple dilution of the matrix and the avoidance of cumber- some pre-analytical steps.

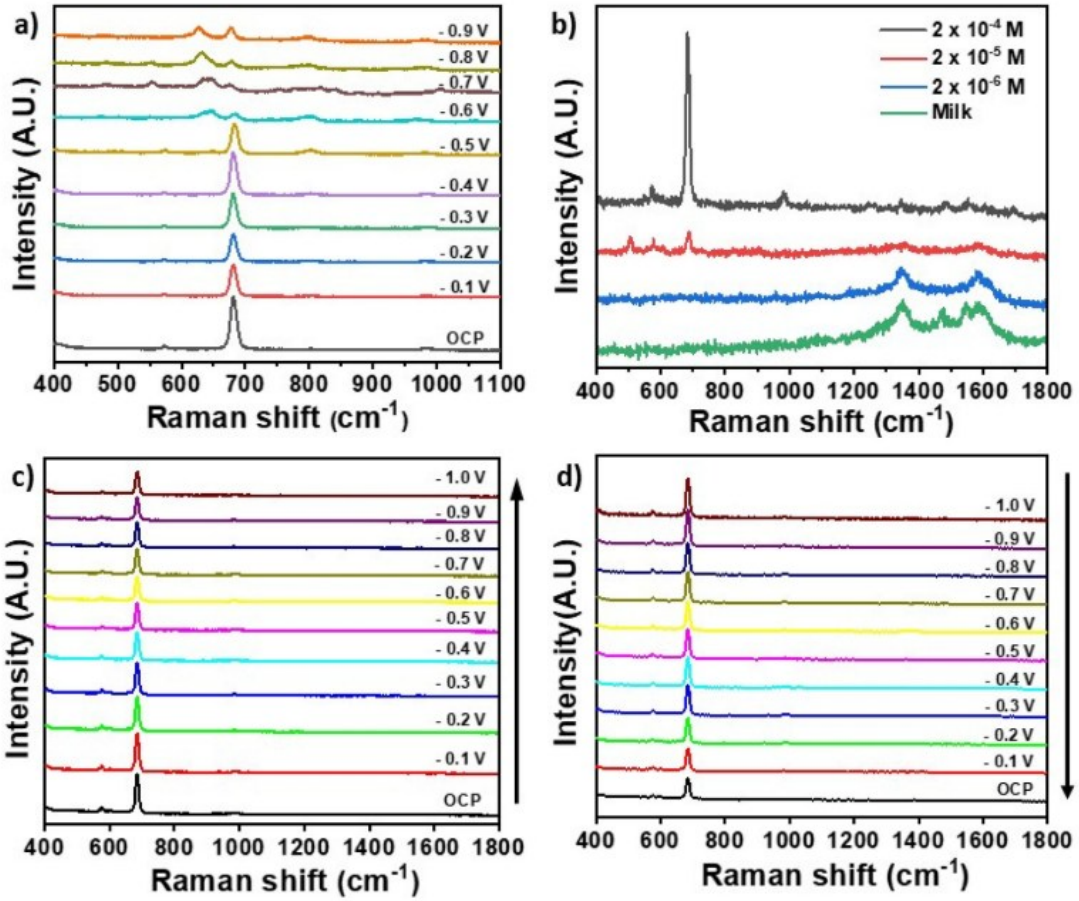

Figure 2.4 (a) EC-SERS spectra of 2 × 10^{-5} M melamine in PBS recorded on Ag NPs – LIG 450 nm electrode in 0.1 M NaF at 785 nm excitation, 10 s acquisition time and 15 mW laser power; (b) SERS spectra of melamine in milk; (c) cathodic and (d) anodic EC-SERS sequences of melamine (2 × 10^{-5} M) in milk on Ag NPs – LIG 450 nm electrode at 785 nm excitation.

As further example of real analyte detection, difloxacin (DIF) hydrochloride was chosen as it is a broad spectrum, synthetic fluoroquinolone antibiotic widely used in veterinary medicine, particularly for the treatment of infected dermal wounds in dogs, for its bactericidal activity. DIF accumulates in tissues and therefore the recommended daily dose is 5–10 $mg.kg^{-1}$ and its

use is not recommended for longer than 30 days.[44]

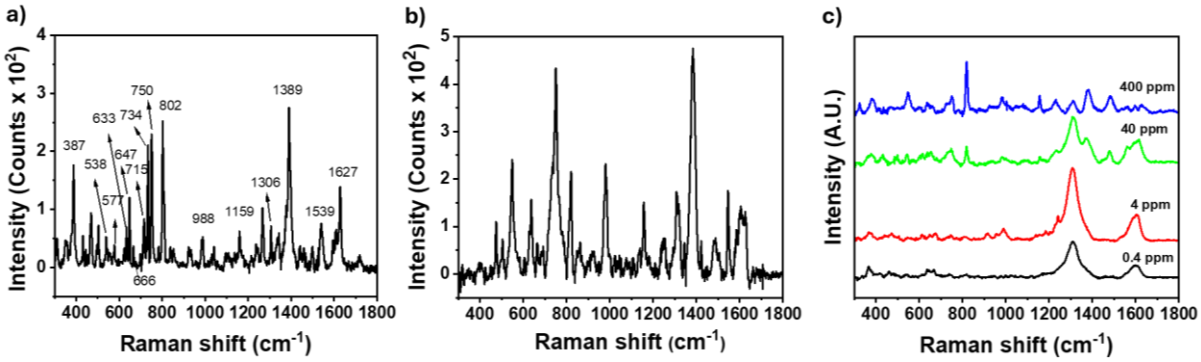

Figure 2.5 a) Raman spectrum of DIF powder; b) SERS spectrum of DIF deposited on Ag NPs – LIG 450 nm substrate; c) SERS spectra of DIF at different concentrations acquired with 785 nm laser illumination.

Figure 2.5a shows Raman spectrum of DIF powder on glass and DIF deposited on Ag NPs – LIG 450 nm substrate, respectively. It showed peaks at 1307 cm^{-1} (pyrazine ring vibrations), 1393 cm^{-1} (ν_{ring} quinolone ring), 1463 and 1448 cm^{-1} assigned to the normal modes involving contributions from piperazine moiety and angular deformation from CH_2 and CH_3 groups, 1498 cm^{-1} (δ_{CH2}), 1541 cm^{-1} (CO stretching mode of the carboxylate moiety $\nu_{C=O}$), 1629 cm^{-1} ($\nu_{C=C}$ aromatic ring). Figure 2.5b shows the SERS spectra of DIF solution (1×10^{-3} M, H_2O:CH_3CN 1:1) deposited on Ag NPs - LIG-450 nm measured by using 785 nm laser irradiation. Compared to the Raman spectrum, the intense SERS bands at 1546, 1340, 920, 785 and 548 cm^{-1} (related to C ring and carboxylate stretching) have significant contribution allowing to infer such molecular moieties are involved in the interaction with the metallic surface. Also, SERS peaks at 1625, 1340, 1051, 747 and 550 cm^{-1} (C-C, C-N stretching vibrations from aromatic rings) have important contributions suggesting an almost perpendicular orientation of these rings on the surface. Figure 2.5c shows the SERS spectra of DIF solutions of various concentrations (400 ppm equal to 1×10^{-3} M) deposited on Ag NPs – LIG 450 nm substrate. Characteristic peaks of DIF were visible down to 0.4 ppm (0.4 mg/L).

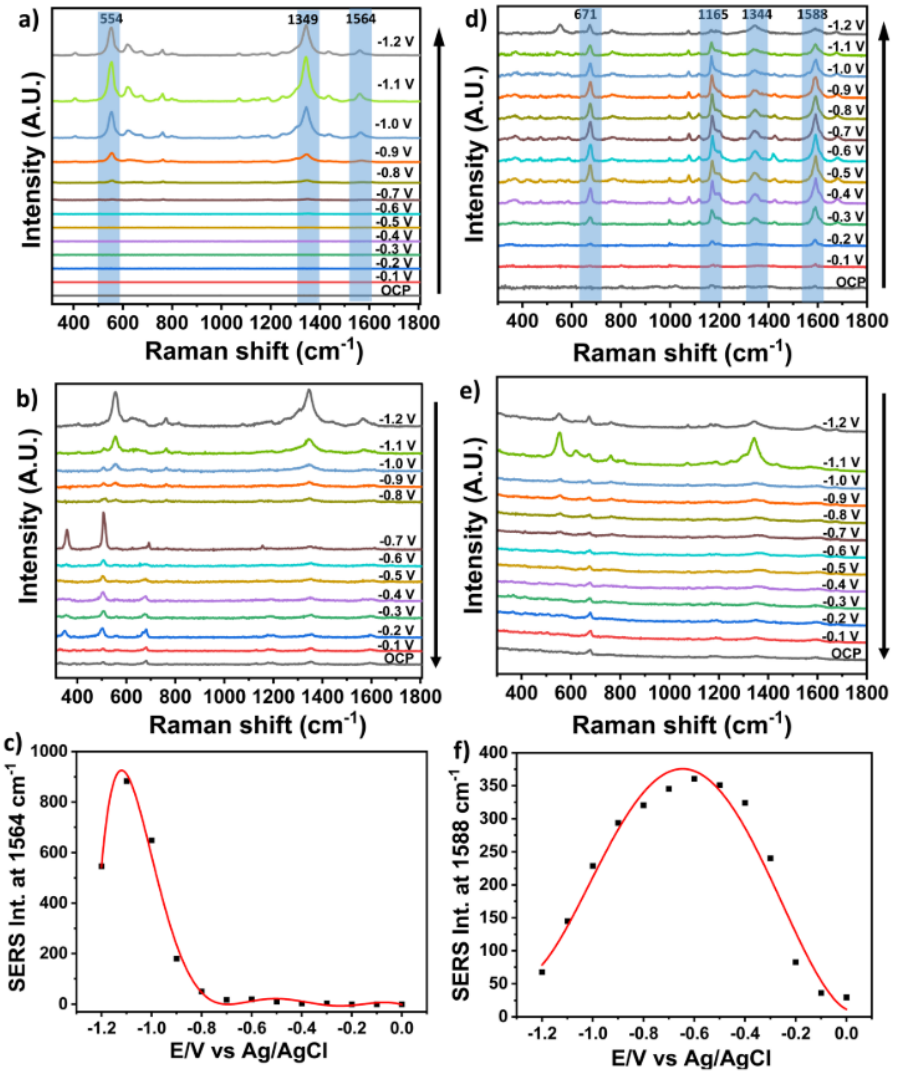

Figure 2.6 (a) Cathodic and (b) anodic EC-SERS sequences of DIF in DI water; (c) potential dependence of DIF SERS intensity band at 1564 cm^{-1} in DI water; (d) cathodic and (e) anodic EC-SERS sequences of DIF in river water; (f) potential dependence of DIF SERS intensity band at 1588 cm^{-1} in river water. All data were recorded using Ag NPs – LIG 450 nm electrode at 785 nm excitation.

Figure 2.6 shows the EC-SERS cathodic (figure 2.6a and d) and anodic **(figure 2.5b and e)** sequences of DIF recorded with 785 nm laser excitation in 100 mV steps in DI water and river water. The cathodic series recorded in DI water (figure 2.6a) until −1.2 V showed featureless SERS spectra at OCP and until the potential reached −0.7 V. For increasingly negative applied potentials SERS spectra were generated which increased in intensity as the potential was stepped to increasingly negative values. The SERS spectra displayed highest intensities at −1.2 V and decreased in intensity as the potential was swept back to 0 V in the anodic direction

(figure 2.6b). Interestingly, the 1536 cm^{-1} peak increased in intensity, as well as the 554 and 1349 cm^{-1} bands. For a very structurally similar molecule, levofloxacin, it has been reported that the appearance of the 1588 cm^{-1} band (CO stretching mode of the carboxylate moiety ν_C = O) is consistent with a bidentate chelate coordination, allowing to suggest that the carboxylate could be the anchor site of DIF adsorption.[45] The concomitant increase of the other bands, associated with stretching and bending of bonds close to the carboxylate moiety further confirmed this hypothesis.[45] Finally, EC-SERS measurements of DIF were carried out in river water. For these studies DIF (10 μL, 1×10^{-3} M) was mixed with filtered river water (90 μL) containing 0.1 M NaF as electrolyte. As already reported for DI water, an increase of SERS bands (figure 2.6d) occurred as the potential of the cathodic series was swept to increasingly negative values. Particularly, peaks at 671, 1165, 1344 and 1588 cm^{-1} were enhanced, again suggesting a coordination to the metal sites through the carboxylic group. The enhanced peaks gradually disappeared in the anodic series (figure 2.6e) as the potential was swept back from −1.2 to 0 V. Figure 2.6c, f show the change of SERS intensity of the 1564 cm^{-1} band and 1588 cm^{-1} with decreasing potential in DI and river water, respectively. In the case of DI water, the band increased as the potential decreased up to −1 V and then decreased at further negative potentials. For river water a similar trend was observed but at lower potentials. The association of the appearance of the 1588 cm^{-1} band with the occurrence of a carboxylate bidentate chelate coordination suggested a transition in coordination of the DIF molecule from mono- to bis-chelate as the potential was swept in the cathodic direction.

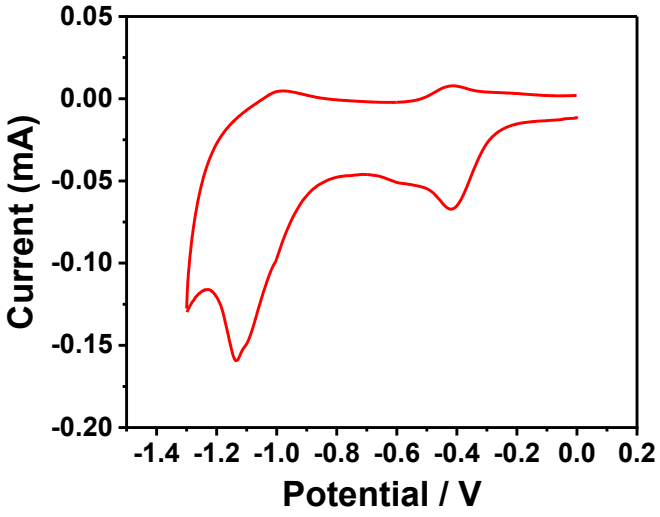

Figure 2.7 Cyclic Voltammogram of para-aminobenzenethiol (4-ABT) on AgNP modified LIG electrode with a potential scan rate of 10 mV/s.

To elucidate the potential-dependent variations in the Raman signals observed for b_2 modes (assigned at 1146, 1388, 1436, and 1578 cm^{-1}), a potential-dependent electrochemical measurement was performed on 4-ABT adsorbed onto an AgNP–LIG electrode in the absence of Raman laser irradiation. This approach minimizes the influence of laser illumination, which can otherwise induce a potential shift at the point of maximum intensity through the photon-driven charge transfer (PDCT) process. Figure 2.7 presents cyclic voltammogram (CV) of 4-ABT on an AgNP-modified laser-induced graphene (LIG) electrode. A cathodic process is evident in the Faradaic region at potentials more negative than –0.2 V, reaching a maximum near –0.4 V. This feature likely results from the synergistic influence of electrochemical reduction and PDCT. However, since no Raman laser irradiation was applied in this experiment, the observed behavior can be attributed solely to electrochemical reduction. This interpretation is further supported by Figure 2.3b, which displays the corresponding potential-dependent SERS response. Consequently, the obtained SERS spectra can be considered as a combined contribution from both 4-ABT and its oxidative product, DMAB.[46]

At more negative potentials, the in-situ generated DMAB molecule undergoes electrochemical reduction back to 4-ABT, as evident by the declining SERS intensity of the "b_2" bands. When

the potential is driven beyond –0.4 V, this reduction process may also promote desorption of the electrochemically produced DMAB species, eventually initiating the hydrogen evolution reaction (HER) at approximately –0.82 V. At highly negative potentials, near –0.8 V, DMAB is completely reduced to 4-ABT, resulting in SERS spectra characteristic exclusively of 4-ABT. Based on these observations, it is proposed that 4-ABT initially undergoes an interfacial oxidation process to form azo species (DMAB) on the AgNP surface [47] at relatively positive potentials under low-power Raman laser illumination, while subsequent electrochemical reduction reverses this transformation by eliminating DMAB. The interplay between these two opposing processes gives rise to the bell-shaped potential-dependent SERS peak intensity profile observed in figure 2.3b. Furthermore, the localized heating effect on the Ag-nanoparticles may significantly influence surface reactions and interfacial dynamics, serving as a key factor in the reversible chemical transformation between 4-ABT and DMAB observed in this study.

2.5 Conclusions

In this work a novel LIG-based electrode was proposed for the realization of versatile EC-SERS detection platforms. The merit of the combined EC-SERS methodology was demonstrated through sensitive detection of food contaminants and residual antibiotics in relevant matrices. Melamine and DIF were rapidly detected at concentrations lower than their relative MRL without the need to pre-treatment steps and with no interference from milk and water river matrices, respectively. EC-SERS approaches are characterized by low-cost instrumentation and rapid/selective signal acquisition. The development of flexible and versatile hybrid materials, such the proposed Ag NPs – LIG electrodes, contributes to extend the use of EC-SERS approaches to the monitoring of food quality/security/traceability and the monitoring of the environmental impact associated to farming and veterinary drugs.

2.6 References

[1] T. T. X. Ong, E. W. Blanch, and O. A. H. Jones, "Surface Enhanced Raman Spectroscopy in environmental analysis, monitoring and assessment," Sci. Total Environ., vol. 720, p. 137601, 2020, doi: https://doi.org/10.1016/j.scitotenv.2020.137601.

[2] X.-S. Zheng, I. J. Jahn, K. Weber, D. Cialla-May, and J. Popp, "Label-free SERS in biological and biomedical applications: Recent progress, current challenges and opportunities," Spectrochim. Acta Part A Mol. Biomol. Spectrosc., vol. 197, pp. 56–77, 2018, doi: https://doi.org/10.1016/j.saa.2018.01.063.

[3] C. Liu, D. Xu, X. Dong, and Q. Huang, "A review: Research progress of SERS-based sensors for agricultural applications," Trends Food Sci. Technol., vol. 128, pp. 90–101, 2022, doi: https://doi.org/10.1016/j.tifs.2022.07.012.

[4] M. Lafuente, D. Sanz, M. Urbiztondo, J. Santamaría, M. P. Pina, and R. Mallada, "Gas phase detection of chemical warfare agents CWAs with portable Raman," J. Hazard. Mater., vol. 384, p. 121279, 2020, doi: https://doi.org/10.1016/j.jhazmat.2019.121279.

[5] J. Neng, Q. Zhang, and P. Sun, "Application of surface-enhanced Raman spectroscopy in fast detection of toxic and harmful substances in food," Biosens. Bioelectron., vol. 167, p. 112480, 2020, doi: https://doi.org/10.1016/j.bios.2020.112480.

[6] M. A. Fikiet et al., "Surface enhanced Raman spectroscopy: A review of recent applications in forensic science," Spectrochim. Acta Part A Mol. Biomol. Spectrosc., vol. 197, pp. 255–260, 2018, doi: https://doi.org/10.1016/j.saa.2018.02.046.

[7] D. Saviello et al., "A combined Surface Enhanced Raman Spectroscopy (SERS)/UV–vis approach for the investigation of dye content in commercial felt tip pens inks," Talanta, vol. 181, pp. 448–453, 2018, doi: https://doi.org/10.1016/j.talanta.2018.01.049.

[8] K. Xu, R. Zhou, K. Takei, and M. Hong, "Toward Flexible Surface-Enhanced Raman Scattering (SERS) Sensors for Point-of-Care Diagnostics," Adv. Sci., vol. 6, no. 16, 2019, doi: 10.1002/advs.201900925.

[9] X. X. Han, R. S. Rodriguez, C. L. Haynes, Y. Ozaki, and B. Zhao, "Surface-enhanced Raman spectroscopy," Nat. Rev. Methods Prim., vol. 1, no. 1, p. 87, 2022, doi: 10.1038/s43586-021-00083-6.

[10] H. Wang et al., “Coupling enhancement mechanisms, materials, and strategies for surface-enhanced Raman scattering devices,” Analyst, vol. 146, no. 16, pp. 5008–5032, 2021, doi: 10.1039/D1AN00624J.

[11] R. Pilot, R. Signorini, C. Durante, L. Orian, M. Bhamidipati, and L. Fabris, “A review on surface-enhanced Raman scattering,” Biosensors, vol. 9, no. 2, 2019, doi: 10.3390/bios9020057.

[12] J. Langer et al., “Present and Future of Surface-Enhanced Raman Scattering,” ACS Nano, vol. 14, no. 1, pp. 28–117, Jan. 2020, doi: 10.1021/acsnano.9b04224.

[13] H. Park, W. Park, and C. H. Lee, “Electrochemically active materials and wearable biosensors for the in situ analysis of body fluids for human healthcare,” NPG Asia Mater., vol. 13, no. 1, p. 23, 2021, doi: 10.1038/s41427-020-00280-x.

[14] M. Cuartero, “Electrochemical sensors for in-situ measurement of ions in seawater,” Sensors Actuators B Chem., vol. 334, p. 129635, 2021, doi: https://doi.org/10.1016/j.snb.2021.129635.

[15] R. Ye, D. K. James, and J. M. Tour, “Laser-Induced Graphene,” Acc. Chem. Res., vol. 51, no. 7, pp. 1609–1620, Jul. 2018, doi: 10.1021/acs.accounts.8b00084.

[16] J. Lin et al., “Laser-induced porous graphene films from commercial polymers,” Nat. Commun., vol. 5, no. 1, p. 5714, 2014, doi: 10.1038/ncomms6714.

[17] X. Kong, P. Gai, L. Ge, and F. Li, “Laser-Scribed N-Doped Graphene for Integrated Flexible Enzymatic Biofuel Cells,” ACS Sustain. Chem. Eng., vol. 8, no. 33, pp. 12437–12442, Aug. 2020, doi: 10.1021/acssuschemeng.0c03051.

[18] L. Ge, Q. Hong, H. Li, C. Liu, and F. Li, “Direct-Laser-Writing of Metal Sulfide-Graphene Nanocomposite Photoelectrode toward Sensitive Photoelectrochemical Sensing,” Adv. Funct. Mater., vol. 29, no. 38, pp. 1–10, 2019, doi: 10.1002/adfm.201904000.

[19] L. Ge, Q. Hong, H. Li, and F. Li, “A laser-induced TiO2-decorated graphene photoelectrode for sensitive photoelectrochemical biosensing,” Chem. Commun., vol. 55, no. 34, pp. 4945–4948, 2019, doi: 10.1039/C9CC00889F.

[20] X. Liu, H. Cheng, Y. Zhao, Y. Wang, and F. Li, “Portable electrochemical biosensor based on laser-induced graphene and MnO2 switch-bridged DNA signal amplification

for sensitive detection of pesticide," Biosens. Bioelectron., vol. 199, p. 113906, 2022, doi: https://doi.org/10.1016/j.bios.2021.113906.

[21] D. Iacopino et al., "Visible laser scribing fabrication of porous graphitic carbon electrodes: Morphologies, electrochemical properties, and applications as disposable sensor platforms," ACS Appl. Electron. Mater., vol. 2, no. 10, pp. 3279–3288, 2020, doi: 10.1021/acsaelm.0c00612.

[22] P. Nayak, N. Kurra, C. Xia, and H. N. Alshareef, "Highly Efficient Laser Scribed Graphene Electrodes for On-Chip Electrochemical Sensing Applications," Adv. Electron. Mater., vol. 2, no. 10, pp. 1–11, 2016, doi: 10.1002/aelm.201600185.

[23] Y. Han, Y. Han, Q. He, H. Liu, Y. Zhang, and L. Han, "Ultrasensitive and Reliable SERS Chip Based on Facile Assembly of AgNPs on Porous LIG to Enhance the Local Electromagnetic Field," J. Phys. Chem. C, vol. 127, no. 8, pp. 4195–4202, Mar. 2023, doi: 10.1021/acs.jpcc.2c08038.

[24] H. K. Lee et al., "Designing surface-enhanced Raman scattering (SERS) platforms beyond hotspot engineering: emerging opportunities in analyte manipulations and hybrid materials," Chem. Soc. Rev., vol. 48, no. 3, pp. 731–756, 2019, doi: 10.1039/C7CS00786H.

[25] Y. Han et al., "Controllable Nanoparticle Aggregation through a Superhydrophobic Laser-Induced Graphene Dynamic System for Surface-Enhanced Raman Scattering Detection," ACS Appl. Mater. Interfaces, vol. 14, no. 2, pp. 3504–3514, Jan. 2022, doi: 10.1021/acsami.1c21159.

[26] A. V Markin, A. I. Arzhanukhina, N. E. Markina, and I. Y. Goryacheva, "Analytical performance of electrochemical surface-enhanced Raman spectroscopy: A critical review," TrAC Trends Anal. Chem., vol. 157, p. 116776, 2022, doi: https://doi.org/10.1016/j.trac.2022.116776.

[27] R. Moldovan et al., "Review on combining surface-enhanced Raman spectroscopy and electrochemistry for analytical applications," Anal. Chim. Acta, vol. 1209, 2022, doi: 10.1016/j.aca.2021.339250.

[28] N. Albarghouthi, M. M. Eisnor, C. C. Pye, and C. L. Brosseau, "Electrochemical Surface-Enhanced Raman Spectroscopy (EC-SERS) and Computational Study of Atrazine:

Toward Point-of-Need Detection of Prevalent Herbicides," J. Phys. Chem. C, vol. 126, no. 23, pp. 9836–9842, Jun. 2022, doi: 10.1021/acs.jpcc.2c02337.

[29] B. H. C. Greene, D. S. Alhatab, C. C. Pye, and C. L. Brosseau, "Electrochemical-Surface Enhanced Raman Spectroscopic (EC-SERS) Study of 6-Thiouric Acid: A Metabolite of the Chemotherapy Drug Azathioprine," J. Phys. Chem. C, vol. 121, no. 14, pp. 8084–8090, Apr. 2017, doi: 10.1021/acs.jpcc.7b01179.

[30] A. M. Robinson, S. G. Harroun, J. Bergman, and C. L. Brosseau, "Portable Electrochemical Surface-Enhanced Raman Spectroscopy System for Routine Spectroelectrochemical Analysis," Anal. Chem., vol. 84, no. 3, pp. 1760–1764, Feb. 2012, doi: 10.1021/ac2030078.

[31] S. D. Bindesri, R. Jebailey, N. Albarghouthi, C. C. Pye, and C. L. Brosseau, "Spectroelectrochemical and computational studies of tetrahydrocannabinol (THC) and carboxy-tetrahydrocannabinol (THC-COOH)," Analyst, vol. 145, no. 5, pp. 1849–1857, 2020, doi: 10.1039/C9AN02173F.

[32] C. Ott, A. Burns, E. Sisco, and L. E. Arroyo, "Targeted fentanyl screening utilizing electrochemical surface-enhanced Raman spectroscopy (EC-SERS) applied to authentic seized drug casework samples," 2023, doi: https://doi.org/10.1016/j.forc.2023.100492.

[33] M. M. Eisnor, K. E. R. McLeod, S. Bindesri, S. A. Svoboda, K. L. Wustholz, and C. L. Brosseau, "Electrochemical surface-enhanced Raman spectroscopy (EC-SERS): a tool for the identification of polyphenolic components in natural lake pigments," Phys. Chem. Chem. Phys., vol. 24, no. 1, pp. 347–356, 2022, doi: 10.1039/D1CP03301H.

[34] S. D. Bindesri, D. S. Alhatab, and C. L. Brosseau, "Development of an electrochemical surface-enhanced Raman spectroscopy (EC-SERS) fabric-based plasmonic sensor for point-of-care diagnostics," Analyst, vol. 143, no. 17, pp. 4128–4135, 2018, doi: 10.1039/C8AN01117F.

[35] P. C. Lee and D. Meisel, "Adsorption and surface-enhanced Raman of dyes on silver and gold sols," J. Phys. Chem., vol. 86, no. 17, pp. 3391–3395, Aug. 1982, doi: 10.1021/j100214a025.

[36] M. Burke et al., "Fabrication and Electrochemical Properties of Three-Dimensional (3D) Porous Graphitic and Graphenelike Electrodes Obtained by Low-Cost Direct Laser

Writing Methods," ACS Omega, vol. 5, no. 3, pp. 1540–1548, 2020, doi: 10.1021/acsomega.9b03418.

[37] R. Murray, M. Burke, D. Iacopino, and A. J. Quinn, "Design of Experiments and Optimization of Laser-Induced Graphene," ACS Omega, vol. 6, no. 26, pp. 16736–16743, 2021, doi: 10.1021/acsomega.1c00309.

[38] Z. Li, L. Deng, I. A. Kinloch, and R. J. Young, "Raman spectroscopy of carbon materials and their composites: Graphene, nanotubes and fibres," Prog. Mater. Sci., vol. 135, p. 101089, 2023, doi: https://doi.org/10.1016/j.pmatsci.2023.101089.

[39] K. Kim, H. B. Lee, D. Shin, H. Ryoo, J. W. Lee, and K. S. Shin, "Surface-enhanced Raman scattering of 4-aminobenzenethiol on silver: Confirmation of the origin of b2-type bands," J. Raman Spectrosc., vol. 42, no. 12, pp. 2112–2118, 2011, doi: 10.1002/jrs.2972.

[40] M. Osawa, N. Matsuda, K. Yoshii, and I. Uchida, "Charge transfer resonance Raman process in surface-enhanced Raman scattering from p-aminothiophenol adsorbed on silver: Herzberg-Teller contribution," J. Phys. Chem., vol. 98, no. 48, pp. 12702–12707, Dec. 1994, doi: 10.1021/j100099a038.

[41] Y. Wang, S. Guo, H. Chen, and E. Wang, "Facile fabrication of large area of aggregated gold nanorods film for efficient surface-enhanced Raman scattering," J. Colloid Interface Sci., vol. 318, no. 1, pp. 82–87, 2008, doi: https://doi.org/10.1016/j.jcis.2007.09.057.

[42] N. E. Mircescu, M. Oltean, V. Chiş, and N. Leopold, "FTIR, FT-Raman, SERS and DFT study on melamine," Vib. Spectrosc., vol. 62, pp. 165–171, 2012, doi: https://doi.org/10.1016/j.vibspec.2012.04.008.

[43] A. Filazi, U. T. Sireli, H. Ekici, H. Y. Can, and A. Karagoz, "Determination of melamine in milk and dairy products by high performance liquid chromatography," J. Dairy Sci., vol. 95, no. 2, pp. 602–608, 2012, doi: https://doi.org/10.3168/jds.2011-4926.

[44] Center for Veterinary Medicine. "FOIA Drug Summaries – NADA 141-096 Dicural® Tablets – original approval". www. fda.gov. Retrieved on 30-11-2015

[45] A. L. Filgueiras, D. Paschoal, H. F. Dos Santos, and A. C. Sant'Ana, "Adsorption study of antibiotics on silver nanoparticle surfaces by surface-enhanced Raman scattering spectroscopy," Spectrochim. Acta Part A Mol. Biomol. Spectrosc., vol. 136, pp. 979–985, 2015, doi: https://doi.org/10.1016/j.saa.2014.09.120.

[46] Y. F. Huang, H. P. Zhu, G. K. Liu, D. Y. Wu, B. Ren, and Z. Q. Tian, “When the signal is not from the original molecule to be detected: Chemical transformation of para-Aminothiophenol on ag during the SERS measurement,” *J. Am. Chem. Soc.*, vol. 132, no. 27, pp. 9244–9246, 2010, doi: 10.1021/ja101107z.

[47] Abdessamad Grirrane et al., Gold-Catalyzed Synthesis of Aromatic Azo Compounds from Anilines and Nitroaromatics. Science 322, 1661-1664 (2008). DOI:10.1126/science.1166401

Chapter 3: Laser-Induced Graphene Supercapacitors by Direct Laser Writing of Cork Natural Substrates

3.1 Abstract

Interdigitated and square laser-induced graphene (LIG) electrodes were successfully fabricated by direct laser writing of common natural cork bottle stoppers. The laser graphitization process was performed with a low-cost hobbyist visible laser in a simple, fast, and one-step process under ambient conditions. The formation of LIG material was revealed by extensive characterization using Raman, attenuated total reflection- Fourier transform infrared (ATR-FTIR), and X-ray photoelectron (XPS) spectroscopies. Electron microscopy investigation showed that the formed LIG structure maintained the hierarchical alveolar structure of the pristine cork but displayed increased surface area, disorder, and electrical conductivity, promising for electrochemical applications. Open planar and sandwich supercapacitors, assembled from fabricated electrodes using poly(vinyl alcohol) PVA/H^+ as an electrolyte, exhibited a maximum areal capacitance of 1.56 mF/cm^2 and 3.77 mF/cm^2 at a current density 0.1 mA/cm^2, respectively. Upon treatment with boric acid (H_3BO_3), the areal capacitance of the resulting boron-doped LIG devices increased by ca. three times, reaching 4.67 mF/cm^2 and 11.24 mF/cm^2 at 0.1 mA/cm^2 current density for planar and sandwich configurations, respectively. Supercapacitor devices showed excellent stability over time with only a 14% loss after >10 000 charge/discharge cycles. The easy, fast, scalable, and energy-efficient method of fabrication illustrated in this work, combined with the use of natural and abundant materials, opens avenues for future large-scale production of “green” supercapacitor devices.

3.2 Introduction

Graphene and graphene-like materials have recently received considerable attention due to their unique properties, which make them particularly suitable for energy storage applications.[1-3] In an attempt to make such materials more environmentally sustainable, a number of routes have been proposed for the ecofriendly fabrication of graphene,[4-6] graphene nanosheets,[7] graphene quantum dots,[8] graphene oxide (GO),[9] and reduced graphene oxide (rGO).[10,11] In parallel, carbon-based natural materials derived from abundant and renewable sources are also increasingly used as electrode materials as their biodegradability and potential cost-effectiveness make them attractive candidates for "green" energy storage applications.[12-15] For example, electrodes fabricated from tree bark, wood,[17] coconut leaves,[18] sunflower seed shells,[12] coconut shells,[20] and pistachio nutshells biomass have already been used in supercapacitor devices with reportedly high specific areal capacitances (CA) as high as 311 F g in a KOH electrolyte.[19] Among natural materials, cork is particularly interesting for its abundance and renewability.[22,23] Cork is harvested from the bark of cork oak trees (*Quercus suber* and *Quercus occidentalis*), growing in all the southern Mediterranean regions. Every 9-12 years, half of the bark from the trees is removed and subjected to various processes, leading to fabrication of cork for a wide range of applications. Cork is a lightweight material, impermeable to both liquids and gases, often associated with wood. However, unlike wood, cork granules can be considered as aggregates rather fibrous materials, possessing lower cellulose and hemicellulose content than wood. In addition, cork has a high chemical content of suberin, a polymer, made up of long-chain aliphatic alcohols and acid monomers and by a honeycomb microstructure, responsible for its overall excellent compressibility and impermeability.[23] Cork itself has shown suitability for green energy storage applications. Recently, amorphous carbon electrodes obtained from biomass Quercus suber have been used for the fabrication of natural supercapacitor devices which displayed specific capacitances of

166 F g^{-1} and power densities of 449.4 W kg^{-1}.[24,25] Unfortunately, despite the natural origins and abundance of the precursor materials, the generation of biomass is a high environmental footprint process, requiring pyrolysis and use of extracting solvents.[26] Recently, direct laser writing techniques have been developed allowing easy, low-carbon footprint, and high-yield generation of graphene-like carbon materials. In this method, highly porous and conductive laser-induced graphene (LIG) structures are obtained by patterning selected substrates with laser engraving tools under mild conditions (low laser power, <5 W, and room-temperature process).[27,28] The method is fast (minutes time scale), does not require the use of toxic or pollutant chemicals, and does not produce waste since the laser converts only selected areas of the substrate, avoiding the production of unusable excess material or waste.[29] By applying direct laser writing methods to commercial polyimide substrates (Kapton tape), researchers developed micro-supercapacitors showing excellent capacitive behaviour and an areal capacitance (CA) up to 16.5 mF/cm^2.[27,30–32] Recently, laser writing graphitization of natural and biodegradable substrates was also demonstrated. For example, Chyan et al. was able to graphitize a variety of natural materials such as paper, coconut shells, cloth, wood, and cork by applying a flame retardant layer onto the substrates and using a multilasing/defocusing approach.[33] In parallel, Ye et al. reported formation of LIG structures on pine wood using a CO_2 laser scribing technique under an inert atmosphere (Ar or H_2), thus avoiding ablation caused by the reaction between laser, wood, and atmospheric oxygen.[34] Interestingly, Lee et al. recently demonstrated the fabrication of LIG structures directly on untreated cellulose nanofiber (CNF) films via one-step CO_2 laser writing at ambient conditions. The direct graphitization (rather than ablation) was attributed to the presence of sodium atoms in the CNF structure arising from a TEMPO (2,2,6,6-tetramethylpiperidin-1-oxyl radical)-mediated oxidation reaction of the original bleached pulp.[35] In this work, we report the fabrication of LIG electrodes by simple, one-step direct visible laser writing of natural cork stoppers. By using

mild laser power conditions (0.9 W laser power), it was possible to obtain electrically conductive materials displaying an alveolar 3D morphology rich in defects and displaying an increased surface area compared to pristine cork. Interdigitated and square electrode geometries were fabricated and assembled into open and sandwich super- capacitor configurations, respectively. In order to enhance device performance, the cork initial substrate was treated with H_3BO_3 prior to laser graphitization, a process leading to formation of boron-doped LIG electrodes. Resulting devices exhibited CA of 4.67 and 11.24 mF/cm^2 at 0.1 mA/cm^2 current density for open and sandwich configurations, respectively. The devices also showed excellent stability over time with no significant loss after >10 000 charge/discharge cycles.

3.3 Experimental Section

3.3.1 Materials

Potassium chloride (KCl), sulfuric acid (H_2SO_4), poly-vinyl alcohol (PVA) (MW = 50 000), and boric acid (H_3BO_3) were purchased from SIGMA Aldrich and used without further purification. All solutions were prepared using deionized Milli-Q water (resistivity 18.2 MΩ·cm). Commercial cork stoppers (20 mm diameter) were purchased from a local store and used without further treatment.

3.3.2 Electrode Fabrication

Natural cork stoppers were cut in disks of about 3 mm width prior to laser engraving. LIG structures were fabricated by laser irradiation with a KKmoon compact automatic desktop laser engraving machine equipped with a laser with a wavelength of 450 nm and power of 3 W. A laser power of 0.9 W (30% of laser power) was used for LIG fabrication. Interdigitated and square electrode geometries were designed in Microsoft PowerPoint and then engraved by raster scanning of the laser beam on the cork surface to create the electrode pattern. Doped

interdigitated electrodes were fabricated by drop casting 0.5 mL of a 2.5% H_3BO_3 aqueous solution onto the interdigitated electrodes followed by evaporation at room temperature. Doped squared electrodes were fabricated by soaking a cork stopper disk in 2 mL of a 2.5% H_3BO_3 aqueous solution overnight and then dried at room temperature before laser fabrication of the electrodes.

3.3.3 Supercapacitor Assembly

A PVA electrolyte solution was prepared by stirring together 10 mL of deionized water with 1 g of PVA and 1 mL of H_2SO_4 at 80 °C overnight. For open in-plane supercapacitors, the electrolyte solution was drop-casted onto the interdigitated electrodes and used immediately for electrochemical measurements. Silver conductive paint (RS Pro, volume resistivity 1 mΩ) was applied and dried for 10 min on the electrode ends in order to ensure electrical connection with the electrochemical workstation for testing. Kapton tape strips were applied around the interdigitated electrodes to contain the electrolyte solution. For square electrodes, an O-ring of 7 mm inner diameter and 1.0 mm in thickness was placed in the center of an LIG square and filled with electrolyte solution. The area outside the O-ring was painted with silver paint to ensure electrical connections to the potentiostat and covered with Kapton tape to avoid short-circuiting of the final device. A second square LIG electrode was placed on top of the O-ring, and the resulting sandwiched structure was held tightly together in a screwed electrochemical cell for 48 h before electrochemical measurements.

3.3.4 Characterization

Surface morphology and elemental analysis of the sample were done using a Zeiss Supra scanning electron microscope (SEM) equipped with an Oxford X-Max 50 detector operating at an accelerating voltage of 10 kV for the (energy dispersive X-ray) EDS detector (Oxford X-Max with AZtec software). Samples were coated with ~10 nm film of AuPd (90% Au, 10%

Pd) prior to imaging. Bright field transmission electron microscopy (TEM) analysis was performed by means of a FEI Tecnai G12 Spirit Twin (LaB6 source) at 120 kV acceleration voltage. TEM images were collected on a FEI Eagle 4k CCD camera. Raman investigation was performed with a Horiba-XPlora instrument equipped with a 70 mW 532 nm laser diode. Spectra were acquired at a laser power of 10% and 30 s acquisition time. Attenuated total reflection-Fourier transform infrared (ATR-FTIR) analysis was carried out with a portable Bruker ALPHA II's Platinum ATR single reflection diamond ATR. X-ray photoelectron (XPS) measurements were performed in a UHV chamber (P ≈ 5 × 10−10 mbar) equipped with a SPECS Phoibos 100-1D-DLD hemispherical electron analyzer and a non-monochromatized dual-anode Mg/Al X- ray source for XPS. The XP spectra were recorded with MgKα at 1253.6 eV photon energy and an analyzer pass energy of 10 eV giving a full-width at half maximum (FWHM) of 0.85 eV for the Ag 3d5/2 line. The analyzed area was a spot of 3 mm diameter. The atomic ratios were calculated from the intensity (peak area) of the XPS peaks weighted with the corresponding relative sensitivity factors (RSF) derived from the Scofield cross-section taking into account the electron transport properties of the matrix and the energy analyzer transmission function. For spectra collection and treatment, including fitting, the commercial software SpecsLab Prodigy (by Specs GmbH, Berlin) was used. The XPS peaks were fitted by decomposing each spectrum into individual mixed Gaussian−Lorentzian peaks after a Shirley background subtraction. Surface wettability was measured using a Dataphysics OCA 20 wetting angle system in air at ambient temperature by dropping distilled water droplets (1 mm diameter) on the LIG electrode structures and bare cork surfaces. The average contact angle value was acquired by measuring at five different positions of the same sample. Thermal degradation of materials was evaluated by thermogravimetric analysis (TGA) that was carried out in N_2 flow (flow rate = 40 mL/min) using a TGAQ500-TA Instruments, at a heating rate of 10 °C/min in the temperature range from 35 to 1000 °C. Volumetric nitrogen adsorption

analysis was performed by means of a Micromeritics ASAP 2020 analyzer using high-purity gases (>99.999%). Nitrogen adsorption isotherms were collected at 77 K, and the Brunauer−Emmett−Teller (BET) specific surface area (SSA) was determined from the linear part of the isotherms. Nonlocal density functional theory (NLDFT) was applied to nitrogen adsorption isotherms to evaluate the pore size distribution of the nanoparticles. Prior to the analyses, the samples were degassed at 100 °C under a vacuum (p <10−5 mbar). The electrical conductivity of the fabricated LIG structures was determined through transfer line measurements (TLM). Transfer line structures (16 × 4 mm) were contacted directly using a probe station (Wentworth Laboratories PML 8000) at known separation lengths. Potential−current sweeps (−0.1 to 0.1 V, 10 mV step) were recorded using a parameter analyzer (Agilent 5270B). Cyclic voltammetry (CV), galvanostatic charge−discharge (GCD), and electrochemical impedance spectroscopy (EIS) measurements were performed with a CHI760C bipotentiostat electrochemical system at ambient conditions. The specific areal capacitance (CA) was calculated from galvanostatic charge−discharge (CC) curves using the standard equation,[24]

$$C_A = \frac{I}{S\ (dV/dt)}$$

where *I* is the constant discharge current, S is the total active area of both electrodes in square cm and dV/dt represents the slope of the discharge as obtained from the charge−discharge curve.

3.4 Results and Discussion

3.4.1 Morphological Characterisation

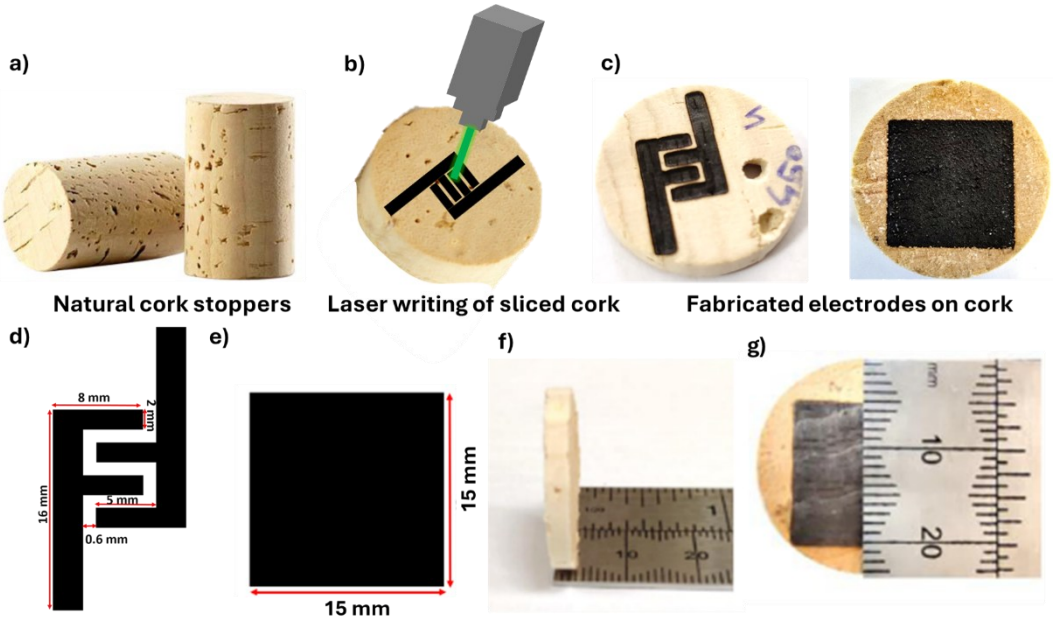

Scheme 3.1 Schematic representation of (a) commercial cork stoppers, (b) the direct laser writing method applied to sliced cork stoppers to fabricate electrode structures, (c) representative photographs of the fabricated interdigitated and square electrodes. (d) Interdigitated electrode pattern, (e) square electrode pattern for the sandwich configuration, (f) vertical view, and (g) top view of the electrodes

Scheme 3.1 shows the process of direct laser writing used to fabricate LIG electrodes by graphitization of cork substrates with a 450 nm laser as well as a photograph of the resulting interdigitated and square electrodes. Interdigitated electrodes had a total length of 16 mm, width of 2 mm, and spacing of 320 μm between two adjacent microelectrodes. Square electrodes were written with a size of 2.25 cm^2 (see scheme 3.1d-g show more details of electrodes and size). To optimize the graphitization conditions, LIG samples were produced by systematically changing the laser power (LP) between 30 and 70% and the laser depth adjustment (DA) between 20 and 50 (DA is a parameter inversely proportional to the laser speed). The images of the graphitized samples are reported in figure 1a. From a simple visual inspection of the 3 × 9 mm LIG features, it is clear that an increase of laser power beyond 40% resulted in smudging

and broadening of the graphitized areas for all DA conditions, with a more evident effect at low DA values. This first investigation restricted the range of laser power conditions to 30%. To select the best DA, a systematic Raman spectroscopy investigation of LIG material produced at 30% laser power and 20−40 DA was performed (see f**igure 3.1b** for representative spectra).

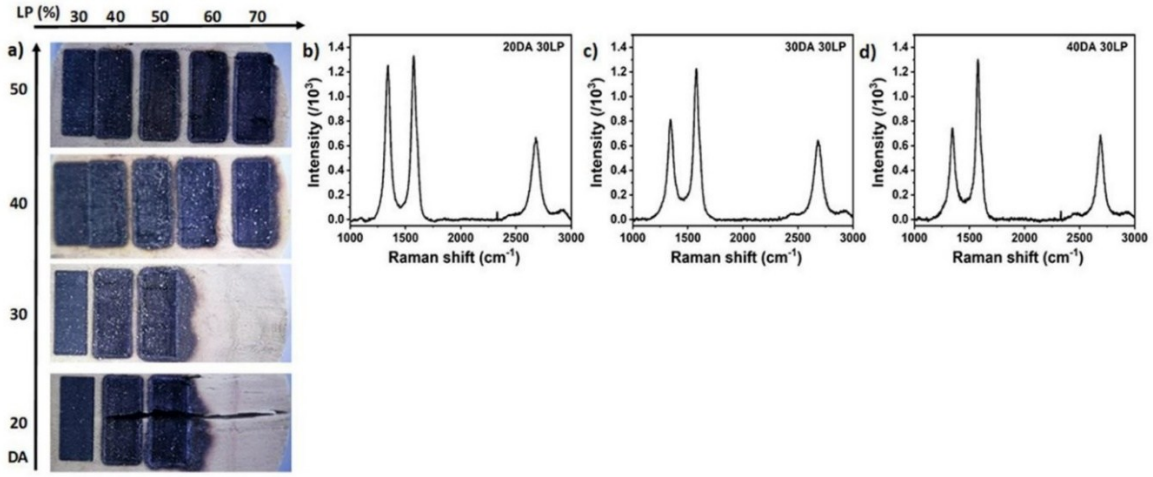

Figure 3.1 (a) Photograph of LIG features on cork obtained at different LP and DA conditions; (b−d) representative Raman spectra of LIG obtained at 20−40 DA and 30% LP.

Table 3.1 Raman Characteristics of Cork LIGs Obtained from Different DAs at 30% Laser Power

Sample (DA-LP)	**FWHM**			**I_D/I_G**	**I_{2D}/I_G**	**Pos-D**	**Pos-G**	**Pos-2D**
	D	**G**	**2D**					
20-30	58 (±6)	50 (±7)	87 (±8)	0.9 (±0.1)	0.5 (±0.1)	1341 (±1)	1574 (±1)	2679 (±1)
30-30	63 (±10)	51 (±5)	83 (±10)	0.7 (±0.2)	0.6 (±0.1)	1342 (±3)	1575 (±3)	2683 (±5)
40-30	71 (±10)	48 (±9)	70 (±11)	0.6 (±0.2)	0.5 (±0.03)	1346 (±2)	1578 (±2)	2690 (±5)

Table 3.1 reports the spectral characteristics of each sample (average of five spectra per sample). Collected data showed that the increase of the DA was associated with the sharpening the 2D peak and a lowering of the I_D/I_G ratio, suggesting formation of good-quality LIG material.[27] Furthermore, electrical measurements performed on the samples showed a decrease

in resistance from 135 to 73 Ω as DA increased from 20 to 40. On the basis of these data, the combination of 30% laser power and 40 DA was used throughout all experiments.

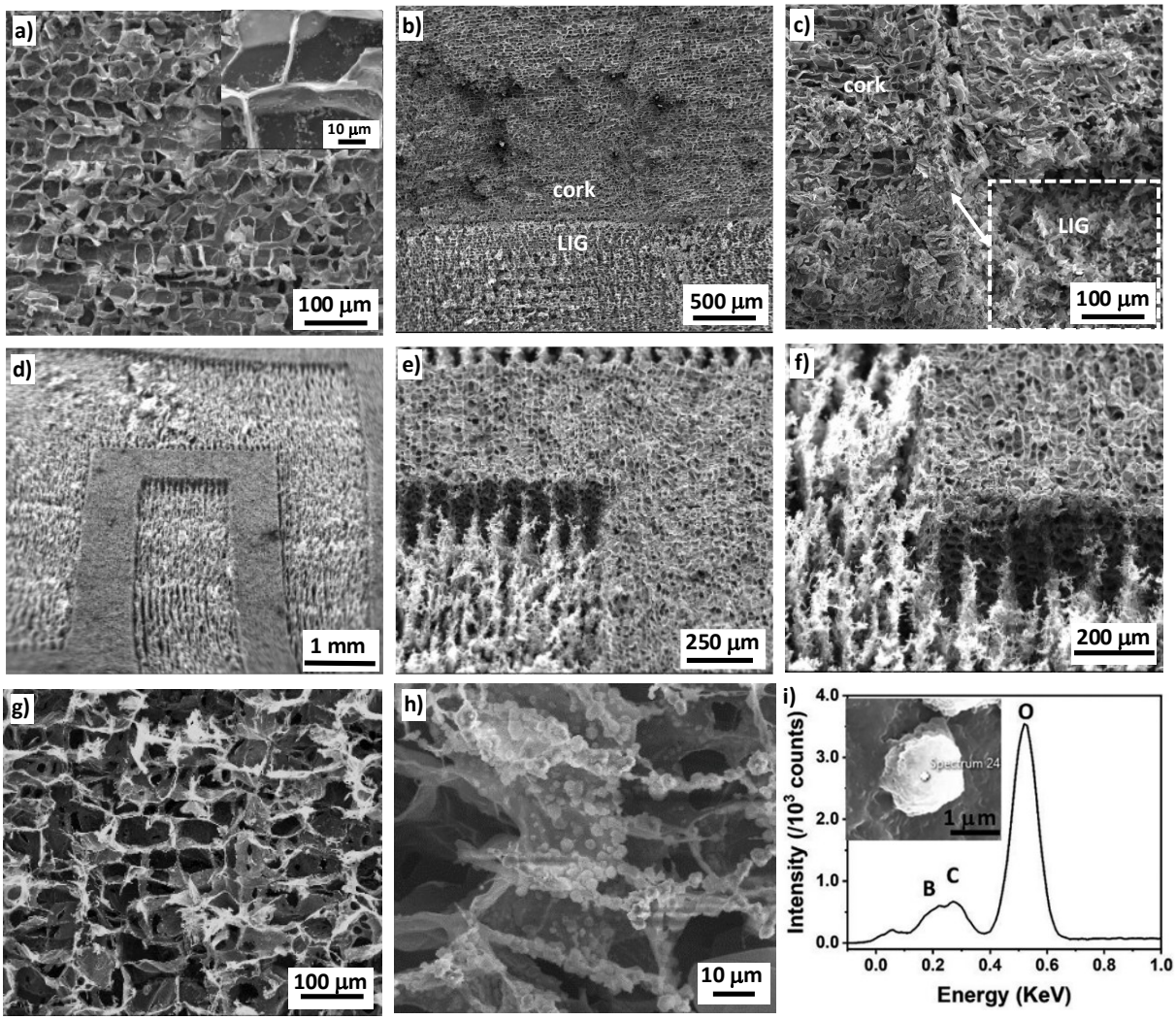

Figure 3.2 SEM images showing the process of laser graphitization on cork: **(a)** image of the cork surface prior graphitization. Inset: high- magnification image of the pristine cork structure; **(b)** low-magnification image showing graphitized and ungraphitized areas following direct laser writing with a 450 nm laser; **(c)** SEM image (stage tilted at 45°) showing a recessed graphitized LIG structure; Different magnification cross-section SEM images of LIG areas obtained at **(d)** low magnification image; **(e-f)** medium magnification images, **(g)** High-magnification SEM image of the LIG graphitized area, **(h)** SEM image of the LIG-boron graphitized area, **(i)** EDS spectrum of the LIG-boron graphitized structure. Inset: Corresponding SEM image of the analyzed region.

Figure 3.2a shows the top SEM view of a pristine cork stopper displaying a 3D structure of thin wall cells regularly arranged in an alveolar structure, analogous to that of a honeycomb. The

cork cells appeared as 4−9-sided polygons with three cell walls meeting at each vertex of the network. In agreement with the literature, individual prismatic cells were stacked in rows parallel to the radial direction, and lateral cell faces displayed various degrees of corrugation, as a result of compression during the cell and bark growth.[23] A close-up higher- magnification SEM image (figure 3.2a, inset) shows details of the alveolar closed cell units, displaying a corrugated, closed, and hollow morphology. Following laser graphitization, an extended rougher structure emerged, as shown in the low- magnification SEM image of figure 3.2b, showing a clear demarcation between the graphitized and non-graphitized areas of the cork stopper. Similar demarcation was also visible in the tilted SEM image of figure 3.2c showing the occurrence of partial ablation and the formation of graphitized areas ca. 184 μm below the level of the cork surface which is more evident from figure 3.2 d-f. Close observation of the LIG area (figure 3.2g) showed that the original cork ordered honeycomb structure was maintained in the graphitized structure, but a higher degree of disorder emerged overall, as cell walls appeared "exploded" and displayed a high density of defects, microholes, and micro-flakes. Figure 3.2h shows the SEM top view of LIG structures obtained after laser writing of cork surfaces pretreated with H_3BO_3. Laser illumination likely promoted dehydration of deposited boron salts resulting in formation of spherical crystals with diameters between 1 and 10 μm, uniformly covering the surface of the engraved cork microstructure. The SEM EDS spectrum shown in figure 3.2i, recorded across one of the boron microcrystals, confirmed the presence of carbon, boron, and oxygen on the graphitized cork structure.

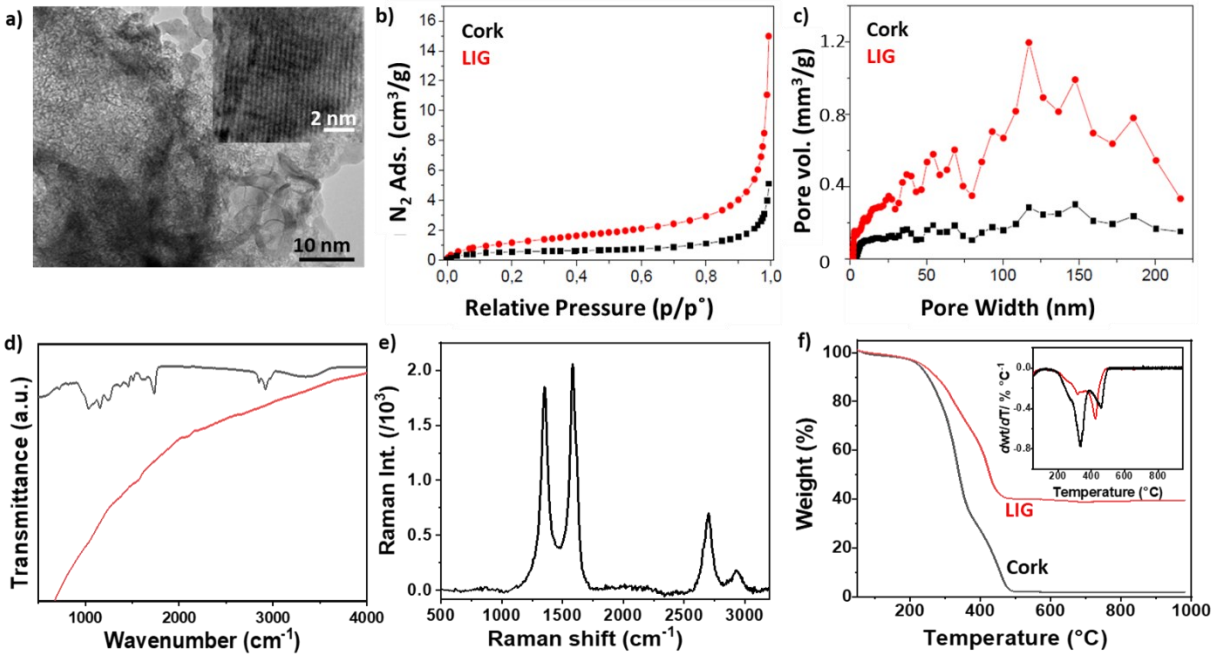

Figure 3.3 (a) TEM image of LIG; (b) FTIR spectra of pristine cork (black curve) and cork graphitized area (red curve); (c) Raman spectrum of LIG; (d) TGA curves of pristine cork (black) and LIG (red). Inset DTGA curves of pristine cork (black) and LIG (red).

Figure 3.3a shows a TEM image of LIG structures displaying nanoscale edges, ripples, and wrinkles resulting in an increased accessible surface area, which is therefore promising for high- performance electrochemical applications. The formed LIG exhibited a crystalline structure (inset of figure 3.3a) with d- spacing of 3.5 Å, corresponding to the distance between two neighbouring (002) planes in graphitic materials, close to the average lattice space of 3.4 Å found for LIG structures obtained from graphitization of polyimide and wood materials.[27,34] Further evidence of the LIG increased surface area compared to pristine cork is given by the results of the Brunauer−Emmett−Teller (BET) in figure 3.3b analysis showing a 2.5 times increase in the specific surface area, from 1.8 ± 0.079 m^2/g (cork) to 4.6 ± 0.026 m^2/g (LIG) and a 3 times increase in pore volume, from 0.00774 cm^3/g (cork) to 0.02281 cm^3/g (LIG). Indeed, the pristine cork sample shows very low N_2 adsorption, presenting just a steep rise at high relative pressure, due to nitrogen condensation. Instead, LIG shows a higher N_2 isotherm in all the ranges of adsorption, indicating a more porous sample, and particularly the significant

presence of mesoporosity (see figure 3.3c). This result is in accordance with the evidence of an expanded structure revealed by morphological analyses. Contact angle measurements were also performed, and they showed a decrease in hydrophobicity from a 102.7° for pristine cork to 80.9° for graphitic carbon areas. The cork graphitization process was also investigated by spectroscopic techniques. Figure 3.3d shows a comparison between the FTIR spectrum of pristine cork (black line) and the graphitic carbon structure (red line) obtained after the laser writing process. A typical FTIR spectrum of pristine cork showed the presence of well-defined peaks that were associated with the presence of suberin (2920, 2851, and 1739 cm^{-1}), guaiacyl-type lignin (1510, 853, and 820 cm^{-1}), polysaccharides (1099 and 1037 cm^{-1}), and extractives (1607 and 1460− 1300 cm^{-1}), as reported in the literature.[36] After the laser engraving process, the FTIR spectrum appeared featureless, thus confirming the conversion of cork into graphitic carbon. The Raman spectrum (figure 3.3e) displayed evidence of graphene-like carbon morphology structure formation. Specifically, the spectrum was characterized by a D band centered at 1352 cm^{-1} induced by bent sp^2 carbon bonds and associated with the presence of defects, a G band centered at 1587 cm^{-1} and corresponding to the E_{2g} tangential vibrations of graphitic carbon, and a 2D band at 2696 cm^{-1} originating from second- order zone boundary phonons indicating conversion from of amorphous carbon to crystalline graphitic carbon. All bands could be fitted by a single Lorentzian peak with a full-width-at- half-maximum (FWHM) of 73.1, 65.9, and 73.4 cm^{-1} for the D, G, and 2D bands, respectively. This profile was consistent with the profile of LIG structures fabricated by our group and others by infrared and visible laser writing of polyimide sheets.[27–29] In particular, the ratio $I_D/I_G \approx 1$ confirmed the crystalline nature of the ablated surface and was in agreement with formation of highly ordered graphite and nanocrystalline graphitic domains in a disordered carbon matrix; the low I_{2D}/ I_G ratio of 0.37 suggested that the laser-induced graphitization process resulted in the formation of nanocrystalline graphitic carbon films, whereas the presence of a sharp 2D peak provided

further evidence for a higher degree of ordering, consisting of randomly stacked graphene layers along the c axis.[27] Figure 3.3f shows the thermal stability of the pristine cork material, evaluated by TGA analysis. The mass change before 210 °C was associated with moisture release. The cork material was stable up to ca. 200 °C. A substantial weight loss occurred between 200 and 400 °C, probably associated with intra- and intermolecular dehydration processes and specifically in decomposition of the hemi-cellulose structure in the range 290−380 °C leading to formation of aliphatic char. The peak visible at 456 °C s associated with the joint degradation of lignin and suberin and the generation of a condensed polycyclic aromatic structure, which was converted to graphitic carbon at higher temperature.[35,37] The two degradation events were clearly visible in the derivative (D)TGA curves shown as inset of figure 3.3f. A small stable graphitic material residue (ca. 2%) remained at temperatures >900 °C, confirming the suppression of complete degradation of the cork material. In comparison, the TGA of LIG material displayed higher temperature stability, with 40% of the material stable at 900 °C. The degradation event clearly visible in the DTGA curve was attributed to degradation of residual lignin and suberin still present in the LIG mechanically removed from the cork substrate. The graphitization of natural materials such wood and lignin-rich materials has been ascribed to a combination between the laser photothermal effect and the unique chemical composition/morphological structure of the materials.[34] The cork graphitization process does not seem to be dependent on the laser wavelength as we were also able to produce LIG by CO_2 irradiation, whereas Chen et al. reported graphitization with UV irradiation.[38] Compared to wood, cork has a similar content of lignin (22 wt %) and a low content of cellulose (9% wt).[27] Furthermore, cork has a rich cellular wall structure consisting of a thin, lignin-rich middle lamella, a thick secondary wall made from alternating hydrophobic suberin and wax lamella and a thin tertiary wall of polysaccharides.[22] Suberin is the most abundant (approximately 40%) of the cell wall components, and it is the major contributor to cork's well-

known resistance to air and water and acids. We speculate that the combination of **(i)** the cork's three-dimensional and heavily cross-linked structure and **(ii)** the hydrophobic nature of most of the cork's structural components might have contributed to the regulation of the local laser high temperature and promoted graphitization while preventing carbonization. Interestingly, suberin consists of a polyester structure composed of long-chain fatty acids, hydroxy fatty and rich in phenolic acids, linked by ester groups. Recently, it has been reported that phenolic resins could be graphitized by 450 nm laser irradiation with better results compared to IR irradiation (better fine-tuning of the conversion process leading to better electrical conductivity and mechanical stability).[39]

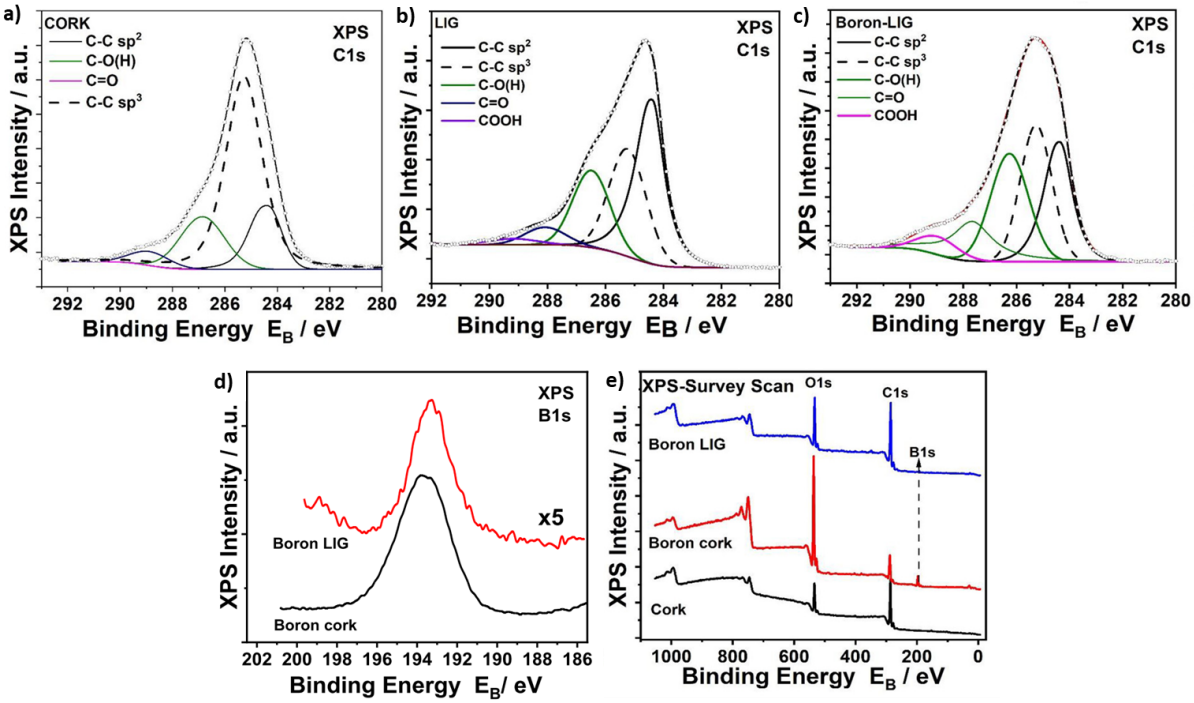

Figure 3.4. XPS spectra of deconvoluted C1s peaks of (a) pristine cork, (b) LIG, and (c) boron-doped LIG; (d) XPS spectra of deconvoluted B1s peaks of Boron cork and Boron LIG, (e) XPS survey scans of cork (black line), boron-doped cork (red line), and boron-doped LIG (blue line).

Further analysis was also carried out to elucidate the process of cork graphitization and the effect of boron doping. Figure 3.4a–c shows the deconvoluted C 1s XPS peaks for pristine cork, LIG, and LIG obtained from boron-doped cork substrates. The peaks were analysed based on five components (the main C=C sp^2 and C–C sp^3 carbon bonds, C–O(H) epoxides and

hydroxides, C=O carbonyl groups, and COOH carboxyl groups). Peak assignments and percentage component concentrations are shown in Table 3.2. XPS data showed an increase in the concentration of sp^2 carbon, from 14.6% of pristine cork to 41.2% of graphitized cork, as well as a decrease in C sp^3 percentage in graphitized cork, further confirming the graphene-like nature of the obtained structure. Also confirmed was the presence of surface carboxyl and carbonyl groups with the C−O peak more dominant than C=O and COOH peaks (21.3% vs 5.4 and 2.2%, respectively).

Table 3.2 Percentage of C−C sp^2, C−C sp^3, Epoxides-Hydroxides, Carbonyls, and Carboxyl bonding as derived from C 1s XPS spectrum deconvolution[a]

Atomic percentages (%)				
Cork	**Boron cork**	**LIG**	**Boron-LIG**	**Peak assignments**
14.6	16.6	41.2	24.7	C-C sp^2
64	34	29.9	29.3	C-C sp^3
17.3	27	21.3	27.7	C-O(H)
0	13	5.4	13	C=O
4.1	9	2.2	5.4	COOH
80.3	31.2	84.7	73.9	Total C
19.7	46.9	15.3	21.7	Total O
N/A	21.9	N/A	4.4	Total B

[a]The atomic % concentration pf carbon, oxygen, and boron is also presented for all analysed materials.

The atomic % concentration of carbon and oxygen is also presented in Table 3.2, and it shows an increased C percentage and decreased O percentage in the transition from pristine cork to graphitic carbon, following a trend already observed for other graphitic carbon materials

derived from polyimide laser writing processes. XPS analysis was also performed on boron-LIG samples to get insights into the nature of boron-doping. C 1s XPS peaks of boron-doped LIG (figure 3.4c) showed an increase in C−Csp^2 compared to pristine cork and a decrease in sp^3 C−C, following a trend analogous to that displayed by undoped LIG materials. The deconvoluted boron XPS peak is shown in figure 3.4d. After laser irradiation, the boron peak slightly shifted to a higher binding energy (193.7 eV); a 4.4% atomic percentage of boron was found in the boron cork-LIG sample, suggesting that a high content of boron was incorporated in the LIG networks. Figure 3.4e shows the XPS survey scans for pristine cork, boron cork, and boron cork-LIG. Boron peaks appeared at 193.3 eV in the boron cork sample, corresponding to an atomic percentage of 21.9%. Table 3.2 shows that the atomic percentage of carbon and oxygen changed in different cork samples upon laser irradiation. Interestingly, the oxygen atomic percentage increased from 19.7 for pristine cork to 21.7 for boron cork-LIG, indicating the formation of new oxygen-containing groups in doped samples. These characteristics are consistent with those reported for boron-doped graphene-like carbon materials whereby boron entered the carbon lattice at the trigonal sites, acting as an electron acceptor, causing a shift in the Fermi level to the conduction band and hence modifying the electronic structure of boron-doped carbon. The redistribution of π electrons induced by the presence of substitutional boron strengthened C−O bonds upon oxygen adsorption resulting in higher oxygen concentrations in the boron-doped samples.[40,41] The sheet resistance of the graphitic carbon structures measured by a TLM method was calculated to be 46 ± 3 and 38 ± 2 Ω/sq for LIG and boron-LIG, respectively, while the bare cork showed no conductivity, as expected from an insulating material.

Table 3.3 compares the quality of LIG material obtained by graphitization of lignin-rich substrates. The sheet resistance (R_{sh}) reported above was comparable or lower than the resistance calculated for most fabricated structures and lower than the R_{sh} reported for cork graphitized with UV laser. The Raman characteristics were comparable to those reported for watercolour and chromatography papers.

Table 3.3 Comparison of LIG Characteristics Obtained from Lignin-Based Materials

Material	**Laser type/ Wavelength**	**Raman (D/G)**	**Raman (2D/G)**	**R_{sh} (Ω/sq)**	**Ref.**
Paper	UV (355 nm)			125	[42]
Wood	IR (10.6 µm)	0.8	0.5	10	[34]
Watercolour paper	IR	1		40	[43]
Chromatography paper	IR	0.5		32	[44]
Chromatography paper	IR	1.28	0.62	56	[45]
Cellulose nanofibers	IR			16000	[35]
Cork	UV	0.41	0.37	75	[46]
Cork	Visible (450 nm)	1	0.37	46	Our work

3.4.2 Electrochemical Characterisation

The supercapacitive behaviour of fabricated devices was electrochemically tested in both open planar configuration (interdigitated electrodes) and sandwich (square electrode) configurations using PVA/H_2SO_4 as an electrolyte.

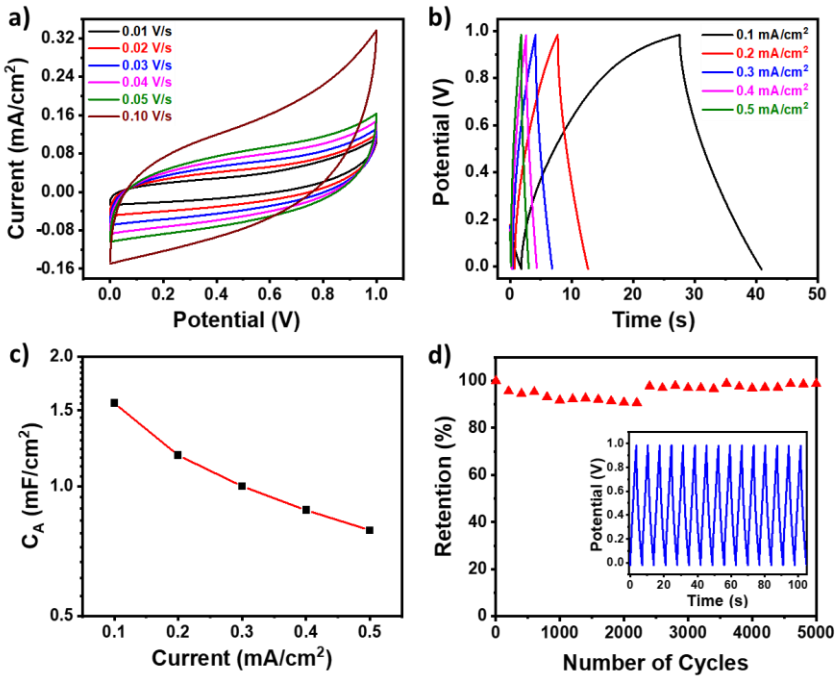

Figure 3.5 Electrochemical characterization of a representative open interdigitated LIG supercapacitor device (a) cyclic voltammograms at different scan rates (from 0.01 to 0.10 V/s); (b) galvanostatic charge discharge (GCD) curves at different current densities; (c) plot of areal capacitance (C_A) at different current densities (d) cyclability testing over 5000 cycles. Insets: representative GCD curves recorded during cycling.

Cyclic voltammetry (CV) and galvanostatic charge−discharge measurements were used to investigate the device's electrochemical behaviour. Figure 3.5a shows CV curves collected in the 0.01−0.1 V/s scan rate interval for the planar configuration. All curves showed a pseudo-rectangular shape commonly associated with a good capacitive behaviour.[25] Figure 3.5b shows the galvanostatic charge discharge (GCD) curves of a representative device collected in the 0.1−0.5 mA/cm^2 interval. All curves displayed a nearly triangular shape, another indication of good capacitive behaviour. [30–32] The areal capacitance, C_A, calculated from the discharge

curves of the GCD measurements at 0.1 mA/cm^2 was found to be 1.56 mF/cm^2. The C_A showed a decrease with the increase of current density, as displayed in figure 3.5c. The stability over time of the interdigitated graphitic carbon electrodes was tested over 5000 cycles of charge−discharge (figure 3.5d) recorded at a current density 0.1 mA/cm^2. It was found that the device retained 99.7% of its original capacitance and showed an average capacitance of 1.64 ± 0.03 mF/cm^2. Inset of figure 3.5d shows representative galvanostatic CD curves recorded during the 5000 cycles of charge−discharge.

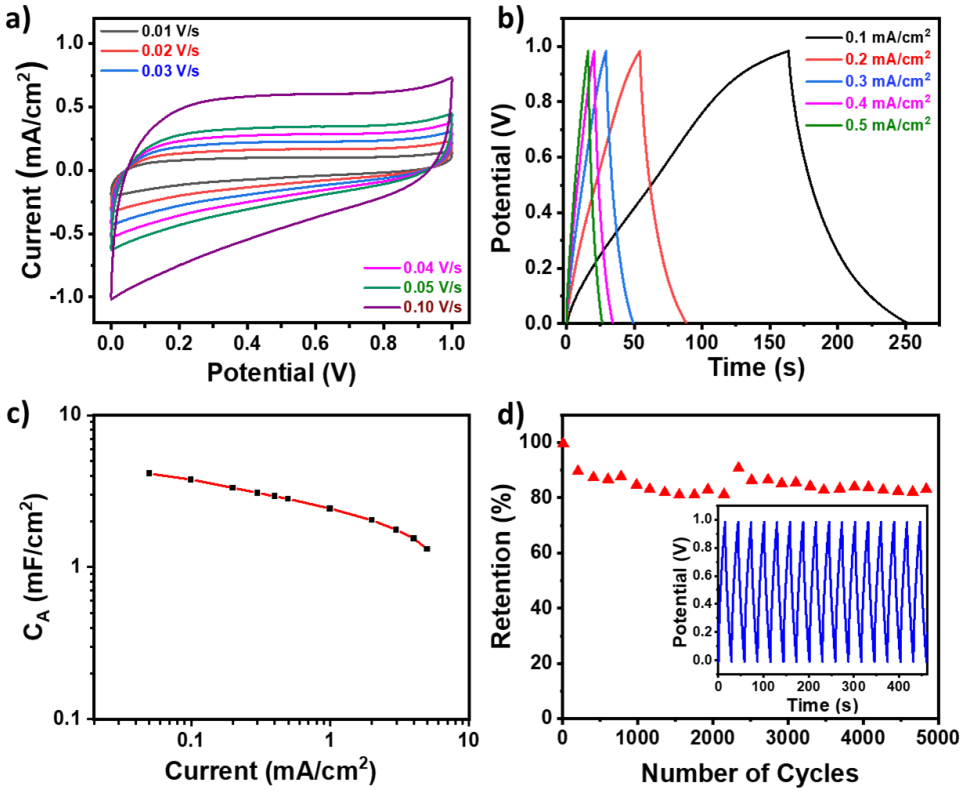

Figure 3.6 Electrochemical characterization of a representative Sandwich LIG supercapacitor device (a) cyclic voltammograms at different scan rates (from 0.01 to 0.10 V/s); (b) GCD curves at different current densities; (c) plot of areal capacitance (C_A) at different current densities (d) cyclability testing over 5000 cycles. Insets: representative GCD curves recorded during cycling.

Figure 3.6 shows data associated with the electrochemical characterization of sandwich configuration supercapacitor devices. The CV curves (figure 3.6a) collected in the 0.01− 0.1 V/s scan rate interval showed a pseudo-rectangular shape, while the galvanostatic charge

discharge (GCD) curves (figure 3.6b) recorded in the 0.1−0.5 mA/cm^2 interval showed a nearly triangular shape, both indicative of good super-capacitive behaviour. The C_A calculated from the GCD curves at different current density values showed the highest capacitance equal to 4.13 mF/cm^2 at a current density of 0.05 mA/cm^2 (figure 3.6c). The stability over time of the sandwich LIG electrodes was tested over 5000 cycles of charge−discharge (figure 3.6d) at a current density of 1.0 mA/cm^2, and it was found that the device retained 83.3% of its original capacitance.

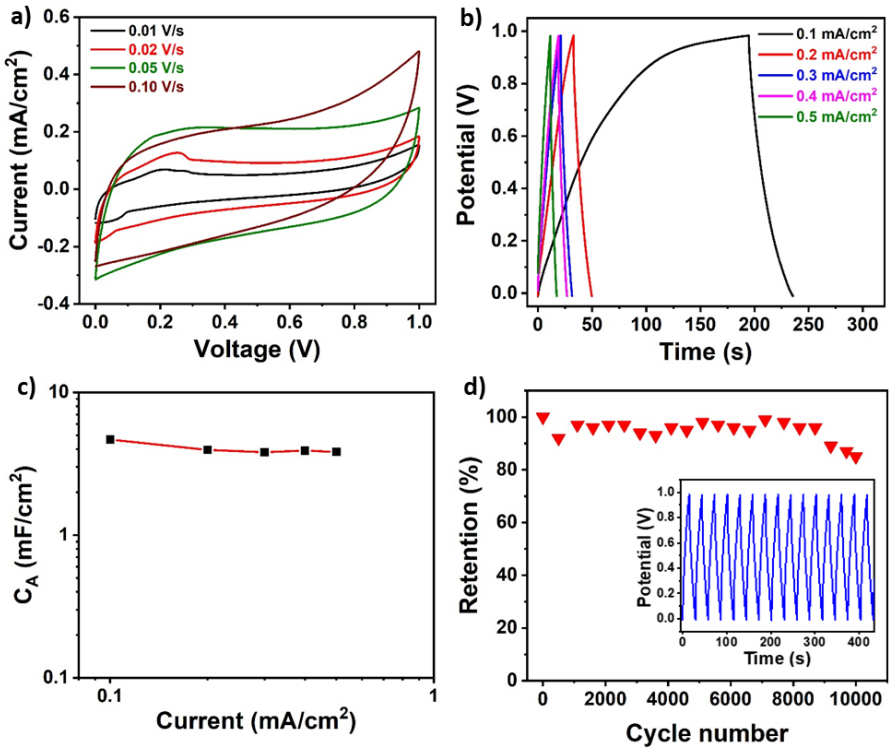

Figure 3.7 Electrochemical characterization of Boron-doped interdigitated LIG supercapacitor device (a) cyclic voltammograms at different scan rates (from 0.01 to 0.10 V/s); (b) GCD curves at different current densities; (c) plot of areal capacitance (C_A) at different current densities (d) cyclability testing over 10000 cycles. Insets: representative GCD curves recorded during cycling.

To improve the electrochemical performance, LIG electrodes in both configurations were doped with boron by immersion of the cork substrate into an aqueous solution of H_3BO_3 prior laser irradiation. Figure 3.7 reports the electrochemical characterization of the resulting boron-doped interdigitated devices. CV curves acquired between 0.01 and 0.1 V/s scan rates showed

the typical super-capacitive pseudo-rectangular shapes (see figure 3.7a) and the galvanostatic charge discharge (GCD) curves showed pseudo-triangular shapes (figure 3.7b). Furthermore, the C_A, calculated from the CC curves across two orders of magnitude current densities range, showed a little decrease with the increase of the current densities, analogous to the behaviour previously observed for no-doped devices. A maximum C_A of 4.67 mF/ cm^2 at 0.1 mA/cm^2 was calculated for the open interdigitated configuration (figure 3.7c). Finally, the stability over time of the boron-doped interdigitated super- capacitor was assessed over 10 000 cycles of galvanostatic charge−discharge at 0.1 mA/cm^2 and showed excellent stability over time with a recorded 15% loss in retention for the interdigitated configuration (figure 3.7d).

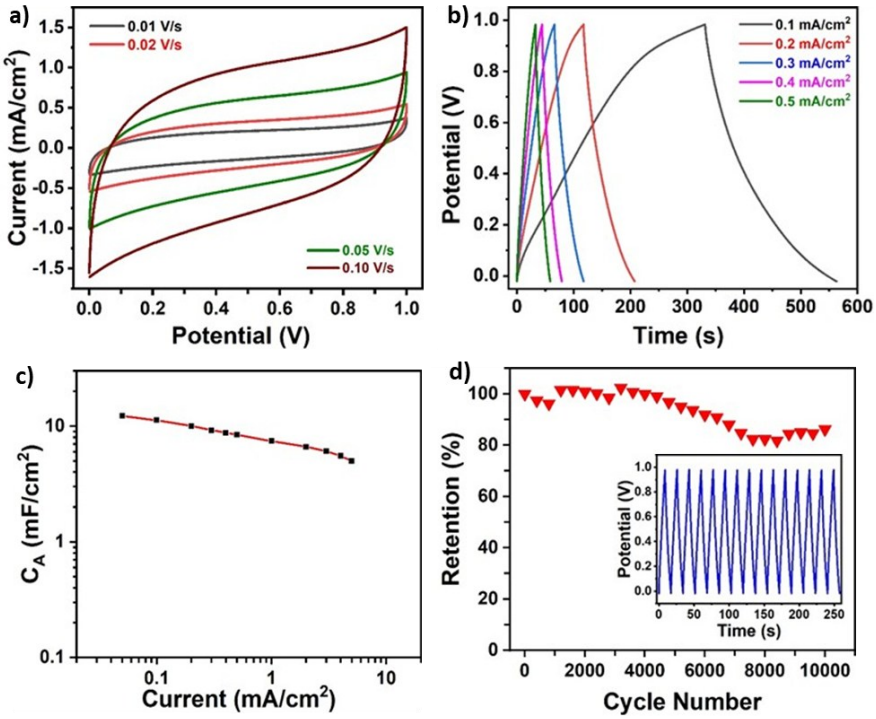

Figure 3.8 Electrochemical characterization of Boron-doped sandwich LIG supercapacitor device (a) cyclic voltammograms at different scan rates (from 0.01 to 0.10 V/s); (b) GCD curves at different current densities; (c) plot of areal capacitance (C_A) at different current densities (d) cyclability testing over 10000 cycles. Insets: representative GCD curves recorded during cycling.

Figure 3.8 presents the electrochemical characterization of boron-doped sandwich supercapacitors. The CV curves recorded at scan rates between 0.01 and 0.1 V/s exhibited a

pseudo-rectangular shape (figure 3.8a), characteristic of supercapacitive behaviour, similar to that observed for boron-doped interdigitated devices. The GCD curves at varying current densities displayed pseudo-triangular profiles (figure 3.8b), further confirming capacitive charge storage. The areal capacitance (C_A), calculated from the GCD curves across two orders of magnitude of current densities, showed a slight decrease with increasing current density. A maximum areal capacitance of 11.24 mF/cm² was achieved at 0.1 mA/cm² (figure 3.8c), which is 2.4−3 times higher than that of non-doped cork-based devices. The long-term stability of the boron-doped sandwich supercapacitor was evaluated over 10,000 charge-discharge cycles at 1.0 mA/cm², revealing a 14% capacitance loss, demonstrating excellent cycling stability (figure 3.8d).

The better performance of boron-doped devices was ascribed to the catalytic effect of the low-concentration boron doping where boron doped sandwiched device showed a maximum areal energy density of 1.7 μWh cm^{-2} and power density of 55.7 μWcm^{-2} at a discharge rate of 0.05 mA/cm^2. As observed in the XPS analysis, boron-doped LIG materials displayed a higher oxygen atomic percentage, which resulted in a higher redox capacitance. In parallel, it has been reported that boron doping can induce hole charge carriers in the graphene lattice, resulting in an increase of the charge density and hence the electrons' charge storage.[40,41] The results reported were comparable to the performance shown for other "natural" supercapacitor devices. For example, supercapacitors based on jute fibers have shown a specific capacitance of 8.65 mF.cm^{-1} at 0.1 mA.[47] On the other hand, LIG supercapacitors recently fabricated by femtolaser graphitization of fallen leaves showed a CA of 34.68 mF cm^{-2} at 5 mV s^{-1}.[48]

3.5 Conclusions

In conclusion, novel LIG supercapacitors were fabricated by using cork-based devices in both open and sandwich configurations. An easy, one-step laser engraving process, carried out in minutes with visible irradiation wavelength and under ambient conditions, was used for the two-electrode fabrication, leading to the formation of highly 3D, porous, and electrically conductive LIG structures. Best performances were obtained upon boron treatment of the cork substrates prior to laser graphitization, a process that resulted in boron doping of the resulting LIG electrodes and an increase of ca. three times in the specific areal capacitance compared to non-doped devices. The cork-based supercapacitors also displayed good stability over time, with no significant loss over 10,000 cycles of charge−discharge. The laser-induced graphitic carbon electrodes obtained by laser engraving of earth-abundant and low-cost renewable sources such as cork constitute promising candidates for the realization of next-generation low-carbon-footprint and low-cost energy storage devices.

3.6 References

[1] X. Guo et al., "Nanostructured graphene-based materials for flexible energy storage," Energy Storage Mater., vol. 9, pp. 150–169, 2017, doi: https://doi.org/10.1016/j.ensm.2017.07.006.

[2] B. Wang et al., "Graphene-based composites for electrochemical energy storage," Energy Storage Mater., vol. 24, pp. 22–51, 2020, doi: https://doi.org/10.1016/j.ensm.2019.08.004.

[3] W. K. Chee, H. N. Lim, Z. Zainal, N. M. Huang, I. Harrison, and Y. Andou, "Flexible Graphene-Based Supercapacitors: A Review," J. Phys. Chem. C, vol. 120, no. 8, pp. 4153–4172, Mar. 2016, doi: 10.1021/acs.jpcc.5b10187.

[4] H. J. Salavagione et al., "Identification of high performance solvents for the sustainable processing of graphene," Green Chem., vol. 19, no. 11, pp. 2550–2560, 2017, doi: 10.1039/C7GC00112F.

[5] A. R. Kamali, "Eco-friendly production of high quality low cost graphene and its application in lithium ion batteries," Green Chem., vol. 18, no. 7, pp. 1952–1964, 2016, doi: 10.1039/C5GC02455B.

[6] D. Beloin-Saint-Pierre and R. Hischier, "Towards a more environmentally sustainable production of graphene-based materials: Building on current knowledge to offer recommendations," Int. J. Life Cycle Assess., vol. 26, no. 2, pp. 327–343, 2021, doi: 10.1007/s11367-020-01864-z.

[7] B. Ouyang, Y. Zhang, Z. Zhang, H. J. Fan, and R. S. Rawat, "Green synthesis of vertical graphene nanosheets and their application in high-performance supercapacitors," RSC Adv., vol. 6, no. 28, pp. 23968–23973, 2016, doi: 10.1039/C5RA27084G.

[8] W. Chen et al., "Green Synthesis of Graphene Quantum Dots from Cotton Cellulose," ChemistrySelect, vol. 4, no. 10, pp. 2898–2902, 2019, doi: 10.1002/slct.201803512.

[9] S. Pei, Q. Wei, K. Huang, H. M. Cheng, and W. Ren, "Green synthesis of graphene oxide by seconds timescale water electrolytic oxidation," Nat. Commun., vol. 9, no. 1, pp. 1–9, 2018, doi: 10.1038/s41467-017-02479-z.

[10] R. Sha and S. Badhulika, "Facile green synthesis of reduced graphene oxide/tin oxide composite for highly selective and ultra-sensitive detection of ascorbic acid," J.

Electroanal. Chem., vol. 816, pp. 30–37, 2018, doi: https://doi.org/10.1016/j.jelechem.2018.03.033.

[11] G. Bhattacharya, S. Sas, S. Wadhwa, A. Mathur, J. McLaughlin, and S. S. Roy, "Aloe vera assisted facile green synthesis of reduced graphene oxide for electrochemical and dye removal applications," RSC Adv., vol. 7, no. 43, pp. 26680–26688, 2017, doi: 10.1039/C7RA02828H.

[12] T. Li et al., "The synthesis and performance analysis of various biomass-based carbon materials for electric double-layer capacitors: A review," Int. J. Energy Res., vol. 44, no. 4, pp. 2426–2454, 2020, doi: 10.1002/er.5061.

[13] W. Gu and G. Yushin, "Review of nanostructured carbon materials for electrochemical capacitor applications: Advantages and limitations of activated carbon, carbide-derived carbon, zeolite-templated carbon, carbon aerogels, carbon nanotubes, onion-like carbon, and graphene," Wiley Interdiscip. Rev. Energy Environ., vol. 3, no. 5, pp. 424–473, 2014, doi: 10.1002/wene.102.

[14] A. M. Abioye and F. N. Ani, "Recent development in the production of activated carbon electrodes from agricultural waste biomass for supercapacitors: A review," Renew. Sustain. Energy Rev., vol. 52, pp. 1282–1293, 2015, doi: https://doi.org/10.1016/j.rser.2015.07.129.

[15] L. Migliorini et al., "All-Printed Green Micro-Supercapacitors Based on a Natural-derived Ionic Liquid for Flexible Transient Electronics," Adv. Funct. Mater., vol. 31, no. 27, pp. 1–10, 2021, doi: 10.1002/adfm.202102180.

[16] D. Momodu et al., "Enhanced electrochemical response of activated carbon nanostructures from tree-bark biomass waste in polymer-gel active electrolytes," RSC Adv., vol. 7, no. 59, pp. 37286–37295, 2017, doi: 10.1039/C7RA05810A.

[17] C. Chen et al., "All-wood, low tortuosity, aqueous, biodegradable supercapacitors with ultra-high capacitance," Energy Environ. Sci., vol. 10, no. 2, pp. 538–545, 2017, doi: 10.1039/C6EE03716J.

[18] K. S. Sulaiman, A. Mat, and A. K. Arof, "Activated carbon from coconut leaves for electrical double-layer capacitor," Ionics (Kiel)., vol. 22, no. 6, pp. 911–918, 2016, doi: 10.1007/s11581-015-1594-9.

[19] X. Li et al., “Preparation of capacitor’s electrode from sunflower seed shell,” Bioresour. Technol., vol. 102, no. 2, pp. 1118–1123, 2011, doi: https://doi.org/10.1016/j.biortech.2010.08.110.

[20] F. Barzegar et al., “Cycling and floating performance of symmetric supercapacitor derived from coconut shell biomass,” AIP Adv., vol. 6, no. 11, 2016, doi: 10.1063/1.4967348.

[21] J. Xu et al., “Preparing two-dimensional microporous carbon from Pistachio nutshell with high areal capacitance as supercapacitor materials,” Sci. Rep., vol. 4, no. 1, p. 5545, 2014, doi: 10.1038/srep05545.

[22] S. P Silva, M. A Sabino, E. M Fernandes, V. M Correlo, L. F Boesel, and R. L Reis, “Cork: properties, capabilities and applications,” Int. Mater. Rev., vol. 50, no. 6, pp. 345–365, Dec. 2005, doi: 10.1179/174328005X41168.

[23] S. Karade, M. Irle, and K. Maher, “Challenges of Concrete Construction: Volume 5, Sustainable Concrete Construction,” Challenges Concr. Constr. Vol. 5, Sustain. Concr. Constr., no. March 2014, 2002, doi: 10.1680/scc.31777.

[24] F. O. Ochai-Ejeh et al., “High electrochemical performance of hierarchical porous activated carbon derived from lightweight cork (Quercus suber),” J. Mater. Sci., vol. 52, no. 17, pp. 10600–10613, 2017, doi: 10.1007/s10853-017-1205-4.

[25] F. O. Ochai-Ejeh, M. J. Madito, D. Y. Momodu, A. A. Khaleed, O. Olaniyan, and N. Manyala, “High performance hybrid supercapacitor device based on cobalt manganese layered double hydroxide and activated carbon derived from cork (Quercus Suber),” Electrochim. Acta, vol. 252, pp. 41–54, 2017, doi: https://doi.org/10.1016/j.electacta.2017.08.163.

[26] M. Irimia-Vladu, “‘Green’ electronics: biodegradable and biocompatible materials and devices for sustainable future,” Chem. Soc. Rev., vol. 43, no. 2, pp. 588–610, 2014, doi: 10.1039/C3CS60235D.

[27] J. Lin et al., “Laser-induced porous graphene films from commercial polymers,” Nat. Commun., vol. 5, no. 1, p. 5714, 2014, doi: 10.1038/ncomms6714.

[28] R. Ye, D. K. James, and J. M. Tour, “Laser-Induced Graphene,” Acc. Chem. Res., vol. 51, no. 7, pp. 1609–1620, Jul. 2018, doi: 10.1021/acs.accounts.8b00084.

[29] M. Burke et al., “Fabrication and Electrochemical Properties of Three-Dimensional (3D) Porous Graphitic and Graphenelike Electrodes Obtained by Low-Cost Direct Laser Writing Methods,” ACS Omega, vol. 5, no. 3, pp. 1540–1548, 2020, doi: 10.1021/acsomega.9b03418.

[30] L. Li et al., “High-Performance Pseudocapacitive Microsupercapacitors from Laser-Induced Graphene,” Adv. Mater., vol. 28, no. 5, pp. 838–845, 2016, doi: 10.1002/adma.201503333.

[31] Z. Peng, J. Lin, R. Ye, E. L. G. Samuel, and J. M. Tour, “Flexible and stackable laser-induced graphene supercapacitors,” ACS Appl. Mater. Interfaces, vol. 7, no. 5, pp. 3414–3419, Feb. 2015, doi: 10.1021/am509065d.

[32] Z. Peng et al., “Flexible Boron-Doped Laser-Induced Graphene Microsupercapacitors,” ACS Nano, vol. 9, no. 6, pp. 5868–5875, Jun. 2015, doi: 10.1021/acsnano.5b00436.

[33] Y. Chyan, R. Ye, Y. Li, S. P. Singh, C. J. Arnusch, and J. M. Tour, “Laser-Induced Graphene by Multiple Lasing: Toward Electronics on Cloth, Paper, and Food,” ACS Nano, vol. 12, no. 3, pp. 2176–2183, 2018, doi: 10.1021/acsnano.7b08539.

[34] R. Ye et al., “Laser-Induced Graphene Formation on Wood,” Adv. Mater., vol. 29, no. 37, pp. 1–7, 2017, doi: 10.1002/adma.201702211.

[35] S. Lee and S. Jeon, “Laser-Induced Graphitization of Cellulose Nanofiber Substrates under Ambient Conditions,” ACS Sustain. Chem. Eng., vol. 7, no. 2, pp. 2270–2275, Jan. 2019, doi: 10.1021/acssuschemeng.8b04955.

[36] M. H. Lopes, A. S. Barros, C. Pascoal Neto, D. Rutledge, I. Delgadillo, and A. M. Gil, “Variability of cork from portuguese quercus suber studied by solid-state 13C-NMR and FTIR spectroscopies,” Biopolym. - Biospectroscopy Sect., vol. 62, no. 5, pp. 268–277, 2001, doi: 10.1002/bip.1022.

[37] R. Ferreira et al., “Isolation of suberin from birch outer bark and cork using ionic liquids: A new source of macromonomers,” Ind. Crops Prod., vol. 44, pp. 520–527, 2013, doi: https://doi.org/10.1016/j.indcrop.2012.10.002.

[38] Y. Chen et al., “UV Laser-Induced Polyimide-to-Graphene Conversion: Modeling, Fabrication, and Application,” Small Methods, vol. 3, no. 10, pp. 1–9, 2019, doi: 10.1002/smtd.201900208.

[39] Z. Zhang, M. Song, J. Hao, K. Wu, C. Li, and C. Hu, “Visible light laser-induced graphene from phenolic resin: A new approach for directly writing graphene-based electrochemical devices on various substrates,” Carbon N. Y., vol. 127, pp. 287–296, 2018, doi: https://doi.org/10.1016/j.carbon.2017.11.014.

[40] D.-W. Wang, F. Li, Z.-G. Chen, G. Q. Lu, and H.-M. Cheng, “Synthesis and Electrochemical Property of Boron-Doped Mesoporous Carbon in Supercapacitor,” Chem. Mater., vol. 20, no. 22, pp. 7195–7200, Nov. 2008, doi: 10.1021/cm801729y.

[41] L. Niu et al., “Pyrolytic synthesis of boron-doped graphene and its application as electrode material for supercapacitors,” Electrochim. Acta, vol. 108, pp. 666–673, 2013, doi: https://doi.org/10.1016/j.electacta.2013.07.025.

[42] B. Kulyk et al., “Laser-Induced Graphene from Paper by Ultraviolet Irradiation: Humidity and Temperature Sensors,” Adv. Mater. Technol., vol. 7, no. 7, pp. 1–11, 2022, doi: 10.1002/admt.202101311.

[43] Y. Chyan, J. Cohen, W. Wang, C. Zhang, and J. M. Tour, “Graphene Art,” ACS Appl. Nano Mater., vol. 2, no. 5, pp. 3007–3011, May 2019, doi: 10.1021/acsanm.9b00391.

[44] B. Kulyk et al., “Laser-Induced Graphene from Paper for Mechanical Sensing,” ACS Appl. Mater. Interfaces, vol. 13, no. 8, pp. 10210–10221, 2021, doi: 10.1021/acsami.0c20270.

[45] T. Pinheiro et al., “Laser-Induced Graphene on Paper toward Efficient Fabrication of Flexible, Planar Electrodes for Electrochemical Sensing,” Adv. Mater. Interfaces, vol. 8, no. 22, pp. 1–12, 2021, doi: 10.1002/admi.202101502.

[46] A. F. Carvalho, A. J. S. Fernandes, R. Martins, E. Fortunato, and F. M. Costa, “Laser-Induced Graphene Piezoresistive Sensors Synthesized Directly on Cork Insoles for Gait Analysis,” Adv. Mater. Technol., vol. 5, no. 12, pp. 1–8, 2020, doi: 10.1002/admt.202000630.

[47] L. Manjakkal, F. F. Franco, A. Pullanchiyodan, M. González-Jiménez, and R. Dahiya, “Natural Jute Fibre-Based Supercapacitors and Sensors for Eco-Friendly Energy Autonomous Systems,” Adv. Sustain. Syst., vol. 5, no. 3, 2021, doi: 10.1002/adsu.202000286.

[48] T. D. Le et al., “Green Flexible Graphene–Inorganic-Hybrid Micro-Supercapacitors Made of Fallen Leaves Enabled by Ultrafast Laser Pulses,” Adv. Funct. Mater., vol. 32, no. 20, May 2022, doi: 10.1002/adfm.202107768.

Chapter 4: Eco-friendly Energy Storage and Energy Harvesting Devices Fabricated by Direct Laser Writing of Chitosan-Lignin-Boric Acid Substrates

4.1 Abstract

Novel eco-friendly supercapacitor (SC) and triboelectric nanogenerator (TENG) devices were assembled using Laser Induced Graphene (LIG) electrodes fabricated by direct laser writing of chitosan-lignin-boric acid films. A simple one-step laser irradiation was used to convert the chitosan-based films into 3D, interlinked, and electrically conductive LIG electrode materials. Assembled SCs displayed specific areal capacitances up to 21.4 mF/cm^2 at a current density of 0.05 mA/cm^2 and 68% capacitance retention for > 10000 charge/discharge cycles. When charged by a commercial solar cell, the SC could power an LED light, a calculator, and a hygrometer, showing potential for real applications. Single-electrode TENG (SE-TENG) devices were also assembled using PDMS as dielectric layer. The TENGs displayed open circuit voltage of 13.3 V, a short-circuit current of 1.7 μA, and stability over 10,000 cycles. The TENG could charge commercial SCs of 0.1 μF and 1 μF capacitance in less than 60 s. This work demonstrates the suitability of sustainable materials as feedstock constituents for the generation of LIG electrodes and opens the door to the large-scale production of cost-effective electrode materials for “green” wearable electronic applications.

4.2 Introduction

Wearable sensors have gained much attention in recent decades for their applications in health,[1][2] sport,[3] fitness and wellbeing,[4] enabling the monitoring of biomarkers and the transition from centralized to personal, point-of-care monitoring.[5] The rapid technological development and high demand for such wearable devices requires the urgent development of light weight, flexible and robust power systems. Supercapacitors (SCs) are increasingly used in wearable electronics as alternative to traditional batteries, as they combine light weight and flexibility with high-power density, fast charging/discharging ability, and long cycle life.[6-9] A possible alternative strategy to reduce weight and volume in wearable designs is the incorporation of energy harvesting devices to achieve self-powering capabilities.[10-11] Triboelectric nanogenerators (TENGs) are devices capable of harvesting and converting mechanical energy from various stimuli – solid-solid, liquid-solid, and gas-solid - into electricity, generating high AC voltage through the combined effects of contact electrification and electrostatic induction.[12-15] Due to the low cost of materials involved, simplicity of operation, versatility of configuration and wide range of applications, TENGs are being increasingly considered for wearable power supplies and versatile self-powered sensing applications.[16]

Recently, direct laser writing (DLW) has emerged as a high throughput and ecofriendly manufacturing technique for the realization of energy storage[17-19] and energy harvesting[20-22] devices. In this method, low-cost hobbyist lasers are used to "write" Laser Induced Graphene (LIG) conductive patterns on flexible polymer substrates without the use of templates or chemicals. The obtained LIG structures exhibit high surface area, high density of defects and low sheet resistance (R_{sh} < 50 Ω/sq), making LIG an ideal electrode material for energy applications. For example, the application of DLW methods to commercial polyimide substrates (Kapton tape), has led to the development of micro-supercapacitors with excellent

capacitive behavior and showing areal capacitances up to 16.5 mF/cm^2.[17-19] LIG has also been used in energy harvesting applications. Stanford et al. fabricated LIG-TENGs on polyimide and cork substrates obtaining open-circuit voltages >3.5 kV and peak power >8 mW.[20] Yang et al. used polyimide paper to realize novel foldable and stackable TENGs, also displaying tailorable performance and enhanced versatility.[22] Shrestha et al. developed the first example of a SC power cell (SPC) in which energy generated from a TENG device was stored in a SC without power management or rectifier circuits via a 'tribo-electrochemical mechanism. The self-charging SPC combined TENG and SPC into a single integrated device, with TENG generating 2.5 mW power, which successfully charged a SPC to maximum 210 mV within 9 s.[23]

In parallel to the above technological advances, new efforts are nowadays concentrating into embedding abundant, natural, or renewable constituent materials into energy devices towards development of green wearable technologies with reduced environmental impact. Interestingly, it has been recently demonstrated that natural and abundant precursors can be eggshell feedstock materials for the production of "green" LIG, making this process amenable to the fabrication of biodegradable electronic platforms.[24-26] For example, our group and others have investigated the merit of sustainable paper, lignin-enriched paper, and cork for the production of LIG SC electrodes, reaching impressive areal capacitance (up to 10 mF/cm^2), power (4 μW cm^{-2} at 0.01 mA/cm^2) and energy (≈4 μW/cm^2 and ≈0.77 μWh/cm^2 at 0.01 mA/cm^2) densities.[27-28] Chi et al. have designed a rice-based TENG able to produce 244 V with 6 μA of short circuit current and 37 μW/cm^2 of power density.[29] Saqib et al. have fabricated a TENG from waste peanut shells achieving 910 V open circuit voltage and 104.5 μA short circuit current with 1.3 mW of peak instantaneous power.[30] Singh et al. also has used waste from fish fins as well as other biomaterials combinations (egg shell membrane, dog hairs, tree cotton) to fabricate TENGs, achieving 130 V, with 1.1 μA measured across a 1 MΩ resistor.[31]

In this work “green” LIG electrodes were fabricated by one-step DLW of flexible chitosan-lignin-boric acid films. The electrodes displayed the typical high surface area of LIG materials obtained from conventional polyimide and were used to assemble energy storage and harvesting units. The SCs showed impressive areal capacitance of 15.2 mF/cm^2 at 0.1 mA/cm^2 and good stability and cyclability, with retention of 68% of the initial capacitance after > 10000 charge/discharge cycles. When assembled in series and charged with a commercial solar cell, the SCs were able to power LED lights, a calculator and a chronometer, showing promising real-world application capabilities. Single-electrode TENG devices were also fabricated, which showed open circuit voltages 3.7V–13.3V for 30N–60 N applied forces. The capability of TENGs to charge commercial supercapacitors was also shown, towards demonstration of practical applications.

4.3 Experimental Section

4.3.1 Materials

Chitosan powder (CS, medium molecular weight), glycerol (99.5%), lignin alkali (LIGN, 95% pure), acetic acid (50%), boric acid (BA) powder (H_3BO_3, 99.5%), poly(vinyl alcohol) (PVA, M_w 89,000-98,000), and sulphuric acid (96%) were purchased from Sigma Aldrich. Polydimethylsiloxane (PDMS) base and curing agent at a 10:1 ratio (Dowsil 184 Sylgard) were purchased from Farnell Ireland. All the chemicals were used without further purification or modification. All solutions were prepared using deionized (DI) Milli-Q water (resistivity ~18.2 MΩ/cm).

4.3.2 Preparation of Chitosan-Lignin-Boric acid substrate

Chitosan (2g), glycerol (2mL) and lignin alkali powder (0.3g) were dissolved in 100 mL of an aqueous solution of acetic acid (1%) and stirred for 1 h. Different amounts of BA, equivalent to 1-11% relative to chitosan weight, were added to the solution which was stirred for 24 h. The resulting mixtures were poured on polyethylene terephthalate (PET) sheets in a plastic tray

and dried for 48 hours at room temperature to get a 200 µm thick flexible Chitosan-Lignin-Boric acid (CS-LIGN-BA) film on PET. Scheme 4.1 illustrates the fabrication of CS-LIGN-BA substrates, along with the process of LIG fabrication by one-step visible laser irradiation.

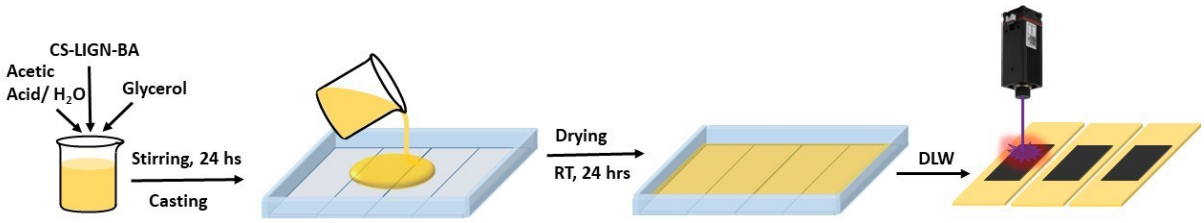

Scheme 4.1 Schematic process for the preparation of CS-LIGN-BA substrates by casting aqueous CS-LIGN solutions with 3-11 wt% of BA into PET substrates, followed by LIG fabrication with DLW.

4.3.3 LIG Fabrication

LIG electrodes were fabricated via laser irradiation using a K5 compact desktop mini laser engraving machine equipped with a 450 nm wavelength laser and a 3 W power source. To ensure stability during laser processing, PET films were secured onto a glass slide using double-sided tape. LIG patterns were laser-written onto CS-LIGN-BA films with optimized laser power and depth settings, determined through a Design of Experiments (DoE) approach using Design Expert 11 software. A randomized parameter set was employed to enhance LIG production efficiency.

4.3.4 Fabrication of energy storage and harvesting devices

For the fabrication of SCs, a sandwich configuration was designed using LIG square (1 cm^2) electrodes. A PVA/H_2SO_4 electrolyte solution was prepared by stirring together 10 mL of de-ionized water with 1 g of PVA and 1 mL of H_2SO_4 at 80°C overnight. A sintered polypropylene separator with a thickness of 100 µm was placed between two LIG electrodes filled with PVA/H^+ electrolyte solution. The outside edges of the LIG electrodes were painted with conductive silver paint to ensure stable electrical connections to the potentiostat. Prior to electrochemical measurements, the SC sandwich device was placed in a tightly screwed

aluminium holder and stored overnight in a vacuum desiccator to remove any excess moisture and ensure electrolyte penetration into the porous electrodes.

SE-TENG devices were fabricated using LIG as electrodes and polydimethylsiloxane (PDMS) as the triboelectric layer. The PDMS layer was prepared by mixing the silicone elastomer precursor with the curing agent (Sylgard 184) in a 10:1 volume ratio. After thoroughly mixing, the PDMS mixture was vacuum degassed for one hour to remove air bubbles. The degassed PDMS was then spin-coated onto a square-shaped LIG surface (3.8 cm^2) maintaining a constant acceleration speed of 200 rpm for 60 s. After deposition the PDMS layer was further vacuum degassed for one hour to ensure uniformity and eliminate any remaining bubbles. The layer was then cured at 80 $^{\circ}C$ for one hour, resulting in an average thickness of approximately 225 μm, as measured with a Mitutoyo external micrometre. To facilitate electrical measurements, copper tape was attached to LIG surface, serving as the connection point for electrical wiring.

4.3.5 Characterization

The electrical conductivity of the fabricated LIG structures was determined through Transfer Line Measurements (TLM). Transfer line structures (16 × 4 mm) were contacted directly using a probe station (Wentworth Laboratories PML 8000) at known separation lengths. Potential-current sweeps (-0.1 to 0.1 V, 10mV step) were recorded using a parameter analyser (Agilent 5270B). Surface morphology and elemental analysis were performed using Scanning Electron Microscopy (SEM) and Energy-dispersive X-ray Spectroscopy (EDS) with a Zeiss Supra 40, equipped with an Oxford X-Max 50 detector, operating at an accelerating voltage of 10 kV. Samples were coated with ~10 nm film of AuPd (90%Au, 10%Pd) prior to imaging. X-ray photoelectron spectroscopy (XPS) measurements were conducted in a vacuum transfer module using a K-Alpha (Thermo Scientific) 180° double-focusing hemispherical analyzer with 128-channel detector and Al Kα micro-focused monochromator with an excitation energy (hν =

1486 eV) and X-ray spot size of 300 μm. The electron energy analyzer operated with a constant pass energy of 50 eV for high-resolution (HR) spectra and 200 eV for survey spectrum. A dwell time of 50 ms was used for HR spectra and 10 ms for survey spectra, along with 10 and 20 scans, respectively. Raman investigation was performed with Horiba-XPlora equipped with a 70 mW 532 nm laser diode. Spectra were acquired at a laser power of 10% and 30 s acquisition time. X-ray diffraction (XRD) measurements were carried out by scanning from 4 to 70° (2θ) with a Shimadzu XRD-6000 X-ray diffractometer at a rate of $1^{\circ}min^{-1}$. Thermogravimetric analysis (TGA) was conducted using a QG50 TG analyzer from TA Instruments (USA) under a nitrogen atmosphere at a flow rate of 40 mL min^{-1}. Samples of 10 mg were placed in platinum crucibles and heated from 25 °C to 800 °C at a rate of 10 °C min^{-1}.

To investigate electrochemical performance of the SC devices, cyclic voltammetry (CV), galvanostatic charge-discharge (GCD) and electrochemical impedance spectroscopic (EIS) measurements were performed with a multichannel (Autolab PGSTAT M204) electrochemical workstation at ambient condition. The specific areal capacitance (C_A) was calculated from GCD curves using the standard equation [27]

$$C_A = \frac{I}{S \times (dV/dt)} \quad \ldots\ldots\ldots\ldots\ldots\ldots \quad (1)$$

Where, I denotes the constant discharge current, S is the total active area of positive and negative electrodes in cm^2 and dV/dt represents the slope of the discharge as obtained from the charge-discharge curve. EIS spectra of all LIG supercapacitor devices were obtained at open circuit potential (OCP) in the range -0.047 to +0.045V, in the frequency range from 10 kHz to 0.01 Hz using an AC amplitude of 10 mV.

Open circuit electrical voltages (V_{OC}) generated from the constructed SE-TENG device were measured by varying the applied mechanical forces (30 – 60 N) and frequencies (2 to 10 Hz). The short-circuit current (I_{SC}) output was measured under varying forces (30 – 60 N) at a fixed frequency of 2 Hz. The TENGs were connected to an external circuit for measurements, and

the data was collected using an oscilloscope (Tektronix TBS1000C). In all cases, the triboelectric layer matched the area of the LIG electrode, and the V_{OC} results were normalized based on the TENG contact volume. Mechanical drive was generated using a custom-made device. The TENG's electrical output stability was evaluated by monitoring V_{OC} over 10000 cycles at 50 N and 2 Hz. Instantaneous power was calculated using $P = V^2R^{-1}$ from the data obtained from voltage measurements in the corresponding load resistance (R). V_{OC} and I_{SC} output under activation at 50 N and 2 Hz across different resistance ranges (0.1 to 200 MΩ) was evaluated. Then, instantaneous power was plotted as a function of time and power density was calculated by dividing the power by the sample contact area. The surface charge density was obtained following the method proposed by Germane, in which the surface charges Q (nC) was determined from the measured current peaks using equation 2:

$$Q = \int i dt \quad \text{..... (2)}$$

where *i* is the instantaneous current (nA) and *dt* is the time differential (s). Integration was done for the highest and lowest peak corresponding to the separation stage.

4.4 Results and discussion

4.4.1 Material optimisation

Laser writing conditions were optimized for LIG production using CS-LIGN-BA substrates with 5% wt. BA, as this concentration was found optimum in previously fabricated LIG electrodes from polyimide substrates.[33-34] DLW was carried out by using a DoE approach, whereby laser power (LP) and laser depth (LD) were systematically changed between 30-80% and 40-80%, respectively, aiming at obtaining LIG materials with the lowest values of sheet resistance (R_{sh}). Figure 4.1a shows the DoE graph where the values of R_{sh} obtained for LIG written with different LP-LD combinations are shown as colour density (blue to green equivalent to low to high). The calculation showed that the LP-LD combination of 30-40 was the minimum required parameter setting for successful conversion of CS-LIGN-BA into LIG.

However, these experimental conditions led to formation of LIG structures showing high average R_{sh} of ~121 Ω/sq. In contrast, the lowest average R_{SH} value (~12 Ω/sq) was found for the LP-LD combination of 80-80. However, LIG structures formed under this experimental condition were highly brittle. Therefore, an LP-LD 55-60 combination was chosen for further study, as the obtained LIG structures showed acceptable low average R_{sh} of 33 Ω/sq while maintaining their flexibility. After optimization of the laser writing parameters, the contribution of BA was investigated, with the purpose of choosing the BA concentration (wt.%) leading to formation of LIG structures with the lowest R_{sh} values. Figure 4.1b shows that the average R_{sh} of LIG decreased as the BA content in the CS-LIGN mixture increased, until reaching a plateau at BA concentrations of 9% and higher.

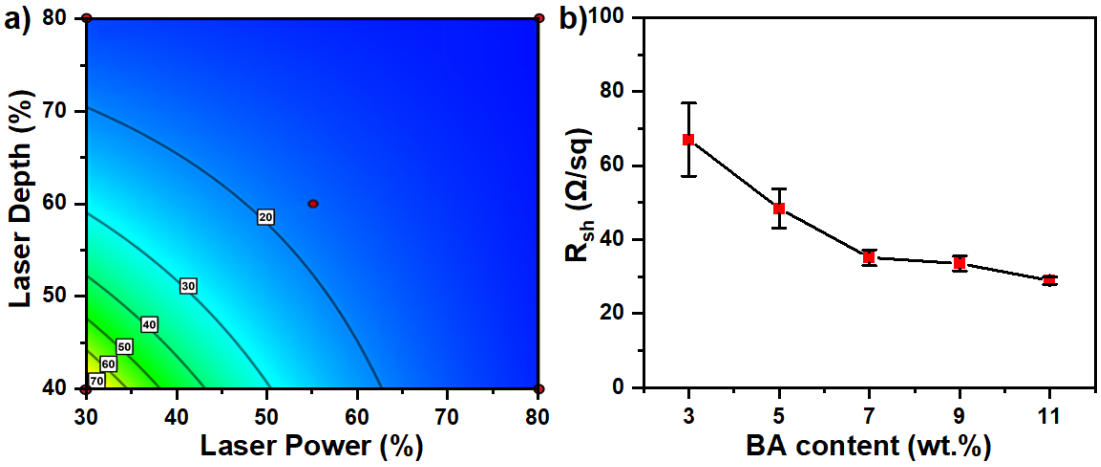

Figure 4.1 a) Response surface design of experiment (DoE-RS) model output for R_{SH} vs. various LP-LD combinations; b) R_{SH} of LIG structures obtained by laser writing (55-60 LP-LD) of CS-LIGN-BA films with different BA contents (wt.%)

Based on this trend, 9% BA was selected for synthesizing subsequent substrates for LIG production, achieving a dry mass loading of CS-LIGN-BA on PET sheet equivalent to 21.36 mg/cm². BA concentrations below 3% were not included, as graphitization did not occur. Furthermore, for BA concentrations above 3%, graphitization was observed even in the absence of LIGN. However, the inclusion of LIGN led to LIG structures of lower R_{sh} values (33 Ω/sq with LIGN vs. 75 Ω/sq without LIGN) and enhanced the overall substrate hydrophobicity,

resulting in SC and TENG devices of greater electrochemical performance and mechanical/chemical stability.

4.4.2 Morphological Characterisation

Figure 4.2 shows SEM images associated with the graphitization of CS-LIGN-BA substrates. The pristine film (figure 4.2a) showed a smooth surface with some residual wrinkles arising from the drying process. The SEM image of LIG (figure 4.2b) illustrates a clear transition from a smooth morphology to a significantly corrugated, elevated morphology upon graphitization and LIG formation. The image showed quite clearly the formation of parallel linear LIG structures about 30 μm wide, associated with the raster scanning movement of the laser during the writing process. The laser written area showed the typical "exploded" LIG morphology, characterized by high density of micro-holes and defects and displaying high surface area and porosity. This morphology resembled closely the morphology of LIG and green-LIG structures previously obtained by laser writing of polyimide and biomaterials, respectively.[26-27, 35] The cross-sectional SEM micrograph revealed an approximate CS-LIGN-BA thickness of ~200 μm (figure 4.2c) and a LIG thickness ranging from 100 to 157 μm (figure 4.2d), consistent with reported values for chitosan-based derivatives.[36] The high LIG thickness played a crucial role in modulating lateral electron pathways and charge-transfer routes, contributing to the observed low sheet resistance (~33 Ω/sq). Figure 4.2e-g shows the SEM-EDS mapping displaying homogeneous distribution of C, O and B in the film. A representative EDS spectrum is shown in figure 4.2h, with atomic percentages of C, O and B equal to 50.0, 42.8 and 7.3 wt%, respectively. Figure 4.2i-k show SEM-EDS mapping and representative EDS spectrum (figure 4.2l) of C, O and B in the LIG materials. Following laser treatment, the C content increased to 82 wt.%, indicating occurrence of graphitization; the O content decreased to 9.3 wt.%, and the B content showed a slight increase (8.7 wt.%), indicating incorporation of boron into the LIG structure.

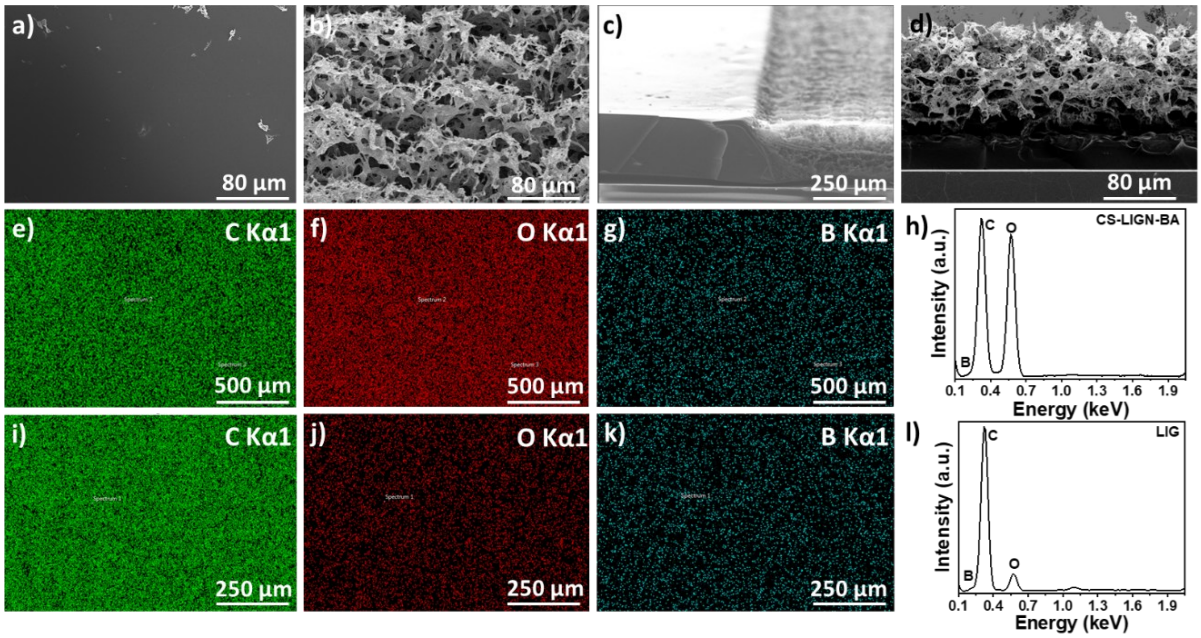

Figure 4.2 SEM images of (a) pristine CS-LIGN-BA substrate; (b) LIG; (c) Cross-sectional SEM image of CS-LIGN-BA and LIG (side by side); (d) LIG. SEM-EDS colour mapping of the CS-LIGN-BA substrate for (e) Carbon, (f) Oxygen, and (g) Boron, with (h) a representative SEM-EDS spectrum of CS-LIGN-BA. SEM-EDS colour mapping of the LIG surface for (i) Carbon, (j) Oxygen, and (k) Boron, with (l) a representative SEM-EDS spectrum of LIG showing atomic distribution.

The SEM-EDS color mapping of CS-LIGN-BA and LIG show a homogeneous atomic distribution of C, O and B throughout the material surface. These preliminary results suggest that BA played a key role in the graphitization process, probably acting as temperature regulator during laser writing, by reducing thermal degradation and ablation and facilitating graphitization.[34] Specifically, it known that CS-BA composites show thermal stability, due to the formation of cross-linked, gel-like structures, a process that releases water preventing ablation during laser irradiation.[34]

4.4.3 Chemical characterization

To evaluate chemical properties of LIG on CS-LIGN-BA composite film, further characterization of LIG was performed using Raman spectroscopy. Figure 4.3a shows a representative Raman spectrum of LIG obtained by laser writing of CS-LIGN-BA substrate displaying three major peaks, typical of graphene-like carbon morphology. Specifically, the

spectrum showed a D-band, related to bent sp^2 carbon and associated with defects, centered at 1351 cm^{-1}, a G-band centered at 1584 cm^{-1}, corresponding to the E_{2g} tangential vibrations of graphitic carbon, and a 2D-band related to second-order zone boundary phonons at 2698 cm^{-1} indicating conversion from of amorphous carbon to crystalline graphitic carbon.[25]

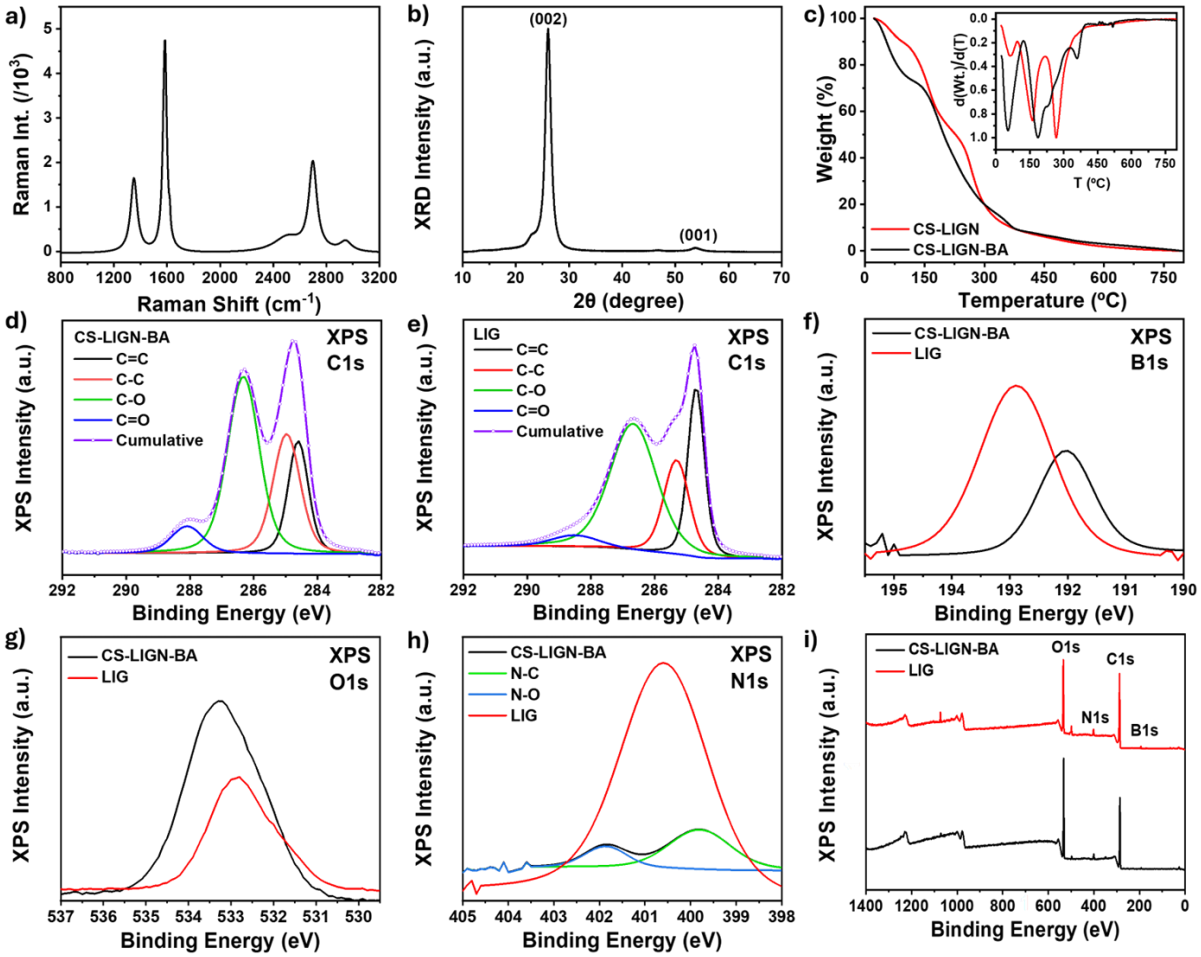

Figure 4.3 (a) Raman spectrum of LIG; (b) XRD pattern of LIG; (c) TGA profiles of CS-LIGN and CS-LIGN-BA substrates; (d) XPS C1s spectra of pristine CS-LIGN-BA films; (e) XPS C1s spectra of LIG; XPS spectra of CS-LIGN-BA and LIG: (f) B1s spectra, (g) O1s spectra, (h) N1s spectra, and (i) XPS survey scan spectra.

All the bands could be fitted by a single Lorentzian peak and showed full width at half max (FWHM) of 60.7, 34.7 and 73.2 cm^{-1} for the D, G, and 2D bands, respectively.[27] The Raman data showed that the quality of the herein produced LIG material had comparable characteristics with those of other LIG materials produced previously by our group and others using polyimide

and other sustainable materials.[35-38] Specifically, the I_D/I_G ratio of 0.6 indicates formation of structures with significant degree of crystallinity within a disordered graphitic carbon network, whereas the I_{2D}/I_G ratio of 0.84, alongside a sharp 2D peak, highlights the formation of a graphene-like multilayer structure characterized by abundant defects and edges.[37] Figure 4.3b shows the XRD pattern of LIG, featuring a sharp major peak at $2\theta = 27^{\circ}$, corresponding to the (002) graphitic crystal planes with an interlayer spacing of ~0.34 nm, and a minor peak at $2\theta = 53^{\circ}$, attributed to the (100) graphitic crystal phase. These data are in line with XRD patterns reported for other LIG structures obtained by laser writing of polyimide, paper, and biopolymers.[38] The thermal stabilization effect of BA in the CS-LIGN formulation was assessed using thermogravimetric analysis (TGA). Figure 4.3c shows the thermal stability of CS-LIGN-BA compared to CS-LIGN substrates. For both materials the TGA curves revealed distinct weight-loss stages, highlighting the thermal stability differences between CS-LIGN and CS-LIGN-BA substrates. These stages were better visualized in the corresponding peaks of the DTA curves, shown as inset in figure 4.3c. For both materials, weight loss occurred in three stages: the first stage (Td_1), up to 100 °C corresponds to the desorption of physiosorbed water; the second stage (Td_2), extending to ca. 200 °C, was attributed to the loss of chemisorbed water; the third stage (Td_3) below 400 °C, represents the thermal decomposition of CS and LIGN. The TGA profile for CS-LIGN showed a moisture weight loss of 25% at 63 °C and 67% at 161 °C, followed by a 68% weight loss at 268 °C due to CS decomposition through pyrolysis of the polysaccharide moiety, starting from a random split of the glycosidic bonds, followed by a further decomposition forming predominantly carboxylic acids.[39] In contrast, CS-LIGN-BA substrates displayed water loss of 63% at 53 °C and 81% at 187 °C, with a subsequent 9% loss at 359 °C. These results suggest that BA introduced a distinct mechanism for water loss in CS-LIGN-BA, attributed to its increased water content, arising from the neutralization reaction between boric acid and chitosan.[34] This could be responsible for the higher water loss observed

in CS-LIGN-BA compared to CS-LIG and the higher temperature at which decomposition occurred (Td_3 of 359 °C for CS-LIGN-BA, 91 °C higher than the Td_3 of CS-LIGN). This observation aligns with earlier findings on LIG formation in CS-BA films, where the presence of BA, due to its radiation shielding capability, was found effective in enhancing the thermal stability of CS, supporting its efficient graphitization.[34] The obtained LIG structure was characterized by XPS to further evaluate the effect of BA in the graphitization process. Figure 4.3d and 4.3e show the deconvoluted C1s XPS peaks for pristine CS-LIGN-BA and LIG, respectively. The peaks were analysed into four components, the main C=C sp^2 and C-C sp^3 carbon bonds, C-O(H) epoxides, hydroxides and C=O carbonyl groups. Peak assignments and percentage of each component concentrations are shown in Table 4.1. XPS data indicated an increase in sp^2 carbon concentration from 13.24% in pristine CS-LIGN-BA to 17.0% in LIG, alongside a decrease in sp^3 carbon from 18.96% to 14.47%, confirming the occurrence of graphitization.

Table 4.1 High resolution XPS fit results for CS-LIGN-BA and LIG

Element(s)	Peak assignment	CS-LIGN-BA			LIG		
		Position	%	FWHM	Position	%	FWHM
Carbon 1s	C=C	284.60	13.24	0.75	284.69	17.00	0.59
	C-C	284.96	18.96	1.00	285.31	14.47	0.89
	C-O	286.32	32.55	1.18	286.67	35.48	1.74
	C=O	288.08	4.88	1.03	288.49	3.23	2.55
Boron 1s	B-N/B-O	191.83	1.27	1.02	193.17	2.97	2.61
Oxygen 1s	O-C	533.17	26.25	1.81	532.76	23.76	2.85
Nitrogen 1s	N-C	399.8	2.03	1.60	401.6	3.01	2.82
	N-O	401.9	0.75	1.70			

Figure 4.3f shows the XPS boron peak for both CS-LIGN-BA and LIG-CS-LIGN-BA films. In the CS-LIGN-BA film, the boron peak appeared at 191.8 eV, corresponding to an atomic percentage of 1.27% and associated with the presence of B-O bonds. After laser irradiation, the boron peak shifted to a higher binding energy of 193.2 eV, indicative of B-O bond formation, and its atomic percentage increased to 2.97%, indicating the incorporation of BA into the LIG structure. The XPS spectrum of O1s species (figure 4.3g) showed a decrease in the overall oxygen content in LIG compared to the pristine CS-LIGN-BA substrate, in line with results obtained for other LIG structures.

4.4.4 Electrochemical characterisation

Direct laser scribing was performed to produce LIG square patterns on CS-LIGN-BA films deposited on PET substrates. A sandwiched SC was fabricated placing PVA/H^+ gel electrolyte (~80 µL) with a polypropylene separator (100 µm) between two LIG square electrodes. Then the assembled SCs were connected to a potentiostat for electrochemical characterization. First, the electrochemical performances of SC devices assembled with LIG electrodes fabricated from CS-LIGN-BA substrates with different BA contents (3–9 wt.%) were investigated. Figure 4.4a shows the CV curves of obtained SCs, measured at 100mV/s scan rate. For all BA percentages almost rectangular CV curves were obtained, indicating good electrochemical double layer properties of the SCs and an increase in capacitive area as the percentage of BA increased. This trend was also evident from the almost triangularly shaped GCD curves recorded at a current rate of 0.2 mA/cm^2 (figure 4.4b), showing larger discharge times for higher BA percentages. Accordingly, higher specific areal capacitances and longer discharge times were measured for SC devices with higher BA percentages (figure 4.4c). EIS was performed to check the resistive nature of assembled SCs made using LIG electrodes obtained from CS-LIGN-BA substrates (figure 4.4d). The low frequency region of the Nyquist plot of the fitted EIS data showed a decrease in both internal and external resistances resulting from

electrode-electrolyte interface as the BA content increased, whereas the high frequency region showed an increase in semicircle with increase in BA content up-to a certain level after which the super-capacitive performance was not significantly influenced (see inset of figure 4.4d).

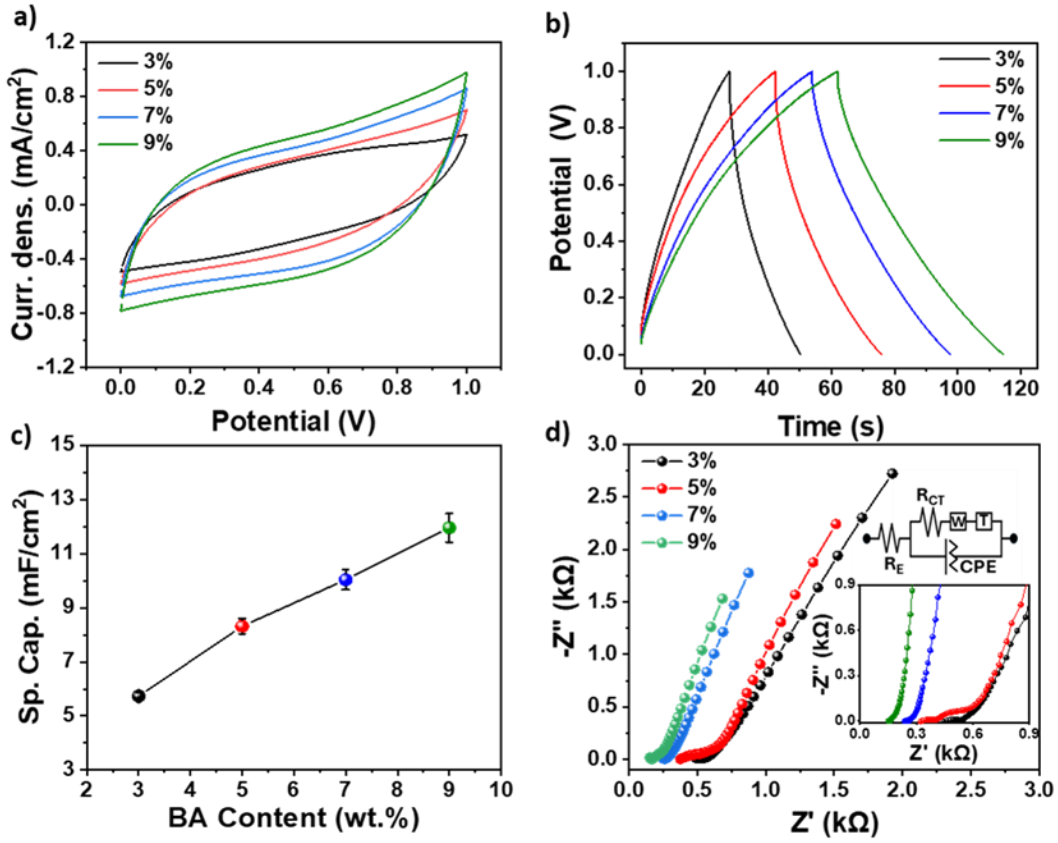

Figure 4.4 Electrochemical performance of LIG supercapacitors fabricated using CS-LIGN-BA substrates with varying BA content (wt.%). a) CV at a scan rate of 100 mV/s; b) galvanostatic charge-discharge (GCD) curves; c) specific areal capacitances for different BA contents at a current density of 0.2 mA/cm²; d) EIS Nyquist fitting plot of SC devices (inset: equivalent EIS circuit and high-frequency region of EIS).

The plot showed a gradual reduction in equivalent series resistance (R_e) as the BA content (wt.%) increased. During discharge processes the initial IR drop values decreased from 55 to 26 mV with the increase of BA percentage from 3 to 9%, indicating a decreased internal resistance of the SC devices.

Further electrochemical characterization of SCs fabricated with LIG from CS-LIGN-BA (9%) was conducted to evaluate their capacitive behaviour. The selection of boric acid (BA)

concentrations (9%) in the CS-LIGN-BA composite film was based on both structural integrity and electrical performance upon laser conversion. Initial tests covered a broader range (1–11 wt%), but lower and higher concentrations were excluded from the final device fabrication for specific reasons. Films with less than 3% BA failed to produce LIG, even at the lowest power and dwell time settings, making device fabrication impossible. Conversely, increasing BA content led to lower sheet resistance after laser treatment, thereby enhancing capacitance. However, to maintain material sustainability and avoid excessive BA content, devices with more than 10% BA were arbitrarily excluded. The final selection of 9% BA thus balanced convertibility, electrical performance, and sustainability in LIG based devices. CV curves recorded at different scan rates (20–100 mV/s) for SC devices with LIG-CS-LIGN-BA (9%) exhibited pseudo-rectangular shapes (figure 4.5a), indicating good electric double-layer capacitive (EDLC) properties. GCD measurements at different charge-discharge rates from 0.1 to 1.0 mA/cm^2, showed pseudo-triangular shapes, also indicating good capacitive properties (figure 4.5b). Specific areal capacitances for the SCs, calculated across various charge-discharge rates, showed a reduction in capacitance values with increasing current density (figure 4.5c). The SCs demonstrated impressive performance, retaining a capacitance of approximately 6.7 mF/cm^2 even when the discharge rate was increased 20-fold, from 0.05 to 1.0 mA/cm^2. A representative SC was cycled for 10,000 cycles through continuous charge-discharge cycling to assess the long-term stability and performance. CV curves at a scan rate of 50 mV/s were recorded every 500 cycles (figure 4.5d) and GCD curves were obtained at a charge discharge rate of 1.0 mA/cm^2 (figure 4.5e). SCs showed nearly stable capacitance retention, maintaining over 68% of their initial capacitance after 10,000 cycles. Close observation revealed that during the initial GCD cycling, the specific areal capacitance slightly increased before reaching stability, followed by a gradual decrease with further cycling. The initial increase in capacitance could be due to better penetration of PVA/H^+ electrolyte into the

porous LIG electrodes, resulting in higher ion transport and electrical double layer formation between anodic and cathodic surfaces.

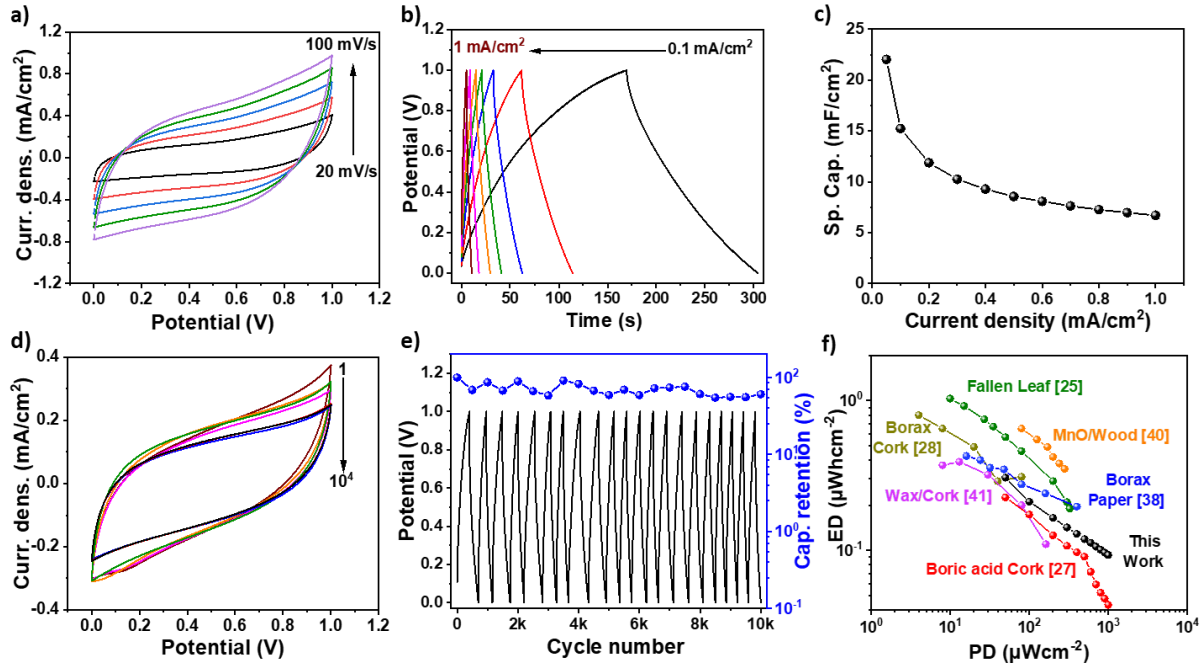

Figure 4.5 a) CVs of LIG supercapacitors fabricated using CS-LIGN-BA substrates with 9 wt.% BA content at different scan rates; b) GCD curves; c) Specific areal capacitances at different current densities; d) selected CVs recorded during long-term cycling; e) capacity retention recorded at regular intervals of 500 cycles up to 10,000 cycles; f) Ragone plot comparing the supercapacitive performance with recently reported sustainable materials.

To quantify the supercapacitive performance of the SCs, specific areal energy densities (ED) were calculated at various power densities (PD) based on total geometric area of anode and cathode surfaces and displayed in a Ragone plot (figure 4.5f) along with recent reported results obtained from LIG graphene based on sustainable sources. The impressive performance and long-cycle stability of these LIG- bio-polymer film-based SCs highlight the potential of chitosan as a viable energy storage material for sustainable electronics.

Cyclic voltammetry analysis provided key insights into the charge storage mechanisms, allowing differentiation between diffusion-controlled pseudocapacitive (PC) and capacitive EDLC contributions. Figure 4.6a shows the contribution of diffusion-controlled pseudocapacitive (PC) contribution and the capacitive electric double-layer capacitance

(EDLC) calculated from CV curves recorded at different scan rates for SC device fabricated with LIG from CS-LIGN-BA (9%). Data showed that at low scan rates (10–30 mV/s) pseudocapacitive processes dominated, yielding specific capacitance of 7.79 mF/cm² at 10 mV/s, significantly surpassing the EDLC contribution (1.82 mF/cm²), resulting in a PC**:**EDLC ratio of 4**:**1. This suggests that at slower scan rates, redox reactions were fully accessible, maximizing PC storage. In contrast, EDLC remained relatively stable, as double-layer formation was nearly instantaneous compared to diffusion-controlled PC storage. As the scan rate increased the PC contribution decreased, due to ion diffusion limitations, whereas the EDLC contribution increased. At 50 mV/s, the PC contribution dropped to ~3.55 mF/cm², while the EDLC increased to ~2.61 mF/cm², shifting the PC:EDLC ratio to 1.4**:**1. At high scan rates (>70 mV/s), EDLC became dominant, as redox reactions become diffusion-limited, restricting PC storage to surface-active sites. The gradual transition from a PC-dominant to an EDLC-dominant mechanism highlighted the dependence of charge storage on scan rate.

The CV curve at a low scan rate of 10 mV/s and GCD curves at a low current density of 0.05 mA/cm² presented in figure 4.6b and 4.6c, demonstrating the capability of supercapacitive performance at low scan rate and low current density. Specific gravimetric capacitances at different current rates showing capacitance up to 1.84 F/g were obtained at 20 mA/g current rate based on the total mass loading (21.36 mg/cm^2) of dry CS-LIGN-BA film on the PET substrate (figure 4.6d). To evaluate their practical applicability, two SCs were connected in series and analyzed. This configuration was tested through cyclic voltammetry (CV) measurements at a scan rate of 100 mV/s (figure 4.6e) and galvanostatic charge-discharge (GCD) curves at current densities of 0.2 mA/cm² (figure 4.6f).

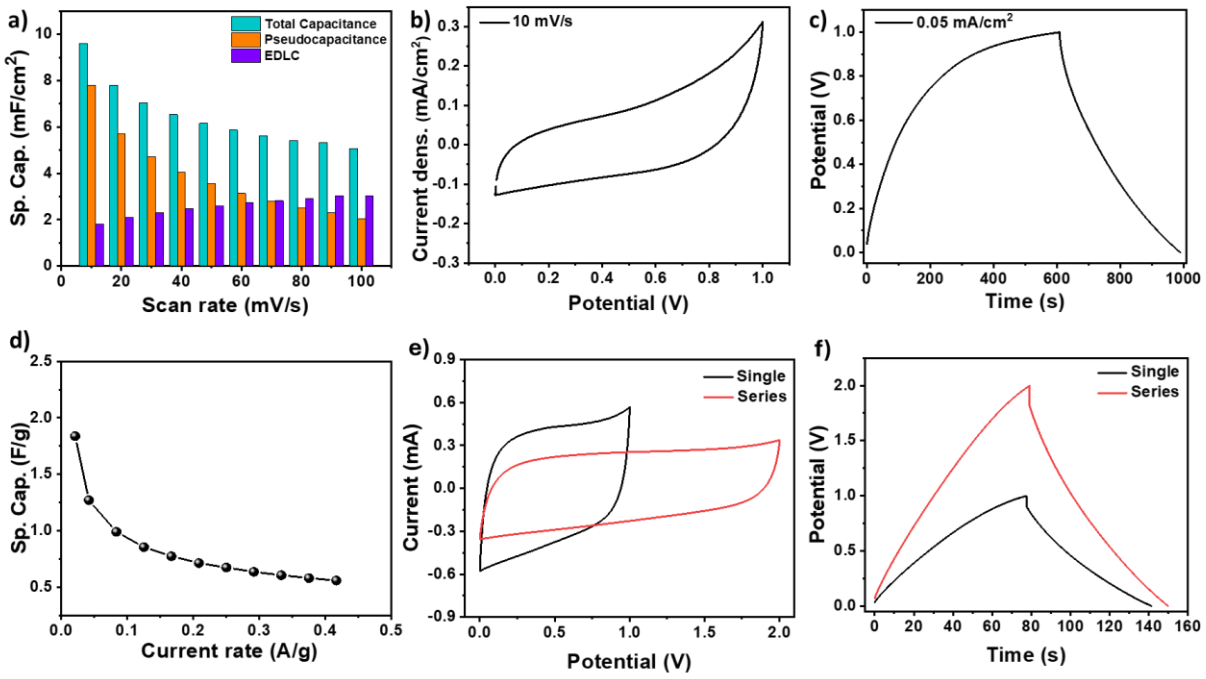

Figure 4.6 (a) Pseudocapacitive (PC) and EDLC contributions to capacitance calculated from CV at varying scan rates; (b) CV curves at 10 mV/s for SCs with LIG-CS-LIGN-BA (9%); (c) GCD profile at 0.05 mA/cm² for SCs with LIG-CS-LIGN-BA (9%); (d) Specific gravimetric capacitances at different charge-discharge current rates; (e) CVs at a scan rate of 100 mV/s; (f) GCD curves at 0.2 mA/cm² for two LIG SCs connected in series.

The results confirmed the feasibility of achieving higher voltage output by connecting the supercapacitors in the series. Furthermore, to assess the capabilities for practical applications, SCs were charged with a commercial solar cell and used to power different devices, as shown in figure 4.7. It was observed that SCs were instantly fully charged by the solar cell, and once disconnected from the charging source, they were able to power a digital temperature-humidity meter, an electronic stopwatch and a calculator.

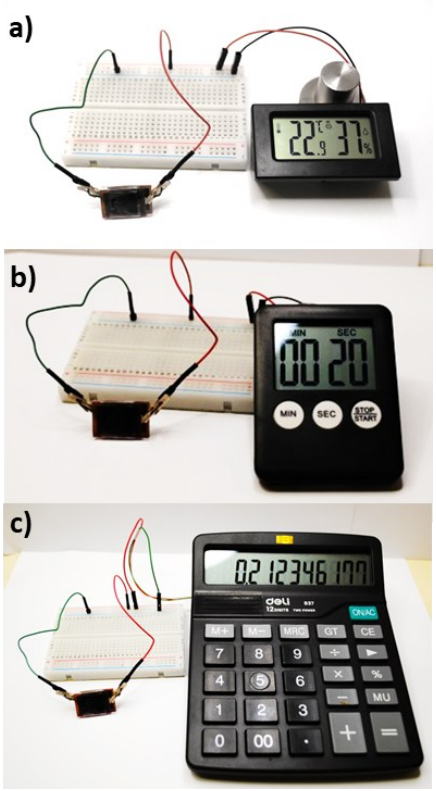

Figure 4.7 Photographs of a single LIG SC powering **a)** a digital temperature-humidity meter; **b)** an electronic stopwatch; **c)** a calculator

Table 4.2 reports a comparison of performance between the SC presented in this work with other "green" SCs fabricated by laser writing technologies. The LIG SCs were characterized by high specific capacitance and areal power density. The reported 68% capacity retention after 10,000 cycles was lower than other reported stability values. Our CV analysis indicated that charge storage occurred through a combination of EDLC and PC processes. The faradaic reactions associated with PC contributions may contribute to gradual electrode degradation, resulting in performance fading over prolonged cycling. Potential degradation mechanisms include electrolyte decomposition or drying over extended charge-discharge cycles, as well as structural instability of the bio-based electrode material due to swelling, dissolution, or mechanical stress.[43-45]

Table 4.2 Comparison of sustainable material based LIGs for supercapacitor devices reported in recent literature.

Substrate materials	**Laser type/ wavelength**	**Specific capacitance @ current density**	**Areal power density**	**Areal energy density**	**Cyclic stability with capacity retention (%)**	**Ref.**
Nageia fleuryi leaf	Femtosecond laser	34.68 mF/ cm^2 @ 5 mV/s	10 $\mu W/cm^2$	1.03 $\mu Wh/cm^2$	50 000 (99%) @ 100 mV/s	[25]
Boric acid treated Cork	450 nm	3.77-11.24 mF/cm^2 @ 0.1 mA/cm^2	55.7 $\mu W/cm^2$	1.7 $\mu Wh/cm^2$	>10 000 (86%) @ 1 mA/cm^2	[27]
Borax treated Cork	CO_2 laser	7–10 mF/ cm^2 @ 0.01 mA/cm^2	4 $\mu W/cm^2$	≈0.77 $\mu Wh/cm^2$	5000 (80–85%) @ 0.08 mA/cm^2	[28]
Borax treated paper	CO_2 laser	4.6 mF/ cm^2 @ 0.015 mA/cm^2	0.3 $\mu W/cm^2$	4.5 $\mu Wh/cm^2$	10 000 (85%) @ 0.5 mA/cm^2	[38]
MnO embedded wood	Femtosecond laser	35.54 mF/ cm^2 @10 mV/s	0.67 $\mu W/cm^2$	80 $\mu Wh/cm^2$	10,000 (82.31%) @100 mV/s	[40]
Wax treated Agglomerated Cork	Nd:YAG fiber laser	1.43 mF/ cm^2 @0.1 mA/cm^2	8 $\mu W/cm^2$	0.37 $\mu Wh/cm^2$	>10 000 (106%) @ 0.05 mA/cm^2	[41]
Cotton cloth/MnO_2	Nd:YAG laser	54.97 mF/ cm^2 @ 0.05 mA/cm^2	7.63 $\mu W/cm^2$	78.93 $\mu Wh/cm^2$	10,000 (80.6%) @ 500 mV/s	[42]
CS-LIGN-BA	450 nm	21.4 mF/ cm^2 @ 0.05 mA/cm^2	50 $\mu W/cm^2$	0.30 $\mu Wh/cm^2$	>10000 (68%) @ 1.0 mA/cm^2	This work

4.4.5 SE-TENG characterization

Prior to undertaking experimental work, a COMSOL Multiphysics simulation was performed to evaluate the suitability of PDMS as a triboelectric active layer. This included numerical calculations to demonstrate the higher surface electric potential of PDMS-SE-TENG compared to bare LIG-SE-TENG devices (figure 4.8), due to the inhibition of surface charge accumulation induced by the bare conductive LIG network. After confirming the suitability of PDMS as a dielectric layer material, the energy harvesting capability and functional stability of the assembled SE-TENG device were evaluated.

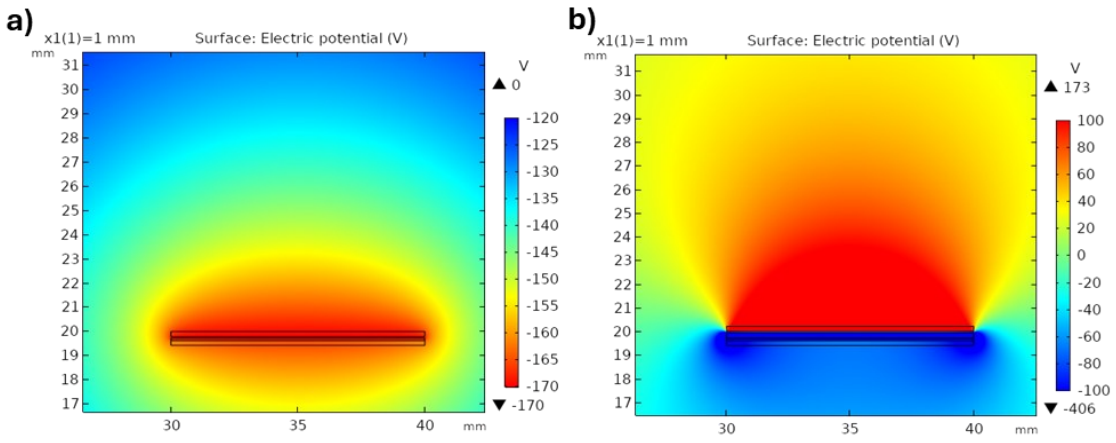

Figure 4.8 Triboelectric surface potential distribution assessed via COMSOL in a) bare LIG- and b) PDMS/LIG configurations.

Figure 4.9a shows the schematic design of the SE-TENG device, comprising a LIG electrode obtained from direct laser writing of CS-LIGN-BA (9%) films on PET, a PDMS dielectric active layer, and PET as the counterpart material. Figure 4.9b illustrates the working principle of the single-electrode triboelectric nanogenerator (SE-TENG) operating in the vertical contact-separation mode. In its initial state **(i)**, the device exhibits no charge transfer or potential difference between its triboelectric layers. However, upon contact with the active surface of the SE-TENG, the counter material (PET) induces charge separation, due to differences in triboelectric affinities. Specifically, PDMS, which has a stronger tendency to attract electrons, gains a negative charge, while PET becomes positively charged, forming an oppositely charged

interface. As the separation process begin **(ii)**, the distance between the triboelectric layers increases, leading to an electrostatic potential difference. This potential imbalance drives electrons through the external circuit, generating a transient current flow until an equilibrium state is established **(iii)**. Upon re-contact **(iv)**, mechanical force reduces the gap between the layers, leading to electron backflow in the opposite direction to restore charge equilibrium. This periodic contact and separation cycle results in a continuous alternating current (AC) output. The electrical output performance of the device was first measured in terms of open-circuit potential (V_{OC}) over extended operating cycles at a frequency of 2 Hz, under varying drive forces of 30, 40, 50, and 60 N. To derive reliable conclusions about the performance of these devices, it is crucial to evaluate the V_{OC} behavior under different mechanical forces. In our study, the applied force during the activation of the nanogenerators exhibited an excellent linear positive correlation, with V_{OC} increasing proportionally to the applied mechanical tension. Figure 4.9c shows the peak-to-peak V_{OC} outputs generated from the contact-separation processes for a SE-TENG device under forces between 30 and 60 N, showing the highest V_{OC} output of 25.8 V/cm². The data show a progressive increase of V_{OC}, associated with the increase of charge transfer produced by the greater interfacial contact area generated by the material's plastic deformation under higher applied forces. In comparison, SE-TENG devices fabricated with no PDMS layer (using air as dielectric) showed much lower performance, with V_{OC} outputs of 11.2 V/cm² (figure 4.10a,b). Figure 4.9d shows a significant increase in V_{OC} with increasing frequency, reaching a plateau at approximately 8 Hz. Beyond this point, V_{OC} remained practically unchanged. This behaviour is associated to the decrease of charge generation rate with the increase of trigger frequency.

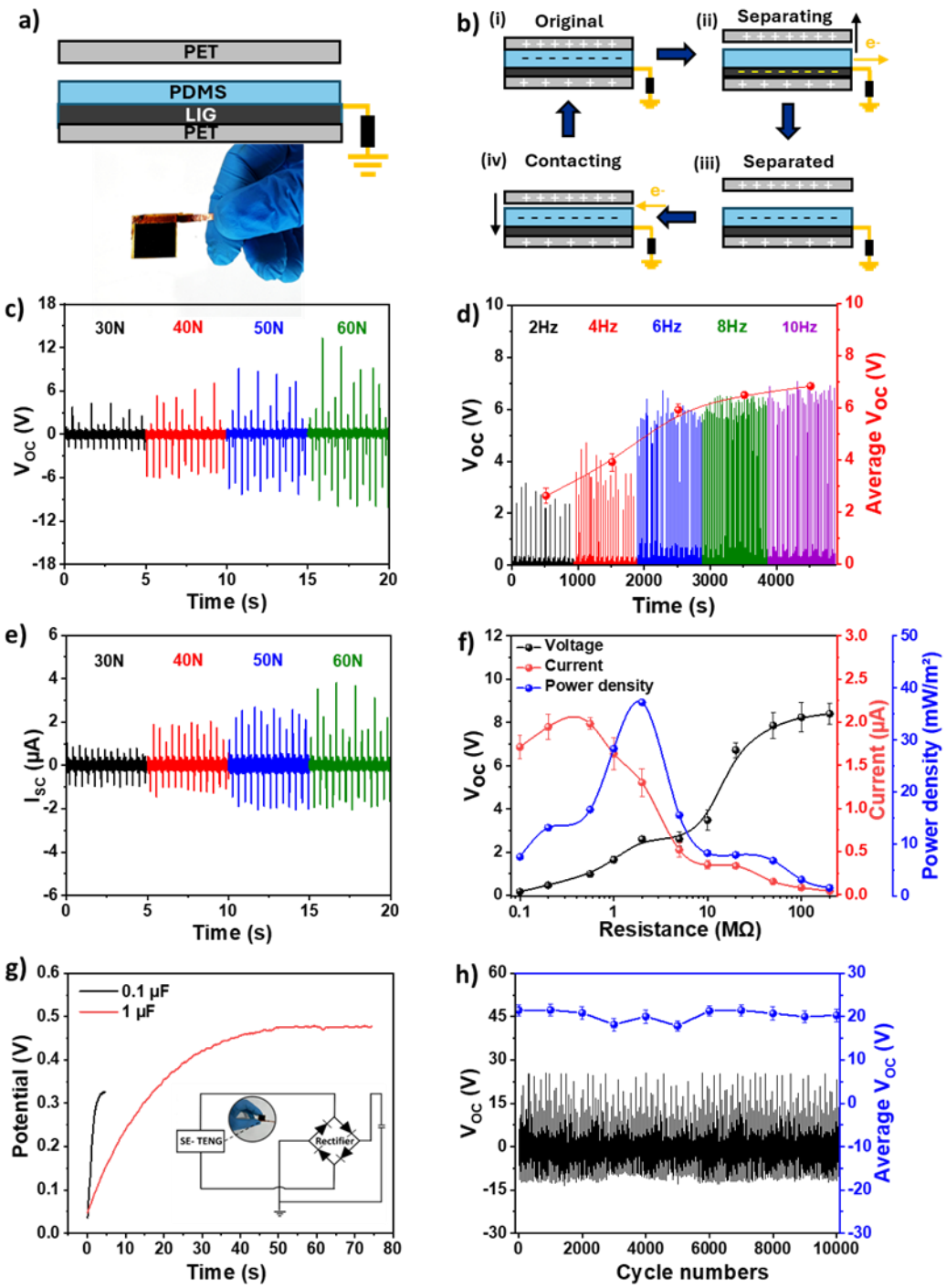

Figure 4.9 a) Schematic of the SE-TENG device, composed of PDMS/LIG, and **b)** an illustration of its working principle in the single-electrode vertical contact-separation mode at various stages; **c)** Open-circuit voltage (V_{OC}) peaks under different contact-separation forces (30, 40, 50, and 60 N); **d)** Open-circuit voltage (V_{OC}) peaks under different frequencies (2, 4, 6, 8, and 10 Hz); **e)** Short-circuit current (I_{SC}) peaks under different contact-separation forces at 2 Hz; **f)** Average V_{OC} and I_{SC} output values and peak power density (PD) across different external resistances; **g)** Charging curves for 0.1 μF and 1 μF commercial capacitors (inset: operational circuit diagram); **h)** Long-term stability of V_{OC} output.

In systems with capacitive effects, lower frequencies allow sufficient time for charge accumulation, enabling the capacitor (or an equivalent charge storage mechanism) to fully charge during each cycle. However, once the frequency exceeds a certain threshold, the system reaches a saturation limit, where charge collection and transfer become inefficient, due to material and circuit constraints. At high frequencies, the recombination rate of charge carriers may begin to match the generation rate, thereby limiting any further increase in V_{OC}. Furthermore, capacitive effects contribute to the saturation behaviour, as the voltage across a capacitor requires time to build up and discharge. Additionally, at elevated frequencies, impedance variations within the circuit may further restrict the system's ability to sustain higher V_{OC} values. Once the system reaches its maximum charge transfer efficiency, further increases in frequency do not contribute to a higher V_{OC}, ultimately resulting in a steady-state response. Figure 4.9e shows the short-circuit current (I_{SC}), measured at 2 Hz, generated during contact-separating cycling process and measured simultaneously with V_{OC} measurements. The I_{SC} values displayed an increase from 1.88 to 5.36 μA with an increase of contact-separation forces from 30 to 60 N. For I_{SC}, the TENG device exhibited performance with a trend like the V_{OC} trend, providing overall stable current outputs over the range of applied contact forces. The average I_{SC} values were measured as 0.24 ± 0.09 μA at a load resistance of 100 kΩ (figure 4.10e), increasing significantly to 5.57 ± 2.27 μA at 200 kΩ (figure 4.10f). The internal resistance and maximum peak power density of the TENG were measured by incorporating a series of variable load resistors into the external circuit. Figure 4.9f illustrates the TENG's power density behaviour across the same range of load resistances. As the external load resistance varied from 0.1 to 200 MΩ the V_{OC} increased from 0.17 V to 8.4 V, while the peak current decreased from 1.7 to 0.042 μA. Furthermore, the I_{SC} exhibited a decline at higher external resistances, whereas the voltage across the load followed an inverse trend, increasing with resistance. Consequently, the power density generated by the TENG initially increased in

the low-resistance region, reaching a maximum peak power of 8.9 mW/m² at a load resistance of 2.0 MΩ. This peak power corresponds to the resonant point where the external resistance aligns with the internal resistance of the TENG system, while beyond this point, the power density decreases in the high-resistance domain. To assess the TENG's energy storage capabilities, the TENG's alternating current (AC) output was converted into direct current (DC) utilizing a bridge rectifier consisting of four Schottky diodes for charging 0.1 and 1 μF commercial ceramic capacitors (figure 4.9g with the circuit diagram depicted in inset). The load curves exhibited a swift rise in output voltage, leading to the saturation of the capacitor. Notably, 0.1 μF capacitors demonstrated rapid charging, while the 1 μF capacitor required approximately 60 s to reach full charge. Finally, the output stability was assessed by measuring the V_{OC} activated at 50 N, which showed minimal fluctuation in the average V_{OC} value and no decrease over 10,000 cycles (figure 4.9h).

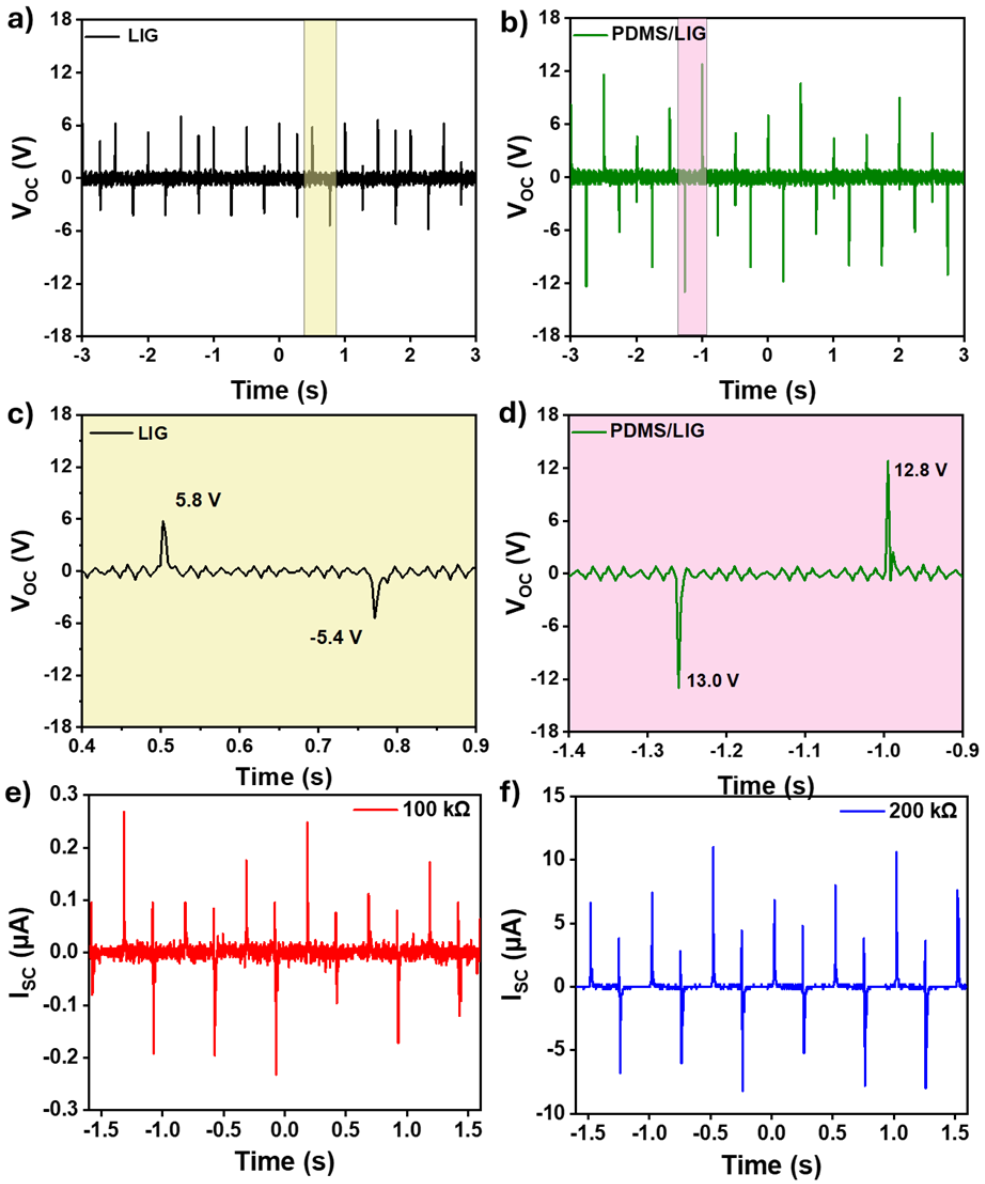

Figure 4.10 V_{OC} peaks of the active friction layer against the counterpart (PET) for SE-TENG with a) bare LIG; and b) PDMS/LIG at applied force of 60 N; (c, d) Expanded view of a) and b) I_{SC} values measured at a load resistance of a) 100 kΩ and b) 200 kΩ.

Finally, a comparative literature analysis with other SE-TENGs employing LIG as an electrode is presented in Table 4.3. The observed peak power density surpassed many of the values reported by several recent publications, as summarized in the figure of merits. Interestingly, when evaluating TENGs with similar characteristics, such as those using LIG fabricated from CS and employing PDMS as active layer, our device notably outperformed its counterparts by up to 335%. This significant result, coupled with the sustained stability demonstrated by the

LIG produced device, emphasizes the critical role of electrode optimization in achieving TENG's enhanced performance.

Table 4.3 Comparison of power density of LIG-based SE-TENG for energy harvesting reported in recent literature.

Active layer/ Counter part	**Electrodes**	**Peak power density (mW/m^2)**	**References**
PI/Al	PI-LIG	2.4	[17]
LF-LIG/PMMA	PI-LIG	512	[46]
SF-LIG/PMMA	PI-LIG	98	[46]
LIG/PMMA	PI-LIG	3.9	[46]
PDMS/Leaf	PI-LIG	80.8	[47]
PDMS/Au-LIG	PI-LIG/Au	11.1	[48]
CMCS/Acrylic	CS-LIG	2.48	[36]
CMCS/PI	CS-LIG	1.44	[36]
PDMS/LIG	CS-LIGN-BA-LIG	8.9	This work

PMMA: polymethyl methacrylate. SF-LIG: Short carbon fiber combined LIG. LF-LIG: Long carbon fiber dominant LIG. CMCS: Carboxymethyl chitosan. PI: polyimide.

4.5 Conclusions

In this work, we have successfully explored the application of chitosan-based green, sustainable, and biodegradable materials as feedstock materials for the direct laser writing fabrication of LIG electrodes and their application in energy storage and harvesting devices. A simple one-step laser writing fabrication was enabled by the addition of BA to the initial feedstock formulation, which enhanced the heat resistance, thus preventing ablation and promoting graphitization. The fabricated SCs could successfully power LEDs and small electronic devices such as a chronometer and an electronic calculator. The capacitive properties of the obtained LIG SC device showed improved performance with the increase of the BA content in the polymer matrix, leading to a final capacitance of 21.4 mF/cm^2 at a current rate of 0.1 mA/cm^2. A SE-TENG device was also fabricated, using PDMS as a dielectric layer. The device showed a max V_{OC} of 13.3V at 60 N and 2 Hz. Ther V_{OC} was also higher compared to other devices fabricated using LIG and PDMS. Considering the eco-friendly chemical composition of the feedstock material, and the ease of LIG fabrication and the performance of fabricated devices, direct laser writing of CS-LIGN-BA films is an attractive tool for the sustainable fabrication of future integrated energy storage /harvesting devices.

4.6 References

[1] J. Kim, A. S. Campbell, B. E. F. de Ávila, and J. Wang, "Wearable biosensors for healthcare monitoring," *Nature Biotechnology*, vol. 37, no. 4. pp. 389–406, 2019. doi: 10.1038/s41587-019-0045-y.

[2] A. A. Smith, R. Li, and Z. T. H. Tse, "Reshaping healthcare with wearable biosensors," *Sci. Rep.*, vol. 13, no. 1, p. 4998, Mar. 2023, doi: 10.1038/s41598-022-26951-z.

[3] D. R. Seshadri *et al.*, "Wearable sensors for monitoring the internal and external workload of the athlete," *npj Digit. Med.*, vol. 2, no. 1, p. 71, Jul. 2019, doi: 10.1038/s41746-019-0149-2.

[4] M. Kang and K. Chai, "Wearable Sensing Systems for Monitoring Mental Health," *Sensors*, vol. 22, no. 3, p. 994, Jan. 2022, doi: 10.3390/s22030994.

[5] F. Khoshmanesh, P. Thurgood, E. Pirogova, S. Nahavandi, and S. Baratchi, "Wearable sensors: At the frontier of personalised health monitoring, smart prosthetics and assistive technologies," *Biosens. Bioelectron.*, vol. 176, p. 112946, Mar. 2021, doi: 10.1016/j.bios.2020.112946.

[6] Z. Yan, S. Luo, Q. Li, Z. Wu, and S. (Frank) Liu, "Recent Advances in Flexible Wearable Supercapacitors: Properties, Fabrication, and Applications," *Adv. Sci.*, vol. 11, no. 8, Feb. 2024, doi: 10.1002/advs.202302172.

[7] G. Pacchioni, "Sustainable flexible supercapacitors," *Nat. Rev. Mater.*, vol. 7, no. 11, p. 844, 2022, doi: 10.1038/s41578-022-00508-y.

[8] A. M. Bayoumy *et al.*, "Microdrop InkJet printed supercapacitors of graphene/graphene oxide ink for flexible electronics," *J. Power Sources*, vol. 617, no. December 2023, 2024, doi: 10.1016/j.jpowsour.2024.235145.

[9] M. M. Momeni, A. S. Renani, and B. K. Lee, "Light-chargeable two-electrode photo-supercapacitors based on MnS nanoflowers deposited on V2O5-BiVO4 photoelectrodes," *J. Alloys Compd.*, vol. 962, no. March, 2023, doi: 10.1016/j.jallcom.2023.171204.

[10] C. Xu, Y. Song, M. Han, and H. Zhang, "Portable and wearable self-powered systems based on emerging energy harvesting technology," *Microsystems Nanoeng.*, vol. 7, no. 1, p. 25, Mar. 2021, doi: 10.1038/s41378-021-00248-z.

[11] R. Liu, Z. L. Wang, K. Fukuda, and T. Someya, "Flexible self-charging power sources," Nat. Rev. Mater., vol. 7, no. 11, pp. 870–886, 2022, doi: 10.1038/s41578-022-00441-0.

[12] K. R. Kaja et al., "Exploring liquid-solid interface based triboelectrification, structures, and applications," Nano Energy, vol. 131, no. September, 2024, doi: 10.1016/j.nanoen.2024.110319.

[13] M. Sahu, S. Hajra, S. Jadhav, B. K. Panigrahi, D. Dubal, and H. J. Kim, "Bio-waste composites for cost-effective self-powered breathing patterns monitoring: An insight into energy harvesting and storage properties," Sustain. Mater. Technol., vol. 32, no. October 2021, 2022, doi: 10.1016/j.susmat.2022.e00396.

[14] S. Panda et al., "Sustainable Solutions for Oral Health Monitoring: Biowaste-Derived Triboelectric Nnanogenerator," Sustain., vol. 11, no. 1, pp. 1–14, 2019.

[15] Y. Wang et al., "TENG-based self-powered device- the heart of life," Nano Energy, vol. 119, p. 109080, Jan. 2024, doi: 10.1016/j.nanoen.2023.109080.

[16] A. Babu, I. Aazem, R. Walden, S. Bairagi, D. M. Mulvihill, and S. C. Pillai, "Electrospun nanofiber based TENGs for wearable electronics and self-powered sensing" Chem. Eng. J., vol. 452, p. 139060, Jan. 2023, doi: 10.1016/j.cej.2022.139060.

[17] W. Ma, J. Zhu, Z. Wang, W. Song, and G. Cao, "Recent advances in preparation and application of laser-induced graphene in energy storage devices," Mater. Today Energy, vol. 18, p. 100569, Dec. 2020, doi: 10.1016/j.mtener.2020.100569.

[18] S. Bai et al., "Laser-induced graphene: Carbon precursors, fabrication mechanisms, material characteristics, and applications in energy storage," Chem. Eng. J., vol. 493, p. 152805, Aug. 2024, doi: 10.1016/j.cej.2024.152805.

[19] S. G. Jo, R. Ramkumar, and J. W. Lee, "Recent Advances in Laser-Induced Graphene-Based Materials for Energy Storage and Conversion," ChemSusChem, vol. 17, no. 5, Mar. 2024, doi: 10.1002/cssc.202301146.

[20] M. G. Stanford, J. T. Li, Y. Chyan, Z. Wang, W. Wang, and J. M. Tour, "Laser-Induced Graphene Triboelectric Nanogenerators" ACS Nano, vol. 13, no. 6, pp. 7166–7174, 2019, [Online]. Available: https://pubs.acs.org/doi/10.1021/acsnano.9b02596

[21] J. Yan, H. Wang, X. Wang, and G. Yang, "High-performance triboelectric nanogenerators with laser-induced graphene pattern for efficient charge transfer," Appl. Surf. Sci., vol. 661, p. 160034, Jul. 2024, doi: 10.1016/j.apsusc.2024.160034.

[22] W. Yang *et al.*, "Structure-Foldable and Performance-Tailorable PI Paper-Based Triboelectric Nanogenerators Processed and Controlled by Laser-Induced Graphene," *Adv. Sci.*, vol. 11, no. 28, Jul. 2024, doi: 10.1002/advs.202310017.

[23] K. Shrestha *et al.*, "A triboelectric driven rectification free self-charging supercapacitor for smart IoT applications," *Nano Energy*, vol. 102, p. 107713, Nov. 2022, doi: 10.1016/j.nanoen.2022.107713.

[24] P. I. C. Claro *et al.*, "Sustainable carbon sources for green laser-induced graphene: A perspective on fundamental principles, applications, and challenges," *Appl. Phys. Rev.*, vol. 9, no. 4, Dec. 2022, doi: 10.1063/5.0100785.

[25] T. D. Le *et al.*, "Green Flexible Graphene–Inorganic-Hybrid Micro-Supercapacitors Made of Fallen Leaves Enabled by Ultrafast Laser Pulses," *Adv. Funct. Mater.*, vol. 32, no. 20, May 2022, doi: 10.1002/adfm.202107768.

[26] C. Larrigy *et al.*, "Porous 3D Graphene from Sustainable Materials: Laser Graphitization of Chitosan," *Adv. Mater. Technol.*, vol. 8, no. 4, 2023, doi: 10.1002/admt.202201228.

[27] A. Imbrogno *et al.*, "Laser-Induced Graphene Supercapacitors by Direct Laser Writing of Cork Natural Substrates," *ACS Appl. Electron. Mater.*, vol. 4, no. 4, pp. 1541–1551, Apr. 2022, doi: 10.1021/acsaelm.1c01202.

[28] S. L. Silvestre *et al.*, "Green Fabrication of Stackable Laser-Induced Graphene Micro-Supercapacitors under Ambient Conditions: Toward the Design of Truly Sustainable Technological Platforms," *Adv. Mater. Technol.*, vol. 9, no. 16, pp. 1–12, 2024, doi: 10.1002/admt.202400261.

[29] Y. Chi *et al.*, "Rice paper-based biodegradable triboelectric nanogenerator," *Microelectron. Eng.*, vol. 216, p. 111059, Aug. 2019, doi: 10.1016/j.mee.2019.111059.

[30] Q. M. Saqib, R. A. Shaukat, M. U. Khan, M. Chougale, and J. Bae, "Biowaste Peanut Shell Powder-Based Triboelectric Nanogenerator for Biomechanical Energy Scavenging and Sustainably Powering Electronic Supplies," *ACS Appl. Electron. Mater.*, vol. 2, no. 12, pp. 3953–3963, Dec. 2020, doi: 10.1021/acsaelm.0c00791.

[31] H. Singh, A. Sheetal, J. Kaur, M. Singh, and M. Sharma, "Generation of Electrical Energy Using Fish Market Waste Fish Fin from Mechanical Motion for Battery-Less Self—Powered Wearable Sensors and IoT Devices," *Electron. Mater. Lett.*, vol. 19, no. 5, pp. 483–494, Sep. 2023, doi: 10.1007/s13391-023-00420-9.

[32] L. Ģērmane, L. Lapčinskis, M. Iesalnieks, and A. Šutka, "Surface engineering of PDMS for improved triboelectrification," *Mater. Adv.*, vol. 4, no. 3, pp. 875–880, 2023, doi: 10.1039/D2MA01015A.

[33] Z. Peng *et al.*, "Flexible Boron-Doped Laser-Induced Graphene Microsupercapacitors," *ACS Nano*, vol. 9, no. 6, pp. 5868–5875, Jun. 2015, doi: 10.1021/acsnano.5b00436.

[34] E. Vaughan *et al.*, "Direct Laser Writing of Chitosan–Borax Composites: Toward Sustainable Electrochemical Sensors," *ACS Sustain. Chem. Eng.*, vol. 11, no. 37, pp. 13574–13583, 2023, doi: 10.1021/acssuschemeng.3c02708.

[35] D. Iacopino *et al.*, "Visible laser scribing fabrication of porous graphitic carbon electrodes: Morphologies, electrochemical properties, and applications as disposable sensor platforms," *ACS Appl. Electron. Mater.*, vol. 2, no. 10, pp. 3279–3288, 2020, doi: 10.1021/acsaelm.0c00612.

[36] Q. M. Huang *et al.*, "Laser-Induced Graphene Formation on Chitosan Derivatives toward Ecofriendly Electronics," *ACS Appl. Nano Mater.*, vol. 6, no. 12, pp. 10453–10465, 2023, doi: 10.1021/acsanm.3c01408.

[37] E. Vaughan *et al.*, "Sustainable Laser-Induced Graphene Electrochemical Sensors from Natural Cork for Sensitive Tyrosine Detection," *Adv. Sens. Res.*, vol. 2, no. 12, Dec. 2023, doi: 10.1002/adsr.202300026.

[38] J. Coelho *et al.*, "Paper-based laser-induced graphene for sustainable and flexible microsupercapacitor applications," *Microchim. Acta*, vol. 190, no. 1, p. 40, Jan. 2023, doi: 10.1007/s00604-022-05610-0.

[39] C. G. T. Neto, J. A. Giacometti, A. E. Job, F. C. Ferreira, J. L. C. Fonseca, and M. R. Pereira, "Thermal analysis of chitosan based networks," *Carbohydrate Polymers*, vol. 62, no. 2. pp. 97–103, 2005. doi: 10.1016/j.carbpol.2005.02.022.

[40] Y. R. Kim *et al.*, "Green supercapacitor patterned by synthesizing MnO/laser-induced-graphene hetero-nanostructures on wood via femtosecond laser pulses," *Biochar*, vol. 6, no. 1, 2024, doi: 10.1007/s42773-024-00320-7.

[41] S. L. Silvestre *et al.*, “Cork derived laser-induced graphene for sustainable green electronics,” *Flex. Print. Electron.*, vol. 7, no. 3, 2022, doi: 10.1088/2058-8585/ac8e7b

[42] L. Lu, D. Zhang, Y. Xie, and W. Wang, “A stretchable, high-voltage and biobased microsupercapacitor using laser induced graphene/MnOx electrodes on cotton cloth,” *J. Energy Storage*, vol. 51, no. January, 2022, doi: 10.1016/j.est.2022.104458.

[43] Z. Khan, P. Singh, S. A. Ansari, S. R. Manippady, A. Jaiswal, and M. Saxena, “VO2 Nanostructures for Batteries and Supercapacitors: A Review,” *Small*, vol. 17, no. 4, pp. 1–33, 2021, doi: 10.1002/smll.202006651.

[44] G. A. M. Ali *et al.*, “Superior supercapacitance behavior of oxygen self-doped carbon nanospheres: a conversion of Allium cepa peel to energy storage system,” *Biomass Convers. Biorefinery*, vol. 11, no. 4, pp. 1311–1323, 2021, doi: 10.1007/s13399-019-00520-3.

[45] S. Yamada, “A Transient Supercapacitor with a Water-Dissolvable Ionic Gel for Sustainable Electronics,” *ACS Appl. Mater. Interfaces*, vol. 14, no. 23, pp. 26595–26603, 2022, doi: 10.1021/acsami.2c00915.

[46] K.-H. Choi *et al.*, “Triboelectric effect of surface morphology controlled laser induced graphene,” *J. Mater. Chem. A*, vol. 8, no. 38, pp. 19822–19832, 2020, doi: 10.1039/D0TA05806H

[47] X. Li, C. Jiang, F. Zhao, Y. Shao, Y. Ying, and J. Ping, “A self-charging device with bionic self-cleaning interface for energy harvesting,” *Nano Energy*, vol. 73, p. 104738, Jul. 2020, doi: 10.1016/j.nanoen.2020.104738

[48] H. Chen *et al.*, “A multiple laser-induced hybrid electrode for flexible triboelectric nanogenerators,” *Sustainable Energy and Fuels*, vol. 5, no. 14. pp. 3737–3743, 2021. doi: 10.1039/d1se00819f.

Chapter 5: Summary and Future Work

5.1 Summary of Thesis

This thesis focuses on the advancement of low-cost, sustainable electrochemical sensors, energy storage and harvesting devices. The research follows a systematic approach beginning with the use of a low-power laser system to fabricate Laser-Induced Graphene (LIG) from both synthetic and natural carbon-rich substrates, including polyimide, cork, and chitosan. These materials were extensively characterized and evaluated for their electrochemical performance, aiming to assess their viability for practical sensing and energy applications.

Chapter 2 introduces a cost-effective method to fabricate Ag nanoparticles–LIG hybrid electrodes using direct laser writing on polyimide tapes, followed by functionalization with silver nanoparticles. These electrodes demonstrated sensitive detection capabilities for analytes such as 4-aminobenzenethiol (4-ABT), melamine in milk, and difloxacin hydrochloride in river water through Electrochemical-Surface Enhanced Raman Spectroscopy (EC-SERS). The method enables rapid, high-sensitivity analysis without the need for pre-treatment, supporting applications in food safety and environmental monitoring. This technique underscores the simplicity and sustainability of the sensing platform.

In Chapter 3, the potential of cork as a renewable carbon precursor for LIG-based supercapacitors is explored. The cork-derived LIG exhibited high surface area, excellent electrical conductivity, and strong electrochemical performance, positioning it as an eco-friendly option for energy storage devices. The fabricated supercapacitors showed high areal capacitance, robust stability over charge/discharge cycles, and mechanical flexibility, making them well-suited for wearable electronics and sustainable energy systems.

Chapter 4 presents a green and efficient approach to develop supercapacitors and triboelectric nanogenerators (TENGs) using LIG derived from chitosan-lignin-boric acid films. Fabricated via a one-step laser-writing process, these LIG materials exhibited interconnected porous

networks, high surface area, and low sheet resistance. The resulting supercapacitors achieved an areal capacitance of 21.4 mF/cm² and retained 68% capacity after 10,000 cycles. Meanwhile, the TENGs produced a maximum open-circuit voltage of 13.3V, sufficient to power small electronics. This approach aligns with the growing demand for biodegradable, cost-effective energy harvesting systems.

A comparative overview is provided in the table 6.1 for the LIG materials used throughout the thesis. Cork-derived LIG reported the best performance in terms of Raman $I_{D/G}$ ratio, sp^2 carbon content, and sheet resistance. Notably, the cork-LIG forms deep conductive layers (~500 μm), which enhance its overall conductivity.

From a fabrication perspective, cork electrodes offer the advantage of being self-supporting. In contrast, polyimide and chitosan-lignin-boric acid-based LIG require external support from rigid substrates like glass slides or PET sheet. However, cork's natural variability due to its biological origin may lead to inconsistent LIG quality. Polyimide, being synthetic, offers better surface reproducibility. One limitation observed in the chitosan-lignin-boric acid composite is its mechanical instability in humid conditions, which can result in surface swelling and cracking.

Table 6.1 Comparison of material characteristics of LIG derived from polyimide, cork and the chitosan-lignin-boric acid substrates. $I_{D/G}$ and $I_{2D/G}$ refer to intensity ratios derived from Raman results; C sp^2 data, XPS, and TLM.

Material	**Laser wavelength (Power-Depth)**	**$I_{D/G}$**	**$I_{2D/G}$**	**C sp^2 (%)**	**R_{SH} (Ω/sq)**
Polyimide	450 nm (30-40)	~0.9	~0.8	71.1 [1]	96 ± 4 [1]
Boric acid-Cork	450 nm (30-40)	~1	~0.37	24.7	38 ± 2
CHI-LIG-BA	450 nm (30-40)	~0.6	~0.84	17.0	35 ± 2

In terms of applications, polyimide-based LIG electrodes have shown excellent sensing capabilities, particularly for detecting difloxacin hydrochloride (Chapter 2). Cork- and chitosan-lignin-boric acid-derived LIGs have proven effective for energy storage (Chapter 3 and 4) and energy harvesting (Chapter 4). Furthermore, in collaboration with external partners, polyimide-LIG was successfully functionalised for biosensing of Interleukin-6, yielding promising results. While chitosan-lignin-boric acid (CS-LIGN-BA) derived LIG currently demonstrates material performance comparable to existing alternatives, it remains in the early stages of development. Nevertheless, it holds significant promise as a next-generation material for sustainable electrochemical energy devices, including supercapacitors and triboelectric nanogenerators (TENGs).

5.2 Future Work

The findings presented in Chapters 2, 3, and 4 clearly establish that Laser-Induced Graphene (LIG), fabricated using a low-carbon footprint 450 nm laser system, is an excellent material for electrochemical sensing, energy storage and harvesting applications. Based on these results, several promising avenues for future research are identified. We plan to develop and demonstrate a label-free LIG electrodes on polyimide substrates for the detection of antibiotics, particularly tetracycline, in aqueous media. This aligns with the growing need for real-time, cost-effective, and eco-friendly monitoring of water quality.

For supercapacitor (SC) applications, future work will focus on integrating biodegradable electrolytes and eco-friendly separators to enhance the environmental sustainability of these devices. This will also involve fine-tuning the electrochemical characteristics to meet the performance needs of flexible and wearable electronics.

In the area of triboelectric nanogenerators (TENGs), we intend to further optimize device performance by exploring new geometrical configurations and incorporating green dielectric materials. This research direction is inspired by the encouraging energy harvesting data

presented in Chapter 4 and aims to improve output efficiency and durability while adhering to sustainability goals.

An essential part of our future strategy involves addressing the limitations of the current subtractive DLW process. Specifically, we will explore methods to enable the transfer of LIG onto various substrates, which will allow for more flexible device integration and compatibility with a wider range of biopolymeric feedstocks. Overcoming this constraint is vital for broadening the applicability of LIG in green electronics, particularly where natural materials may not be directly graphitizable. The potential of Direct Laser Writing (DLW) and green Laser-Induced Graphene (gLIG) as enablers for sustainable electronics is substantial, particularly in light of the global challenges associated with traditional electronics manufacturing, which often relies on conventional materials, energy-intensive semiconductor fabrication, and complex integration processes. Current industrial practices typically follow a linear economic model of "take, make, dispose," wherein single-use designs and low recyclability are tolerated to achieve commercial efficiency. Most electronic products are mass-produced without consideration for carbon footprint associated to manufacturing or end-of-life reuse and recyclability. With the growing global demand for electronics—evidenced by the consumer electronics market being valued at US$ 3,296.66 million in 2023 and projected to reach US$ 5,820.65 million by 2033- necessitates a shift towards circular electronics ensuring this growth is sustainable. Such a shift is critical to address the depletion of natural resources and to mitigate greenhouse gas emissions linked to e-waste generation. [2-3]

In this context, DLW and gLIG present a unique opportunity to advance circular electronics. However, several critical challenges must be overcome to enable their widespread, real-world implementation. Laser processing parameters must be carefully optimized to produce gLIG with consistent surface morphology, high surface area, excellent electrical conductivity, and reliable electrochemical performance. Furthermore, the mechanical strength, chemical

resistance, and stretchability of both the precursor materials and the resulting gLIG must be tailored to meet the demands of specific applications—areas that remain largely underexplored. The variety of biopolymers suitable for gLIG synthesis is still limited. For example, pure chitosan requires a three-step laser graphitization process, which is impractical for scale-up. Although the incorporation of lignin and boric acid has enabled single-step graphitization, the use of boric acid raises environmental concerns, as it is classified as a critical material. To align with the goals of green electronics, such additives should ideally be replaced with more sustainable alternatives.

Moreover, many natural feedstocks lack the mechanical and thermal stability required for efficient DLW processing, underscoring the need for the development of reinforcement strategies and improved biopolymer formulations. To facilitate the transition from laboratory-scale research to industrial deployment, future work should focus on establishing reproducible DLW protocols, engineering green-compatible substrates, and developing scalable, eco-friendly fabrication methods. With sustained innovation, LIG-based technologies hold great promise for enabling the next generation of low-footprint, biodegradable, and sustainable electronic devices.

5.3 References

[1] D. Iacopino *et al.*, "Visible laser scribing fabrication of porous graphitic carbon electrodes: Morphologies, electrochemical properties, and applications as disposable sensor platforms," *ACS Appl. Electron. Mater.*, vol. 2, no. 10, pp. 3279–3288, 2020, doi: 10.1021/acsaelm.0c00612.

[2] Draghi, M. (2024) The future of European competitiveness. Part A: A competitiveness strategy for Europe, available at https://commission.europa.eu/document/download/97e481fd-2dc3-412d-be4cf152a8232961_en

[3] Narendra Singh, Oladele A. Ogunseitan, "Disentangling the worldwide web of e-waste and climate change co-benefits," *Circular Economy,* vol. 1, no. 2. pp. 2773-1677, 2022. doi.org/10.1016/j.cec.2022.100011.

5.4 Publications

1. Alessandra Imbrogno, **Jahidul Islam,** Chiara Santillo, Rachele Castaldo, Labrini Sygellou, Cathal Larrigy, Richard Murray, Eoghan Vaughan, Md. Khairul Hoque, Aidan J. Quinn, and Daniela Iacopino; *Laser-Induced Graphene Supercapacitors by Direct Laser Writing of Cork Natural Substrates.* ACS Applied Electronic Materials 2022, 4 (4), 1541-1551 https://doi.org/10.1021/acsaelm.1c01202
2. Yunyun Mu, **Jahidul Islam,** Richard Murray, Cathal Larrigy, Alida Russo, Xinping Zhang, Aidan J. Quinna and Daniela Iacopino. *Silver nanoparticles – laser induced graphene (Ag NPs – LIG) hybrid electrodes for sensitive electrochemical-surface enhanced Raman spectroscopy (EC-SERS) detection* Analyst, 2023, 148, 3087 https://doi.org/10.1039/D3AN00731F
3. **Jahidul Islam** et al., "Eco-Friendly Energy Storage and Energy Harvesting Devices Fabricated by Direct Laser Writing of Chitosan-Lignin-Boric Acid Substrates," ACS Appl. Electron. Mater., vol. 7, no. 11, pp. 4801–4813, 2025, doi: 10.1021/acsaelm.5c00234.

5.5 Conferences

- Development of a LIG based-electrochemical sensor and a SERS-LFIA for sensitive detection of residual antibiotics in milk" *Jahidul Islam, Alida Russo and Daniela Iacopino, Nano-innovation conference and exhibition 2021, Rome, Italy, 21-24th September, 2021*
- Green Electrodes for Super Capacitors Fabricated by One-step Visible Direct Laser Writing of Cork Natural Substrates *Alessandra Imbrogno, Jahidul Islam_and Daniela Iacopino Nano-innovation conference and exhibition 2021, Rome, Italy, 21-24th September, 2021*
- Development of a Laser Scribed Graphene based Electrochemical Sensor for the detection of Tetracycline Hydrochloride, *Jahidul Islam_and Daniela Iacopino* Vistamilk Industry Day, Portlaoise, Ireland, 9th November, 2021

- Determination of Antibiotic Residues in Milk" *Jahidul Islam_and Daniela Iacopino,* Vistamilk Internal conference 2022, Cork, Ireland, 9-10th May, 2022
- "Green Supercapacitors Based on Electrodes Fabricated by Single-step Visible Direct Laser Writing of Chitosan film", Spring Meeting (2023), EMRS, Strausburg, France.

5.6 Completed Modules

- **SE6014** Semiconductor Growth and Fabrication Technology (2020-2021)
- **IS6306** Technology Business Planning (2020-2021)
- **PG6001** STEPs Scientific Training for Enhanced Postgraduate Studies (2020-2021)
- **PG6015** An Introduction to Research Integrity, Ethics and Open Science (2021-2022)
- **ST6013** Statistics and Data Analysis for Postgraduate Research students (2021-2022)
- **LW6104** Principles of Intellectual Property Law (2021-2022)
- **MG6705** Marketing for Technology Entrepreneurs (2021-2022)
- **IS6307** Creativity and Opportunity Recognition (2023-2024)
- **IS5004** IT Solution Selling and Digital Business (2023-2024)
- **BU6011** Innovation Finance (2023-2024)

5.7 Education and Public Engagement (EPE)

1. VistaMilk International Workshop on Spectroscopy and Chemo-metrics – 28th April 2021
2. The Vidacademy Session 1 and 2 with VistaMilk – 30th April & 7th May 2021
3. "Coding with Cows" Coding Week classroom visit (5th and 6th grade students) – 11th & 16th November 2021, Cork Educate Together National School, Cork
4. Carnival of Science – 11th & 12th June 2022, Fitzgerald Park, Cork
5. Communications Masterclass – "What's the Story?" – 14th June 2022, Devere Hall, UCC
6. Internship Lunchtime Lab Tour – 24th July 2022, Chemistry Lab (A1.1.01)

7. VistaMilk - Ploughing Championships – Ratheniska, Co. Laois 20th to 22nd September 2022
8. Cork Science Festival –13th November 2022 Western Gateway building, UCC
9. EPE Training – 21st November 2022
10. Cork Carnival of Science – 9th June 2023 Fitzgerald Park, Cork
11. Marine Science Event (Marina Market, Cork) – 18th November 2023
12. Research Demonstration for UCC 1st Year Engineering Student Lab Tours – 23rd February 2024